VARIABLE RANGE HOPPING CONDUCTION IN THE EPITAXIAL GRAPHENE BUFFER LAYER ON SIC(0001)

A Thesis
Presented to
The Academic Faculty

by

Jean-Philippe Turmaud

In Partial Fulfillment
of the Requirements for the Degree
Doctor of Philosophy in the
School of Physics

Georgia Institute of Technology
August 2018

VARIABLE RANGE HOPPING CONDUCTION IN THE EPITAXIAL GRAPHENE BUFFER LAYER ON SIC(0001)

Approved by:

Walt A. de Heer, Advisor
School of Physics
Georgia Institute of Technology

Martin Mourigal
School of Physics
Georgia Institute of Technology

Phillip N. First
School of Physics
Georgia Institute of Technology

Paul Douglas Yoder
School of Electrical and Computer Engineering
Georgia Institute of Technology

Zhigang Jiang
School of Physics
Georgia Institute of Technology

Date Approved: June 13, 2018

To Danielle, and to Nugget

ACKNOWLEDGEMENTS

How I came about completing this thesis is a story that involves many characters, and in the space I have here, I will not be able to acknowledge every single one of them. For those I will forget, forgive me. And thank you!

To my advisor, Dr. Walt de Heer, thank you for welcoming me into your research group, for your guidance and for sharing your vision throughout my years in your lab. You have pushed me to think outside the box and I will carry this far beyond this PhD work. To Dr. Claire Berger, thank you for giving me the opportunity to first come as an intern in 2012 and for being always present to coach and support me in the lab.

I am grateful to my thesis committee, Dr. Phillip First, Dr. Zhigang Jiang, Dr. Martin Mourigal, and Dr. Douglas Yoder, for patiently reviewing and evaluating my work.

I am forever indebted to all my colleagues and friends from the epitaxial graphene lab. Thanks to Dr. Dogukan Deniz, Dr. Jamey Gigliotti, Yiran Hu, Yue Hu, Dr. Vladimir Prudkovskiy, Dr. John Hankinson, Dr. Renaud Puybaret, Dr. James Palmer, Dr. Clement Bouvier, Dr. Jan Kunc, Dr. Lei Ma, Dr. Ming Ruan, Dr. Rui Dong and Dr. Zelei Guo, for our endless discussions on graphene and many other life matters. Working with all of you has been a real pleasure, and your help in learning about epitaxial graphene, as well as using, building and maintaining diverse pieces of equipment in the lab has made this work possible.

My time at Georgia Tech has also involved collaborative efforts. I would like to give special thanks to the CASSIOPEE beam line at Synchrotron SOLEIL in France for my two trips there. For the long hours spent doing measurement day and nights, I would like to thank Dr. Maya N. Nair, Dr. Arlensiú Celis, Dr. Antonio Tejeda, Dr. Amina Taleb-Ibrahimi and Dr. Ed Conrad. It was also a pleasure to work for a short time on ultrafast optics at the University of Michigan with Gong Cheng and Dr. Ted Norris.

I would not have been able to do much without the help from the IEN staff with the

cleanroom tools, or without the staff of the School of Physics, always eager to help me with random issues. I would also like to acknowledge the great work of the office of international studies at Georgia Tech coordinating the logistics for international students.

My gratitude goes to my fellow students in the School of Physics, Dr. Matt Conrad, Dr. Stephen Spitz, Benedikt Brandt, Geoff Laughon, John Indergaard, Chris Crowley, Simon Berman and Oliver Pierson, who became friends and allies in the challenges we faced together. There are no words to describe the honor I have had to go through this program alongside you.

To my parents, Jean-Louis and Hélène, and siblings, Céline, Sylvain and Alexandre, thank you for always believing in me and supporting me in my decisions, even when it meant living thousands of miles away. To my friends back home who, despite the distance, keep being a part of my life, thank you. To my "adopting" family and friends here in Atlanta, thank you for welcoming me so warmly and making me feel at home.

Last but not least, a heartfelt thank you to you Danielle, without whom I would certainly not be writing these lines today. Know that your endless support, your patience, your sacrifices, and your simple presence by my side are invaluable.

TABLE OF CONTENTS

DEDICATION . . . . . **iii**

ACKNOWLEDGEMENTS . . . . . **iv**

LIST OF TABLES . . . . . **ix**

LIST OF FIGURES . . . . . **x**

SUMMARY . . . . . **xviii**

I INTRODUCTION **1**

1.1 General introduction to graphene 3

1.2 Production of graphene 6

1.2.1 Mechanical exfoliation of graphite 6

1.2.2 Reduction of graphene oxide 7

1.2.3 Chemical vapor deposition 7

1.3 Epitaxial graphene on silicon carbide 8

1.3.1 Growth 9

1.3.2 Polar faces 10

1.3.3 Sidewall nanoribbons 14

1.4 Motivations to study the electronic transport properties of the buffer layer 15

II EXPERIMENTAL METHODS **17**

2.1 Growth and characterization of epitaxial graphene 17

2.1.1 Confinement control sublimation process 17

2.1.2 Raman spectroscopy 19

2.1.3 Scanning probe microscopy 21

2.1.4 Low energy electron diffraction 26

2.1.5 X-ray photoemission spectroscopy 27

2.2 Micro and nano-fabrication 28

2.2.1 Electron-beam lithography 28

2.2.2 Reactive ion etching 30

2.2.3 Thin film deposition 30

2.2.4 Chemical deposition 31

2.2.5 Physical deposition . . . 32
2.2.6 Lift-off . . . 34
2.2.7 Typical process flow . . . 34
2.3 Transport measurement . . . 34
2.3.1 Four point probe stations . . . 34
2.3.2 Low temperature transport . . . 36
III REVIEW OF THE EPITAXIAL GRAPHENE BUFFER LAYER . . . 38
3.1 Atomic structure . . . 38
3.1.1 LEED pattern and STM measurement . . . 39
3.1.2 Intercalation of the buffer layer . . . 41
3.1.3 XPS analysis . . . 42
3.1.4 Measurement of the buffer layer corrugation . . . 43
3.1.5 Comment on the nature of the interactions . . . 44
3.1.6 Raman spectroscopy . . . 46
3.2 Band structure . . . 47
3.2.1 ARPES measurements and calculations . . . 47
3.2.2 Conduction band . . . 49
IV TRANSPORT MEASUREMENTS ON THE BUFFER LAYER . . . 52
4.1 Device fabrication considerations . . . 53
4.1.1 SiC surface preparation for buffer layer devices . . . 53
4.1.2 Growth parameters . . . 55
4.1.3 Sample packaging and definition of a "clean" device . . . 57
4.2 Contact vs bulk resistance for clean samples . . . 58
4.3 Modulation of the conduction . . . 60
4.3.1 Effect of the environment . . . 60
4.3.2 Gated devices . . . 65
4.4 Magneto-transport . . . 66
4.4.1 Hall measurement . . . 67
4.4.2 Magneto-resistance . . . 68
4.5 Observation of Mott's variable range hopping . . . 68

4.5.1 Data acquisition . . . 69
4.5.2 Temperature dependence at low bias voltage . . . 71
4.5.3 Variable range hopping conduction . . . 72
4.5.4 Electric bias dependence at 4.2 K . . . 76
4.5.5 Effective temperature, localization length, and density of states . . . 79

V DISCUSSION OF THE VARIABLE RANGE HOPPING CONDUCTION IN THE BUFFER LAYER . . . 84

5.1 Electron localization in 2D and quasi 2D systems . . . 84
5.1.1 Variable range hopping in carbon materials . . . 84
5.1.2 Localization in periodic graphene structures . . . 87
5.2 Image charge potential as the origin of localization in the buffer layer . . . 88
5.2.1 Classical calculation of the image potential . . . 88
5.2.2 Quantum effects . . . 91
5.3 Alternative model . . . 92

VI CONCLUSION . . . 95

6.1 Thesis summary . . . 95
6.2 Outlook . . . 96
6.2.1 The buffer layer at high temperature . . . 96
6.2.2 Theoretical work . . . 97

REFERENCES . . . 98

VITA . . . 114

LIST OF TABLES

1 Historical account of the early research on graphene. References and detailed timeline can be found in Ref. [17] 3

LIST OF FIGURES

1.1 Evolution of the number of publications related to graphene per year. 2

1.2 a) Graphene is a honeycomb lattice of carbon atoms (represented by blue and yellow circles in this model) covalently bonded through their sp^2 orbitals. The sub-lattices A and B are highlighted by the two different colors. The unit cell vectors $\mathbf{a_1}$ and $\mathbf{a_2}$ are indicated by the red arrows. b) Reciprocal lattice of graphene with position of Γ, K and M points and reciprocal lattice vector $\mathbf{b_1}$ and $\mathbf{b_2}$ (black arrows). 4

1.3 Nearest neighbor tight-binding calculation of free-standing graphene. The valence and conduction bands touch each other at the K points with a linear Energy-Momentum dispersion around that energy, forming "Dirac cones". . 5

1.4 SiC polytypes 4H, 6H, 3C and their $(11\bar{2}0)$ plane. 9

1.5 a) LEED of C-face epitaxial graphene and b) ARPES giving the measured band structure. 11

1.6 LEED pattern of a buffer layer sample grown by the CCS method. 12

1.7 a) Experimental energy bands along a line through the K point parallel to the Γ-M direction. The dashed lines are an extrapolation of the lower bands (below E_F), which are observed not to pass through the upper bands (above E_F), suggesting the kinked shape of the bands around E_F. The electron density (per cm2) is indicated. b) Band map acquired in an orthogonal direction through the K point, for which one of the bands is suppressed . . . 13

1.8 Cross sectional transmission electron microscopy image of a sidewall nanoribbon. The graphene is seamlessly connected to the buffer layer on the top terrace. 15

2.1 Confinement control sublimation furnace. Top: photograph of the furnace at 1400°C. Bottom: furnace diagram. Si gas sublimes from the crucible walls and the sample and is confined to the enclosure allowing close to equilibrium graphene growth. 18

2.2 Raman spectra of quasi-free standing monolayer graphene on SiC Si-face. The blue spectrum (on top) is the raw data. The red curve (below) is the spectrum after subtraction of the bare SiC background 21

2.3 Principle of AFM. a) Lennard-Jones potential describing the interactions between the short range forces of the surface and an AFM tip. C-AFM operates close to the surface while NC-AFM operates further away from it. b) Basic elements of an AFM. A 4-segment photodiode measures the changing reflection of a laser on the back of the cantilever, flexing due to the height variation on the sample. 23

2.4 Illustration of LFM signal. The surface structure contains topography features and is composed of 3 different materials (labelled 1, 2 and 3) with different frictional coefficient μ such that $\mu_1 > \mu_2 > \mu_3$. Topography features are independent of scan directions in LFM signal because it laterally bends the tip in the same direction while the frictional forces signal changes sign between left and right scan. 24

2.5 Principle of e-beam evaporation. A beam of electron is focused on the metal source to melt it locally. The metal vapor travels to the sample through the high vacuum chamber and the deposition is monitored by the crystal monitor. 33

2.6 Typical process flow for epitaxial graphene device fabrication. If sidewall nanoribbons are part of the device design, a lithography and RIE steps are added before the growth of graphene. Top gated devices requires to add multiple lithography and deposition steps at the end. 35

2.7 The Hall effect for negative charge carrier (electrons) and positive ones (holes). The sign of the Hall voltage depends the sign of the charges. 37

3.1 A model of a graphene layer (honeycomb lattice) grown on 1x1 Si-terminated β-SiC(111) (dots). A,B,C,D,E and F indicate positions where the C atoms on the top layer coincide exactly with the Si atoms on the second layer. The dotted circle, G, outlines positions where the C atoms and Si atoms nearly coincide. The graphene honeycomb spacing is 2.46 Å and the Si-Si spacing is 3.1 Å. 39

3.2 STS and STM images taken on the buffer layer. 40

3.3 XPS analysis of the buffer layer. 42

3.4 XRR and XSW measurement on the buffer layer. 43

3.5 Top and side views of the buffer layer structure. a) STM image (I = 0.25 nA, V = 1.5 V) of the buffer layer, showing the quasi-6×6$_{SiC}$ periodicity (black diamond). b) Close-up on the image shows the graphene honeycomb structure without hexagonpentagonheptagon defects. c) TEM image of a cut through the buffer layer grapheneSiC interface. The dotted line is a guide to the eye above the buffer layer to show the bonding points of the buffer layer to the substrate. The overall periodicity between bonding points is 1.6 nm, compatible with a 6×6$_{SiC}$ period. (d) Vertical profiles of the interface in c have been obtained by averaging the TEM data over several regions where the buffer is attached to the substrate (contact) and where it is decoupled (bump). The red arrows in panel c indicate where the contact profiles were measured. 44

3.6 Relationship between the σ-σ and σ-π interorbital angles and the hybridization at a carbon atom between the extremes of sp^2 (planar geometry) and sp^3 hybridization (tetrahedral geometry). 45

3.7 Example of a Raman spectrum of a buffer layer sample grown via CCS. . . . 46

3.8 Photoemission intensity map vs binding energy and parallel electron momentum of UHV grown (a) buffer layer and (b) monolayer graphene on top of the buffer layer. 48

3.9 Comparison of ARPES data with DFT calculated band structure. a) DFT bands. Red dashes are corresponding to the DFT bands that found a close match in ARPES data. b) ARPES data with overlaid selected bands from DFT calculation. c) Low energy ARPES data with overlaid bands from DFT calculation. 49

3.10 Comparison of ARPES data before and after Cs depostition. The Dirac point from the small coverage of monolayer graphene is shifted 1 eV down while the top of the buffer layer band is only shifted about 0.3 eV. 50

4.1 SWGNRs and buffer layer seamlessly connected in a top gated device geometry. 53

4.2 NC-AFM topography images of SiC surface after face-to-face annealing for a) 4° off-axis 4H SiC and b) on-axis 4H SiC. 54

4.3 C-AFM topography images of SiC surface after growth of the buffer layer succeeding face-to-face annealing at a) 1550°C (with its corresponding LFM image in b) and c) 1700°C (LFM in d). Dark contrast in LFM corresponds to graphene ribbons. 55

4.4 Examples of nanostructures for graphene contacted buffer layer devices. a) AFM image and b) corresponding LFM of a Hall bar device after graphene growth. c) AFM image and d) corresponding LFM of a series of two-terminal graphene contacted devices. Dark contrast in LFM is low friction graphene ribbons. 56

4.5 NC-AFM topography images Pd/Au contacts directly deposited on the buffer layer. a) In line contacts b) Hall bar geometry. 56

4.6 IV curves of a graphene contacted two-terminal buffer layer device in different conditions. Coating the device with Al_2O_3 (red curve) has a similar effect as measuring the device annealed in a vacuum probe station (blue curve). Data for the contaminated device was multiplied by a factor 10 for visibility (green and brown curves). 58

4.7 Zero bias resistance of a series of Pd/Au contacted clean buffer layer devices plotted versus the length of the devices. 59

4.8 Zero bias resistance of a series of graphene contacted clean buffer layer devices plotted versus the length of the devices. 59

4.9 a) IV curves of graphene contacted devices exposed to air. Each device length is indicated in the legend, showing that the positive voltage part of the curve does not scale with the length of the device. b) IV curves at different temperatures for one of the devices. The structure in the IVs is more pronounced at low temperature. 61

4.10 LFM images showing that the edges of graphene are meandering and therefore quite different from one another. Image b is a zoom in image a. 62

4.11 Effect of oxygen adsorption on a metal contacted buffer layer device. a) Relative change of conductance after introduction of oxygen at time t=0s. b) IV curves of the devices in different conditions. 62

4.12 Effect of ammonia adsorption on a metal contacted buffer layer device. The relative change of conductance is measured over time. The higher conductance state is observed when the chamber is filled with 10 mbar of NH_3 while the lower conductance is when the chamber is evacuated. 65

4.13 Log plot of the current versus gate voltage for $V_{bias} = 1$ V, measured at various temperatures. 66

4.14 Hall voltage measurement at 420 K of a graphene contacted Hall bar measured as a function of an applied perpendicular magnetic field. 67

4.15 Magnetoresistance measurement at 420 K of a graphene contacted two-terminal device measured as a function of an applied perpendicular magnetic field. . . 68

4.16 IV curves for a) device A and b) device B. As device B is measured in vacuum, the lack of exchange gas did not allowed the sample to cool all the way down to 4.5K. 70

4.17 Temperature dependence of the zero bias conductance of device A tested for an Arrhenius behavior. The curve is not a straight line showing the absence or such a behavior. 71

4.18 Resistance curve derivative analysis of the temperature dependence of the low bias voltage of devices A, B, C and D. They all give a value of α around 1/3. 73

4.19 Temperature dependence of the conductance of device A and device B. The minimum temperature of the range of validity is limited by the minimum current of the measurement setup. 74

4.20 Basic illustration of carrier transport in a doped semiconductor. At high temperature (left side), the electrons (blue dots) have enough thermal energy to go into the conduction band while at low temperature (right side), the conduction occurs via hopping from one site to another. 75

4.21 Resistance curve derivative analysis of the voltage dependence of the low bias voltage of devices A, B, C and D. They all give an value of α around 1/3 despite a large dispersion devices B and D. 77

4.22 The band bending in a strong electric field increases the number of states accessible by hopping. 79

4.23 Biased electric field dependence of the conductance of device A and device B at 4.2 K. 80

4.24 E^* plotted versus T^* for different buffer layer devices and samples. The linear fit is calculated for the data in red. Blue crosses are outliers and are not taken into account in the fit. 82

4.25 a) IV curves of device A and their fit according to equation 28 with ξ as a fitting parameter. b) Fitted values of ξ at each temperature. 83

5.1 Temperature dependence of amorphous carbon thin films showing a 2D Mott variable range hopping conduction. 85

5.2 Modelization of the buffer layer topography. 89

5.3 Image charge potential of a point charge in the buffer layer. a) Image potential map of a point charge in the buffer as modeled in Fig. 5.2. b) and c) Slices of V_{image} along the x and y directions. 90

5.4 Realistic image charge in the buffer layer should consider the wave function of the electron rather than a point charge. 91

5.5 Schematic view of electron probability density near metal gate and density of image charge. 92

5.6 (a) A model structure based on modulated SiC layer (Black circles are carbon unbonded to the SiC. Gold circles are carbon bonded to Si in the interface layer below.). Red dashed hexagon marks the boundary of an isolated graphene island. (b) The calculated charge density (arbitrary units) at E=-0.6 eV for the structure in (a). 94

List of symbols and abbreviations

Ω	Ohms
2D	Two-dimensional
aC	Amorphous carbon
AFM	Atomic force microscopy
ALD	Atomic layer deposition
ARPES	Angle resolved photoemission spectroscopy
atm	Atmosphere
C-AFM	Contact mode atomic force microscopy
C-face	Carbon terminated $(000\bar{1})$ face of hexagonal SiC
CCD	Charge-coupled device
CCS	Confinement control sublimation
CNT	Carbon nanotubes
CVD	Chemical vapor deposition
DFT	Density functional theory
EBL	Electron beam lithography
EFM	Electrostatic force microscopy
hBN	Hexagonal boron nitride
IPA	Isopropyl alcohol
IV	Current-voltage

LDOS	Local density of state
LEED	Low energy electron diffraction
LFM	Lateral force microscopy
NC-AFM	Non contact mode atomic force microscopy
NLSE	Nonlinear Schrödinger's equation
PID	Proportional-integral-derivative
PMMA	Poly(methyl methacrylate)
PSI	Pounds per square inch. 1 PSI = 69 mbar
PSPD	Position sensitive photo-detector
QFSG	Quasi free-standing graphene
RCDA	Resistance curve derivative analysis
RIE	Reactive ion etching
SEM	Scanning electron microscope
Si-face	Silicon terminated (0001) face of hexagonal SiC
SiC	Silicon carbide
SPM	Scanning probe microscopy
STM	Scanning tunneling microscopy
STS	Scanning tunneling spectroscopy
SWGNR	Sidewall graphene nanoribbon
T	Temperature
T_{eff}	Effective temperature

TBG	Twisted bilayer graphene
TEM	Transmission electron microscopy
TMA	Trimethylaluminum
UHV	Ultrahigh vacuum
XPS	X-ray photoemission spectroscopy
XRR	X-ray reflectivity

SUMMARY

The properties of epitaxial graphene grown by thermal decomposition of hexagonal silicon carbide (SiC) have been the focus of extensive research for several decades now. In this thesis I am interested in the electronic transport properties of the first graphene layer grown on the (0001) of SiC, referred to as the buffer layer. It has been shown previously that the buffer layer is structurally a continuous graphene layer subject to periodic interactions with the underlying substrate. Electronically, the band structure presents a gap around the Fermi level. While much effort has been devoted to the surface science of the buffer layer, little is known about the actual dynamics of its charge carriers. To shed light on its properties as an electronic material, I performed temperature and bias voltage dependent electronic transport measurements on buffer layer devices. The buffer layer is found to display an insulating behavior with the conductivity following a 2D Mott variable range hopping model between 80K and 420K. At lower temperatures, the hopping can also be activated by a strong bias electric field. An effective temperature can be defined to take into account both temperature and electric field, which gives an estimate for the localization length of electrons in the buffer layer between 1 and 2 nm. A model of localization based on the image potential experienced by charges in the corrugation of the buffer layer is presented to explain the observed transport properties.

CHAPTER I

INTRODUCTION

Marie Skłodowska Curie once said: "I am among those who think that science has great beauty. A scientist in his laboratory is not only a technician: he is also a child placed before natural phenomena which impress him like a fairy tale. "[1] Many would agree that graphene, a single layer of carbon atoms bonded to each other in a honeycomb lattice, fits well into this description. Indeed, it has been the playground of an increasing number of scientists and engineers since its rise to popularity in 2004[2, 3]. A simple look at the number of publications per year related to graphene between 2004 and 2014 (Fig. 1.1) shows to what extent it had been the case[4]. Apart from the fact that graphene displays remarkable mechanical properties[5], most of the excitement towards the first truly two dimensional (2D) material finds its source in its unique properties as an electronic material: electrons behave as massless particles and have low scattering probabilities leading to high carrier mobility[6]. The range of applications that have been dreamed of extends now from transistors[7] to solar cells[8], including chemical sensors[9, 10], spintronic devices[11] and supercapacitors[12], to only cite a few. The unique behavior of the massless Dirac Fermions in graphene has also made it an ideal platform to study novel condensed matter physics experimentally[13].

The realization of the possibility of producing graphene on an insulating substrate[3, 2] comes at a time when silicon is getting close to reach a point of physical limitation. Silicon transistors have been made smaller and smaller over the years, following co-founder of Intel corporation Gordon Moore's prediction of doubling the number of components per integrated circuit every one to two years[14]. This prediction, now referred to as "Moore's law", included the fact that this rate of progress would not be sustainable forever. As of 2018, semiconductor chip manufacturers are mass producing transistors with a channel

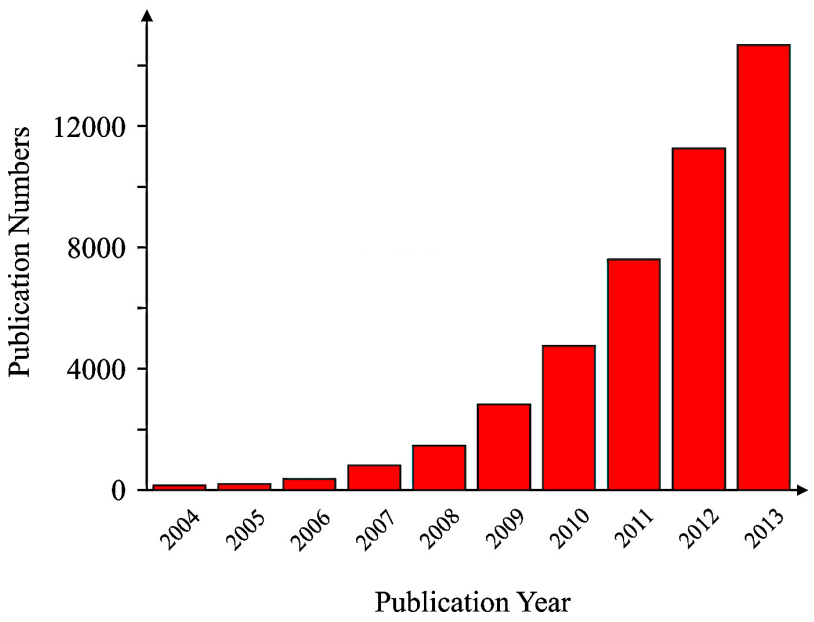

Figure 1.1: Evolution of the number of publications related to graphene per year.

length (the active semiconducting part of the component) around 10 nm[15]. The performance of silicon transistors starts to decline at those length scales and their integration requires more advanced engineering[16]. Alternative materials have been investigated for decades now, and graphene is only one of many. As many challenges have come on the way of making graphene a suitable material for electronic applications, other 2D materials have joined the race towards new relevant technologies.

This is the context in which this thesis is situated. I present here the results and analysis of experimental investigations performed on the buffer layer, a unique form of graphene interacting with its underlying substrate, silicon carbide (SiC). While my interest in studying the buffer layer was triggered by its potential as a semiconductor, perhaps the unforeseen physical phenomenon unveiled in this work may, in the words of Mrs Curie, "impress us like a fairy tale". Before getting there, I will give in this chapter some generalities about graphene, its properties and how it is produced. I will spend a large part of this chapter introducing epitaxial graphene on SiC in more details, as it is the focus of this thesis.

Table 1: Historical account of the early research on graphene. References and detailed timeline can be found in Ref. [17]

1840	Graphite oxide prepared by Schafhaeutl, Brodie, Staudenmaier, Hummers and others
1858	Brodie separated individual layers of graphite oxide in water
1893	Acheson discovered the graphitization of silicon carbide at high temperature
1947	Wallace calculated the band structure of graphene
1962	Boehm and coworkers prepared single layer graphene by reduction of graphite oxide and Badami observed the graphitization of the surface of hexagonal SiC
1968	First LEED pattern of graphene by decomposition of small organic molecules on Pt by Morgan
1970	Segregation of carbon on Ni(100) into monolayer graphite by Blakely and coworkers
1975	Van Bommel observed the formation of monolayer graphite on SiC by thermal decomposition
1997	Graphene name adopted officially by IUPAC
2004	Geim and Novoselov performed magneto-transport in exfoliated ultrathin graphite
2004	Berger and coworkers performed magneto-transport in ultrathin epitaxial graphite on SiC
2005	Geim and Novoselov, and simultaneously Kim, measured electronic transport in exfoliated single layer graphene

1.1 General introduction to graphene

Many of the properties of graphene have been known for a long time, as carbon has been a substance of interest since at least the 19^{th} century. Table 1 summarizes the history related to graphene prior to its rise to fame in the mid-2000. One could have also included carbon nanotubes (CNT) in this table, as their electrical properties strongly mimic those of graphene ribbons. CNT became the focus of intensive research studies in the 1990s due to, for instance, their room temperature ballistic conduction[18]. CNTs are rolled up graphene sheets that can be either metallic or semiconducting. These one-dimensional objects are very attractive for electronic applications but the difficulty resides in aligning them and selecting their electronic nature (metal or semiconductor) during their production. Graphene, on the other hand, possesses the advantage to be a planar material that is compatible with current lithography processes[19].

As mentioned previously, graphene is a single crystal of carbon atoms placed onto a

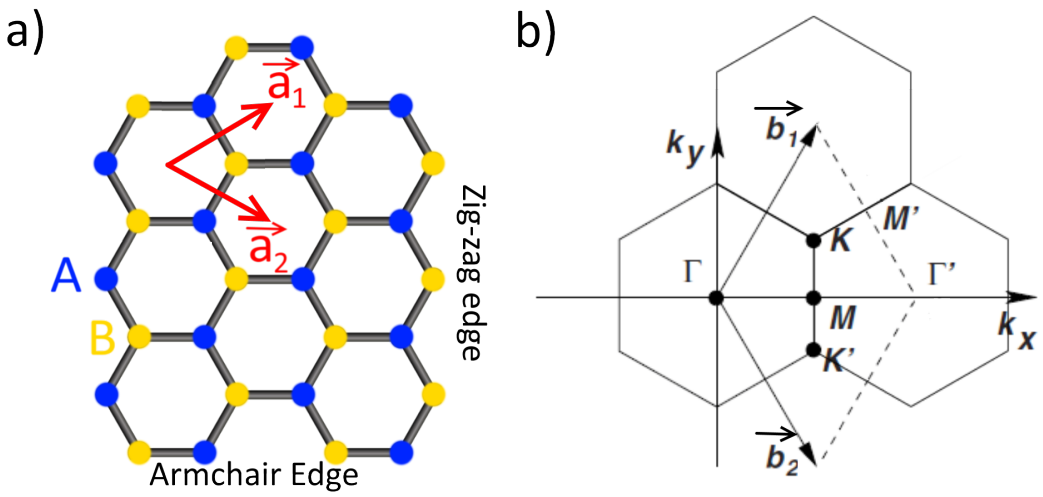

Figure 1.2: a) Graphene is a honeycomb lattice of carbon atoms (represented by blue and yellow circles in this model) covalently bonded through their sp^2 orbitals. The sub-lattices A and B are highlighted by the two different colors. The unit cell vectors $\mathbf{a_1}$ and $\mathbf{a_2}$ are indicated by the red arrows. b) Reciprocal lattice of graphene with position of Γ, K and M points and reciprocal lattice vector $\mathbf{b_1}$ and $\mathbf{b_2}$ (black arrows).

honeycomb lattice, as depicted in Fig. 1.2. The unit cell is composed of two atoms and is defined by the vectors $\mathbf{a_1}$ and $\mathbf{a_2}$. Two triangular sub-lattices can be defined by the two carbon atoms of the unit cell, usually named sub-lattice A and sub-lattice B, which are both Bravais lattices while the honeycomb one is not. This structure has interesting consequences on the electronic structure of graphene as we will discuss shortly. The lattice constant of graphene, defined as the length of the unit vectors, has a theoretical value around 2.456 Å[20]. This value can be slightly modulated in real systems due to the interactions with the surrounding inducing compressive or tensile strain.

Each carbon atom has four valence electrons, in orbitals 2s, $2p_x$, $2p_y$, and $2p_z$. They can hybridize in different way to form bonds with their neighboring atoms depending on the conditions at which the bond is formed. In diamond, they form four equivalent sp^3 hybrized orbitals that form bonds with four neighboring carbon atoms and no electron is available for conduction. This explains the insulating nature of undoped diamond. In graphite, CNTs and graphene, three electrons hybridize into sp^2 orbitals to from three σ-bonds in the plane, while the $2p_z$ electron delocalizes to become a π-electron responsible for conduction. A simple tight-binding model of those *pi*-electrons is able to describe most

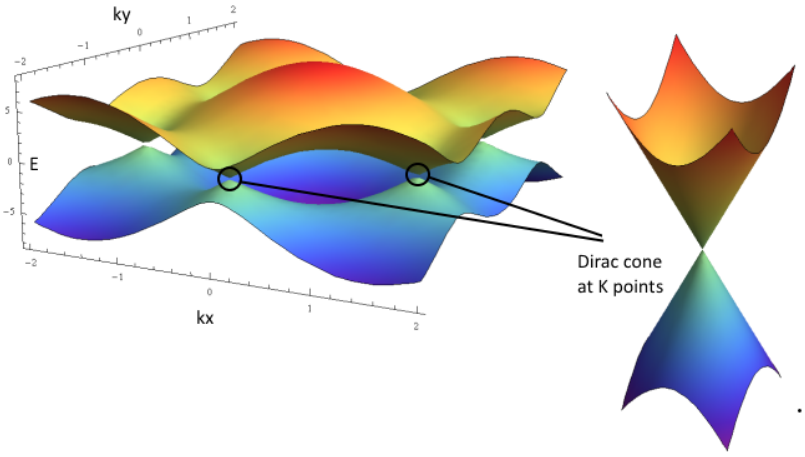

Figure 1.3: Nearest neighbor tight-binding calculation of free-standing graphene. The valence and conduction bands touch each other at the K points with a linear Energy-Momentum dispersion around that energy, forming "Dirac cones".

of the electronic structure of graphene. It was first derived by P. R. Wallace in 1947 as he was investigating the properties of graphite[21]. Taking only the nearest neighbors into account, he obtained:

$$E(\mathbf{k}) = \pm t\sqrt{1 + 4cos^2(\frac{k_y a}{2}) + 4cos(\frac{k_y a}{2})cos(\frac{\sqrt{3}k_x a}{2})} \tag{1}$$

where t=2.7eV is the hopping integral and a is the graphene lattice parameter. As it can be seen in Fig. 1.3, the valence band and the conduction band touch each other at zero energy at specific points called the K points. Around those K points the dispersion relation can be approximated to:

$$E(\mathbf{k}) = \pm\hbar v_F|\mathbf{K} - \mathbf{k}| \tag{2}$$

where $v_F = \frac{\sqrt{3}at}{2\hbar} \approx 10^6$ is the Fermi velocity. This has a conical shape and is therefore often referred to as a Dirac cone. It is interesting to note that the energy is linearly proportional to the momentum, indicating that electrons and holes behave as if they were massless particles, much like photons, with a constant velocity around that energy. One can also note that the density of states vanishes at the K points, giving graphene the status of a semi-metal or zero gap semiconductor, with its dominant charge carriers easily modulated from n-type (electrons) to p-type (holes).

An interesting consequence of this band structure is the existence of pseudospin in

graphene, which originates from the fact that it is composed of the two sub-lattices mentioned previously. The π-orbitals between A and B are orthogonal, which, by analogy with the spin of electron that can be up or down, has been described by a pseudospin, which is a good quantum number. A wave-function that would only reside on sub-lattice A (B) would have a pseudo spin up (down). The pseudospin of electron in graphene is therefore a linear combination of state up and state down, and is parallel to the plane of graphene[22]. In addition, the pseudo spin is aligned with the momentum of the electron, either parallel or antiparallel. As a consequence of the conservation of pseudospin, backscattering, in other words the reversal of the momentum, is prohibited. This feature is unique to Dirac electrons in graphene and is one reason for the high mobility of this material.

1.2 Production of graphene

Discovering new methods to produce graphene has almost became a field of research in itself. Some methods produce high crystalline quality graphene crystal on a wafer scale, while others results in micrometer size flakes, polycrystalline graphene or disordered graphene. The main avenues of production are mechanical exfoliation of graphite[23], chemical reduction of graphene oxide[24], chemical vapor deposition[25], and thermal decomposition of silicon carbide[26, 3].

1.2.1 Mechanical exfoliation of graphite

Mechanical exfoliation is made possible in layered material such as graphite or hexagonal boron nitride (hBN) due to the weak Van der Waals interactions coupling the layers. This method has become very popular as it does not require any advanced and expensive piece of equipment and produces high mobility sample[2, 23]. The most simple most way to cleave graphite consists in using a piece of scotch tape to repetitively peel layers off of it until single layer flakes are obtained. The flakes are then transferred to an insulating substrate such as oxidized silicon or boron nitride for further characterization. Graphene encapsulated by hBN has proven to show superior properties compared to the one deposited on SiO_2[27]. It is also possible to obtain suspended graphene sheet by chemically etching the underlying SiO_2[28]. Many properties of graphene have been unveiled in exfoliated samples

such as the quantum Hall effect[29], the fractional quantum Hall effect, indicative of electron-electron interactions for high quality samples[30], or even unconventional superconductivity in twisted bilayer graphene very recently[31]. Despite the exciting research performed on those samples, this fabrication method is unfortunately not industrially scalable[6].

1.2.2 Reduction of graphene oxide

As reported in table 1, graphene oxide has been produced since around 1840. Nowadays, the reduction of graphene oxide by thermal treatments is a commonly used method to produce graphene in a cheap way[32]. The quality of the thereby produced graphene samples is however much lower than those obtained by other methods, and are therefore systematically referred to as reduced graphene oxide (rGO)[24]. Graphite oxide is initially obtained using some variation of Hummers method, consisting in exposing graphite to a mixture of water free concentrated sulfuric acid, sodium nitrate and potassium permanganate[33]. The layers are successively separated from each other under ultrasonication of the oxide in water. The reduction of graphite oxide is then performed using various methods, such as purely thermal annealing, UV irradiation, chemical reduction, or a combination of several of those[32]. Some additional details on the conduction mechanism in rGO will be discussed in chapter 5. Despite the poor electronic quality of rGO, it remains an actively investigated method to produce industrial scale graphene for many applications.

1.2.3 Chemical vapor deposition

Chemical vapor deposition (CVD) involves the decomposition of hydrocarbon gas precursor on transition metal such as Cu[34], Ni[35], Co[36], Ir[37], Pd[38], Pt[39], or Ru[40]. This process was also shown to work on SiC[41]. The quality of graphene has been shown to be dependent on the quality of the substrate, the size of its grains, the temperature of the substrate during deposition. The concentration of precursor, the growth time and temperature are all parameters determining the number of layers formed during growth. The properties of graphene are also different from substrate to substrate due to the different interactions between the carbon atoms and the underlying substrate. This will be a recurring theme throughout this dissertation as similar effects occurs for graphene on SiC and are

responsible for the formation of the buffer layer.

The main disadvantage of CVD graphene (apart from CVD on SiC) comes from the impossibility to make electronic devices on it as long as it rests on a conductive substrate that would short the current. Transfering the graphene requires to cover the graphene with PMMA and to selectively etch the metal away before put the graphene on an insulating substrate such as SiO_2 and removing the PMMA. Such process tends to bring contamination on graphene leading to reduced mobilities[42].

Much effort is dedicated to improve the aforementioned methods of graphene production. As we are about to see however, epitaxial graphene on SiC is a very promising platform for graphene nanoelectronic as well as a material rich in condensed matter phenomena. It is a simple method to produce high crystalline quality graphene directly on a commercially available substrate.

1.3 Epitaxial graphene on silicon carbide

Silicon carbide is a wide band gap semiconducor material that can be found in many different crystal structures, which are called polytypes. It is actually a synthetic material that initially produced in 1891 by A. G. Acheson who had an interest in its use as a extremely hard material (close to the hardness of diamond). As we will see in this section, the quality and properties of epitaxial graphene grown on SiC depend not only on the polytype but also on which crystallographic face the crystal is terminated. The most commonly used polytypes are 4H and 6H hexagonal SiC (displaying a band gap of 3.3 eV and 3.0 eV respectively) which can be bought in the form of wafers. 3C SiC has a cubic structure and is also the focus of some research studies, although it is not currently produced in the form of wafers but is usually grown on another substrate[43]. The crystal structures of these three polytypes are given in Fig. 1.4. SiC can be made either semi-insulating by pinning the Fermi level in the gap or conductive by specifically electron doping the substrates.

As already indicated in table 1, it has been known for decades that the thermal decomposition of SiC leads to the formation of thin graphite on its surfaces, down to a monolayer

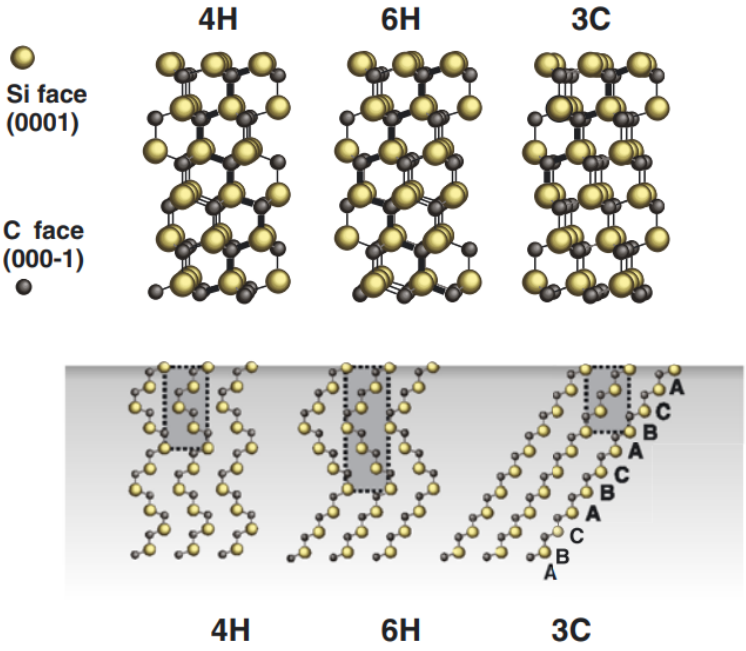

Figure 1.4: SiC polytypes 4H, 6H, 3C and their $(11\bar{2}0)$ plane. Reproduced from [44].

of graphene[26]. In 2004[3], the 2D nature of the electron gas in graphene on SiC was unveiled and the field of epitaxial graphene on SiC as an electronic material was opened. The amount of research performed on this material has been tremendous since then, and several review papers are available. See for example [45, 46, 47]. We will give a brief overview of this very rich field in this section.

1.3.1 Growth

The growth of graphene on SiC is an unusual one. In typical thin film technology, material is deposited from an external source (such as in the CVD process described above) and the thickness of the film is controlled by the amount of molecules brought to the surface of the substrate. Thermal decomposition of SiC, in a sense, is an inverted growth mechanism. When a piece of SiC is heated above 1000°C in ultrahigh vacuum (UHV) , silicon atoms desorb from the surface and leave behind them carbon atoms rearranging themselves into graphene layers. Its takes about three SiC bilayers to free enough carbon to form one layer of graphene; the SiC surface is therefore slowly depleted from material as the growth proceeds rather than having excess layers as in the usual deposition methods.

The rate of sublimation of Si atoms in UHV is controlled by the temperature of the substrate and the chamber pressure. It turns out that this rate surpass the time scale of reorganization of the carbon atoms in graphene and leads to a relatively disordered surface, with pits and high variations in the number of layers on the surface of one sample. To improve the quality of the films, the rate of sublimation can be slowed down using a background pressure of inert gas such as argon [48]. Silane (SiH_4) as been suggested as an alternative[49], and a method of confining the SiC to let the Si partial pressure built on its own and control the sublimation rate have been developed[50]. The latter method, called confinement control sublimation (CCS), is the one used in this work and the experimental details will be given in the next chapter.

1.3.2 Polar faces

The bilayer structure of hexagonal SiC implies that the (0001) face is terminated by Si atoms while the $(000\bar{1})$ face is terminated by carbon atoms. As such, they are referred to as Si-face and C-face. Commercial wafer are typically cut such that one side is the Si-face and the other is C-face. The growth mechanism is very different between those two surfaces, as it will be discussed in this section.

1.3.2.1 C-face epitaxial graphene

As the rate of sublimation of Si atoms is especially high on the $(000\bar{1})$ face of hexagonal SiC, it is difficult to control the growth of C-face epitaxial graphene even with improved methods. While monolayer patches can be produced[51, 52], most studies have been performed on multilayer graphene[53, 54, 55, 56]. Typical C-face growth using the CCS method yields five to ten layers, continuous and single crystalline over the surface of a one cm^2 sample. The main specificity of C-face graphene is the electronic decoupling between the layers. In graphite, the layers are Bernal stacked, where the sub-lattice B is aligned with the center of the hexagons of the top and bottom neighboring layers. This structure gives graphite different properties than those of multilayer graphene on the C-face where there is a rotational stacking preserving the A and B sub-lattice symmetry: the angles between the layers are such that each layer behaves as if it were an isolated graphene layer[55]. This

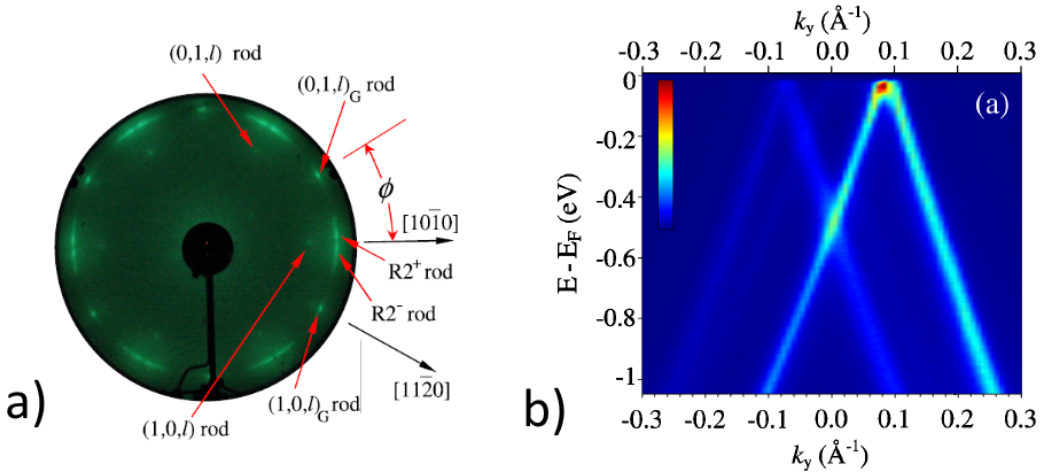

Figure 1.5: a) LEED image acquired at 72.2 eV from 4HSiC(000$\bar{1}$) C-face with 10 graphene layers, showing the graphene and SiC spots and the diffuse arcs labeled as the R2+ and R2 rods. The SiC [10$\bar{1}$0] (= 0) and [11$\bar{2}$0] directions are shown for reference. Reproduced from [54]. b) ARPES measured band structure of an 11-layer C-face graphene film grown on the 6H SiC. The ARPES resolution was set at 7 meV at $\hbar\omega$=30 eV. The sample temperature is 6 K. Reproduced from [56].

particular stacking is indicated by low energy electron diffraction (LEED) characterized by arcs in lieu of spots and confirmed by angle resolved photoemission spectroscopy[56] (Fig. 1.5a and b). Mobilities up to 10^6 $cm^2V^{-1}s^{-1}$ have been observed in the middle layers, which are close to charge neutrality[57], indicating the extremely high quality of this form of graphene. This is also confirmed by Raman spectroscopy (see section 2.1.2 for details on Raman) showing no evidence of D peak, the characteristic signature of lattice disorder and edges in graphene[58].

The main disadvantage of multilayer epitaxial graphene is, well, that it is not a monolayer. Top gated devices are limited by interlayer screening and only the upper layer charge carrier density can be significantly modulated[59]. In addition, the quantum Hall effect is not observed in those samples[60]. Monolayer C-face graphene has proven to be of good quality as well. Mobilities can reach 30000 $cm^2V^{-1}s^{-1}$ in the quantum Hall effect regime, and high frequency transistors have been fabricated[61]. The first C-face graphene layer has no or minimal interaction with the substrate which differentiates it from the Si-face, as we will see later. Growth of a continuous monolayer graphene over a wafer scale on the

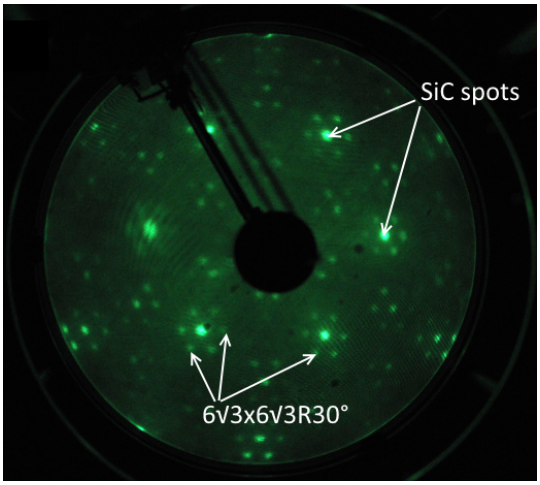

Figure 1.6: LEED pattern of a buffer layer sample grown by the CCS method.

C-face of SiC has so far not been demonstrated which appears to be the main challenge of this type of graphene.

1.3.2.2 Si-face epitaxial graphene

In contrast to the C-face, the growth of graphene happens at a much slower rater on the Si-face where layer by layer growth can be controlled fairly well[62]. One structural particularity is the presence of a $(6\sqrt{3}\times6\sqrt{3})\mathrm{R30}^{\circ}_{SiC}$ reconstruction in the first layer as observed in LEED patterns[26] and shown in Fig. 1.6. Note that in contrast to C-face graphene, the layers on the Si-face are Bernal stacked and therefore present the characteristics of thin graphite. The first layer is referred to as the buffer layer, as it does not display the properties of graphene. While many have classified this layer an inactive layer or merely a detriment to the properties of monolayer graphene on top of it[63, 64], recent studies have indicated that the buffer layer may be the long awaited ordered semiconducting form of graphene[65, 66, 67, 68]. Since it is the graphene layer of interest in this work, and that the interpretation of the transport results presented in chapter 4 and 5 relies strongly on the knowledge of the structural characteristics of the buffer layer, chapter 3 is entirely dedicated to the review of its properties. The layer growing on top of the buffer layer behaves as a single graphene, but its properties are still influenced by the substrate and the underlying buffer layer. Fig. 1.7 shows the ARPES intensity of such a sample[69]. Around E_F, the

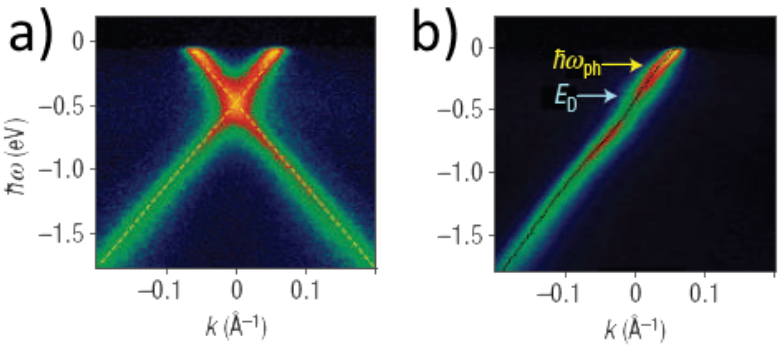

Figure 1.7: a) Experimental energy bands along a line through the K point parallel to the Γ-M direction. The dashed lines are an extrapolation of the lower bands (below E_F), which are observed not to pass through the upper bands (above E_F), suggesting the kinked shape of the bands around E_F. The electron density (per cm2) is indicated. b) Band map acquired in an orthogonal direction through the K point, for which one of the bands is suppressed. Reproduced from [69]

bands present a kink which has been interpreted to be a renormalization of the bands due to electron-plasmon coupling. Others have considered the possibility of a small band gap opening for a monolayer epitaxial graphene to explain this observation[70]. ARPES is only sensitive to states occupied by electrons. Therefore, there is no intensity measured above E_F and the charge density can be deduced from such measurement. For a monolayer epitaxial graphene on the Si-Face, the doping is n-type (electrons are the majority carriers) with a density of about 10^{13} cm^{-2}. The origin of the doping was interpreted to be due (at least partially) to the C-Si polarization at the SiC interface and to the buffer layer states[71]. This doping can be easily modulated by electrostatic potential (with a top gate for example)[3] or chemically: adsorption of molecules present in ambient air is enough to counter dope epitaxial graphene, converting the doping to p-type[51].

The electron (or hole) gas in epitaxial graphene is two dimensional by nature as it is confined to the plane of the graphene sheet, as demonstrated in early studies[3][72]. Magneto-transport experiments revealed a strong anisotropy of the magneto-resistance, indicative of that confinement, accompanied by Shubnikov-de Haas oscillations showing quantization of the electrons into Landau levels. This was further demonstrated in higher mobility samples with the observation of the quantum Hall effect[73], as previously observed in exfoliated graphene[29]. With increasing quality of the grown films, epitaxial graphene is

now considered as a serious successor to GaAs for resistance standard measurements, with the value of quantum resistance e^2/h defined by one of the plateaus in the Hall resistance as a function of magnetic field[74]. A signature of weak localization in two dimensions is also observed in the longitudinal magneto-resistance as a peak around B = 0 T. Compared to other forms of graphene, the mobility of the Si-face monolayer is relatively low, with $\mu \approx 1500 cm^2.V^{-1}.s^{-1}$ at room temperature. Reducing the charge density towards the Dirac point (with a top gate for instance) strongly increases the mobility, up to 30000 at 29 K[75].

1.3.3 Sidewall nanoribbons

Other form of graphene can be produced on the other facets of SiC. Graphene is known to nucleate first on the facet of natural steps of the Si-face[76]. Exploiting this property, artificial trenches can be patterned into the Si-face to serve as a template for graphene ribbon growth[56]. Sidewall graphene nanoribbons (SWGNR) thereby produced can sometimes behave as one dimensional ballistic channels for electron transport, mimicking the properties of carbon nanotubes[18, 77]. For a ribbon of width W and length L, the energy spectrum can be approximated by

$$E_{n,m} = \pm \hbar v_F \sqrt{(n\pi/W)^2 + (m\pi/L)^2} \tag{3}$$

where n and m are integers corresponding to the transverse and longitudinal modes respectively. It means that for a ribbon of width 40 nm at the charge neutrality point, $E_{1,0}$=82 meV which corresponds to 600K. So at room temperature, only the n=0 state is occupied. Ballistic conduction occurs when the mean free path of the charge carrier is much larger than the size of the device, and the electrons travel through the material without ever scattering. There is then no voltage drop along the device but there is a necessary drop of voltage at the interface between the ballistic conductor with only a few transverse modes and the contacting leads that have infinitely many modes. This induces a maximum of conductance of $\nu e^2/h$ where ν corresponds to the degeneracy of the lowest energy mode[78]. SWGNRs are shown to be ballistic conductors at room temperature, up to a record length of 16 μm, and display mobilities surpassing the theoretical limit for graphene[77]. The ballistic conduction is exclusively happening for the n=0 states, which can be seen by applying a top

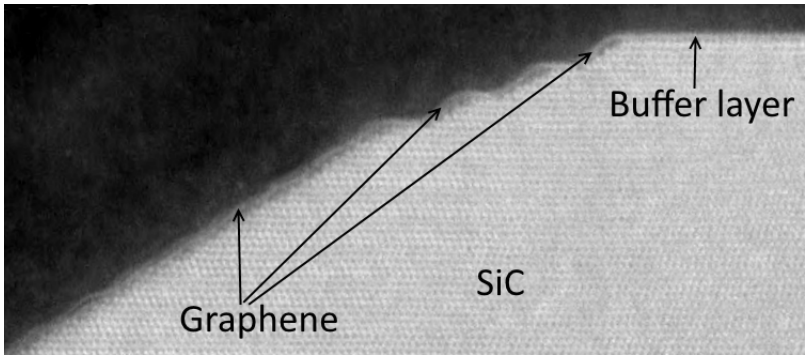

Figure 1.8: Cross sectional transmission electron microscopy image of a sidewall nanoribbon. The graphene is seamlessly connected to the buffer layer on the top terrace. Reproduced from [81].

gate voltage to populate the higher energy states. The increase in conduction when a new channel is opened is quite small and the corresponding mean free path of the extra channel is only around 50 nm, which is much shorter than the n=0 channel mean free path. Two n=0 channels are observed, one that vanishes exponentially for length greater than 160 nm and another one robust up to around 16 μm before vanishing too and the ribbons becoming close to insulating as the resistance is measured with varying spacing between probes in a four probe STM. This behavior is not predicted by any current theory on graphene and the underlying physics is the subject of on going research.

The properties of SWGNR have been investigated by diverse surface science techniques confirming the graphene structure of those ribbons[77, 79, 80, 81]. In particular, transmission electron microscopy (TEM) images of graphene ribbons grown on artificially etched SiC sidewalls (Fig. 1.8) show that the graphene layer forming the ribbon seamlessly turns into the buffer layer at the top. This characteristic will be exploited in the fabrication of buffer layer devices in chapter 4.

1.4 Motivations to study the electronic transport properties of the buffer layer

We have now introduced some elementary characteristics of graphene and some of its production methods. We have drawn special attention to epitaxial graphene as an electronic material. While layers on the carbon face of hexagonal SiC are isolated from each other, the layers are Bernal stacked on the silicon face and the substrate has an influence on their

electronic properties. Many studies have been performed in order to explain the nature of the buffer layer and how it influences the monolayer on top of it. Those studies have focused on surface science of the buffer, and an experimental investigation of electronic transport is missing. As we will see, electronic transport can be helpful to unveil some physics that goes beyond what surface science is able to show. In addition, the claim that the buffer layer is a good semiconductor has to be tested by fabricating electronic devices.

CHAPTER II

EXPERIMENTAL METHODS

This work is experimental in nature. Modern physics and material sciences are very rich in advanced tools giving the possibility to study in detail the structural and electronic properties of materials. In this chapter, I will present the experimental techniques used in the study of the epitaxial graphene buffer layer as well as some used in the literature review of next chapter. They are sorted into three categories: growth and surface science of graphene layers, micro and nano-fabrication of electrical devices and electronic transport characterization techniques.

2.1 Growth and characterization of epitaxial graphene

2.1.1 Confinement control sublimation process

As mentioned in the introduction chapter, epitaxial graphene on SiC was initially obtained by annealing pieces of a silicon carbide wafer in UHV conditions[26, 82, 3]. The confinement controlled sublimation (CCS) process, an improved growth method developed and used at Georgia Tech[50], consists in confining a piece of SiC into a small graphite crucible, heated by induction in high vacuum (see Fig.2.1). The crucible is closed except for a small leak hole allowing the slow escape rate of silicon vapor out of the enclosure.

During the growth of graphene, the sublimation of Si atoms from the crucible walls and from the sample increases the partial pressure to a value depending only on the temperature (see [83]). As a consequence, the graphene growth occurs close to thermodynamic equilibrium, at a rate solely determined (in theory) by the leak size. The improved quality of graphene grown via CCS compared to UHV grown samples was demonstrated in many studies: improved morphology[50], superior device performance[61], and higher crystallographic order[65] are observed.

The graphite crucibles used in a CCS furnace are initially conditioned by annealing them with dummy chips of SiC. Silicon is deposited on the inside walls of the crucible and

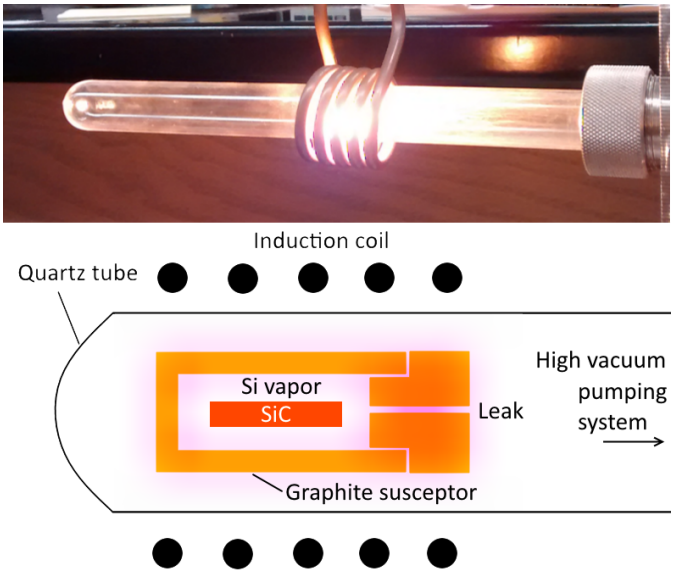

Figure 2.1: Confinement control sublimation furnace. Top: photograph of the furnace at 1400°C. Bottom: furnace diagram. Si gas sublimes from the crucible walls and the sample and is confined to the enclosure allowing close to equilibrium graphene growth.

form Si-C compounds at high temperature. The latter is suggested by a visible change in color and hardness of the inside of the crucible after conditioning. A re-initialization of the crucible condition can be achieved by baking it empty at high temperature so that silicon desorbs from the walls. For a better growth reproducibility between samples, each crucible is dedicated to one type of graphene growth such as multilayer graphene on the C-face, buffer layer, single layer graphene on Si-face, sidewall nanoribbons, and others.

In practice, our furnace is controlled by a proportional-integral-derivative controller (PID) . The temperature is measured by an infrared pyrometer detecting the intensity received from the infrared radiation of the hot crucible at two wavelengths centered around 1μm. The ratio of those intensities is related to the temperature according to Planck's theory of black body radiation. The Stefan-Boltzmann law gives the power P emitted from a black body of surface area A in terms of its temperature T:

$$P/A = \sigma T^4 \tag{4}$$

where $\sigma \approx 5.67\times10^{-8}$ $\mathrm{Wm^{-2}K^{-4}}$ is the Stefan-Boltzmann constant. The power set in the induction furnace is adjusted by the control loop according to the measured temperature. With the appropriate PID parameters, the crucibles temperature is increased from room

temperature to 1000°C in about 30 seconds with no overshoot. A mechanical pump and turbo pump combination gives the system a routine base pressure of 1e-6 mbar outside the crucible during growth. Pressure as low at 1e-7 mbar can be obtained after pumping for a couple hours. The system is systematically vented with Ar gas.

The growth of epitaxial graphene by the CCS method usually consists in three temperature steps. A first step at 800°C for 1200 seconds lets water and other loosely adsorbed impurities to desorb from the crucible walls and the surface of SiC. A second step between 1200-1250°C for another 1200 seconds is used for sublimation of the silicon dioxide that typically forms on SiC exposed to air, as well as to allow mass flow on the surface. The third step corresponds to the graphene growth and depends on the targeted result as well as the crucible size and conditioning.

2.1.2 Raman spectroscopy

Raman spectroscopy is a powerful and quick non-destructive measurement allowing a quantitative analysis of the growth of epitaxial graphene. It gives information on the number of layer, doping, disorder and strain in the atomic lattice[84]. Its usefulness and simplicity makes it an essential characterization step in the fabrication of buffer layer devices.

Raman spectroscopy relies on the inelastic scattering of monochromatic light by molecules. While most of the light matter interaction results in elastic scattering (known as Rayleigh scattering[85]), a small portion of the light is absorbed by the molecules and remitted with a shift with respect to the incident frequency. When this process involves a change in polarization of the molecule, i.e. a change of shape in the electron cloud, it is called Raman scattering (named after Sir C. V. Raman). If the process does involves an electronic transition, it is then called infrared absorption.

In a Raman scattering event, a molecule absorbs a photon and is excited into a higher energy virtual vibrational and electronic (sometimes called vibronic) state (i.e. short lived and not observable) before relaxing into a state different from the initial one. If the energy of the final state is higher than the energy of the initial state, the process emits a photon of lower frequency compared to the incident photon and the difference is called a Stokes shift.

If the final energy state is lower than the initial one, then it is an anti-Stokes shift.

Because the values of possible shifts are specific to the phonon modes and electronic structure of a material, Raman spectroscopy provides a signature of the nature of the chemical bonds present in the sample. In practice, it measures the intensity of the emitted light at different frequencies to produce a spectrum of the Raman intensity versus the frequency shift (traditionally given in cm^{-1}).

In monolayer graphene, there are three main Raman scattering events, leading to three signature peaks in the Raman spectrum, as shown in Fig. 2.2 with the example of quasi-free standing graphene (hydrogen intercalated buffer layer) on SiC. The G peak, around 1582 cm^{-1}, and the 2D peak, around 2700 cm^{-1}, are always present, while the D peak, at 1350 cm^{-1}, is only present if there is some structural disorder in the carbon lattice, i.e. a disruption of the lattice periodicity such as defects, edges or grain boundaries. In each events at the origin of the Raman peaks of graphene, an electron-hole pair is created in a Dirac cone by an incident photon. The G peak is a result of the inelastic interaction of this electron with an optical phonon of the graphene lattice to a lower energy excited state. The electron then recombines with the hole and emits a photon of a frequency lower than the incident one. The 2D peak comes from a more complex process where a phonon scatters the excited electron into an different Dirac cone, and a second phonon scatters the electron back to the initial Dirac cone. Finally, the D peak is a process similar to the 2D peak but the electron is scattered back into the initial Dirac cone by a defect or a boundary (such as the edges of a ribbon).

To measure the Raman spectrum of epitaxial graphene and the buffer layer, we used a Horiba Jobin Yvon LabRam HR, equipped with a 532 nm laser focused on the surface of the sample by a 100x Olympus MPlan N microscope objective. A monochromator filters the emitted light to one frequency at a time and the photointensity is measured by a CCD detector. The difficulty in measuring the Raman signal of epitaxial graphene on SiC comes from the fact that SiC itself has a strong Raman emission in the range of frequency between 1200 cm^{-1} and 2000 cm^{-1}. A systematic background subtraction is necessary to extract the weaker graphene signal in that frequency range, as depicted in Fig. 2.2.

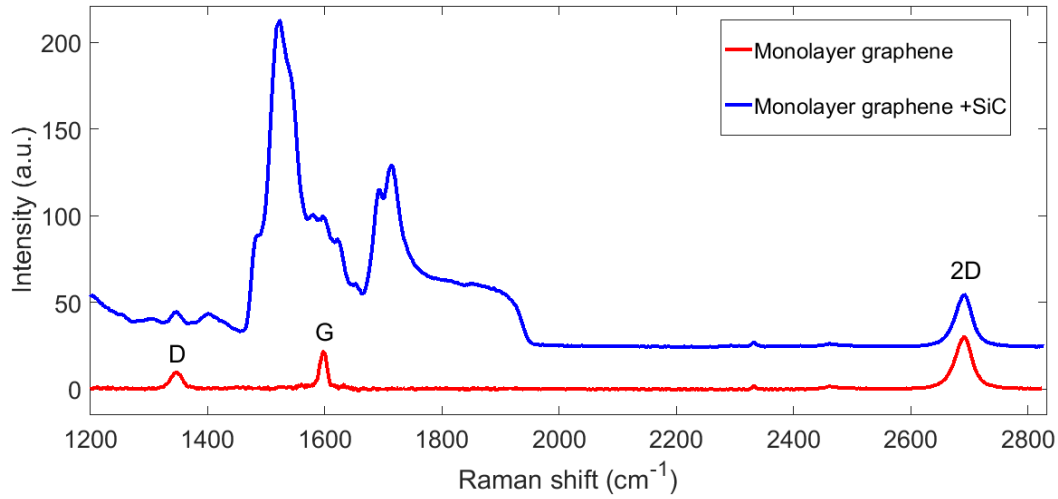

Figure 2.2: Raman spectra of quasi-free standing monolayer graphene on SiC Si-face. The blue spectrum (on top) is the raw data. The red curve (below) is the spectrum after subtraction of the bare SiC background

2.1.3 Scanning probe microscopy

Raman microscopy can be used to spatially characterize the surface of epitaxial graphene. However, the resolution is limited to about 1 μm in our system. Scanning Probe Microscopy (SPM) is a set of complementary tools with much better spatial resolution, each one of them providing a different type of information.

As human we used our tactile sense everyday to get insight on the texture of the objects surrounding us. As we pass our fingers across a surface, even without looking at it, we can detect whether it is flat or bumpy, smooth or rough, and slippery or more sticky. In a sense, SPM does the same, but at a much smaller scale that what we are able to sense with our fingers.

Atomic force microscopy (AFM) measures the topography of the surface of materials, lateral force microscopy (LFM) is sensitive to the variation in friction of those surfaces, and electrostatic force microscopy (EFM) measure their electrical properties. Other techniques are also available to measure the magnetic properties and work function of surfaces, as well as to locally measure the conductivity current in a sample. Scanning Tunneling Microscope (STM) is another SPM technique, originally developed in 1983 at the IBM Zurich research laboratory[86] and preceding the invention of all other SPM techniques. It measures the

tunneling current between a conductive tip and the sample, and can provide atomic resolution imaging. This section introduces the SPM techniques that are useful to characterize the buffer layer.

2.1.3.1 Atomic Force microscopy

AFM was developed in 1986, again by IBM researchers, adapting the principles of the STM[87]. It is based on the short-range forces acting at the surface of a sample. Those forces are repulsive near the surface (distance < 2-3 Å) due to Pauli repulsion of overlapping electron orbitals and attractive otherwise due to Van der Waals forces. The interactions between a sharp probing tip and such forces can be approximated by the Lennard-Jones potential, represented in Fig. 2.3a.

The simplest AFM mode available is called contact AFM (C-AFM) . In C-AFM, a sharp tip scans the sample at a distance of the surface where the forces are repulsive. This tip is situated at the end of a cantilever with very low spring constant $k_{cantilever} < 1$ N/m. The cantilever bends up and down as the tip follows the topography of the surface as depicted in Fig. 2.3b. A laser beam is reflected on the back of the cantilever towards a position sensitive photo-detector (PSPD) . The position of the laser spot on the PSPD is recorded over time by a computer software and converted into a topography map of the surface.

C-AFM is defined by a set-point, which corresponds to the magnitude of the force applied by the tip on the sample. It is typically taking values between 2 and 10 nN. Higher set-points can be used to scratch the sample and perform some kind of nanolithography[88].

The contact mode comes with a couple of issues. First, because the tip is in "contact" with the surface in C-AFM, it wears out fast and the imaging resolution decreases overtime. Second, the presence of adsorbed water and nitrogen on the sample in ambient conditions causes the formation of a meniscus between the tip and the surface which can change the nature of the interaction. Despite those issues, C-AFM provides a good imaging capability. It is also the operating mode for acquiring LFM data, as we will discuss later in this chapter.

In order to overcome the issues originating from the tip being in contact with the surface, a non-contact AFM mode (NC-AFM) was developed[89]. In this technique, the tip hover

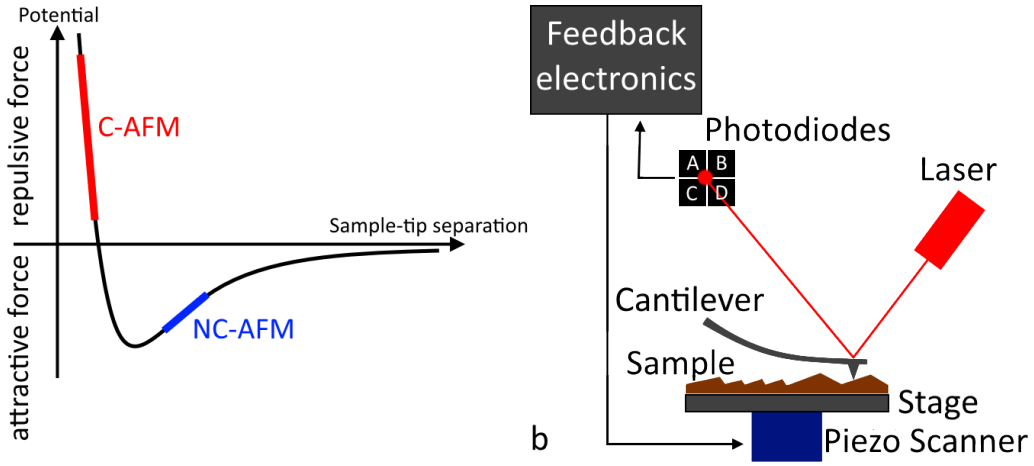

Figure 2.3: Principle of AFM. a) Lennard-Jones potential describing the interactions between the short range forces of the surface and an AFM tip. C-AFM operates close to the surface while NC-AFM operates further away from it. b) Basic elements of an AFM. A 4-segment photodiode measures the changing reflection of a laser on the back of the cantilever, flexing due to the height variation on the sample.

over the sample at a distance where the forces are attractive, further away than in C-AFM where the tip is considered to not be in contact with the surface (see Fig. 2.3a). The magnitude of these forces is weak and it is therefore not possible to measure the deflection of the cantilever directly like in C-AFM. The cantilever is for into oscillation at a frequency near its resonance frequency and the change in phase and oscillation amplitude induced by the surface forces are detected. More technically speaking, the gradient of the surface forces on the cantilever changes its intrinsic spring constant k_0 into an effective spring constant k_{eff} following this equation[90]:

$$k_{eff} = k_0 - grad(\mathbf{F}) \tag{5}$$

The resonance frequency shifts from the value k_0. as a result, the amplitude of oscillation changes as well. NC-AFM uses a feedback loop to keep this amplitude constant by adjusting the distance from sample to tip and the topography is thus recorded.

In certain conditions, sub-atomic resolution can be obtain in NC-AFM[91], but our setup routinely gives only 10 to 30 nm lateral resolution, limited by the radius of curvature of the end of the tip. The system used in this thesis is a Park Systems XE-70. Contact tips are purchased from AppNano, and the model is called SHOCONA. Non-contact tips are

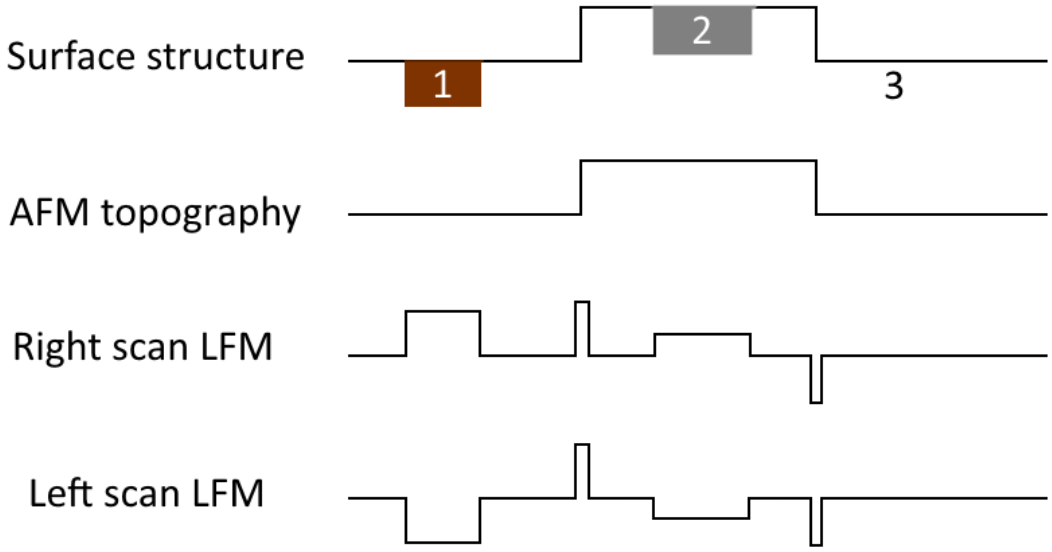

Figure 2.4: Illustration of LFM signal. The surface structure contains topography features and is composed of 3 different materials (labelled 1, 2 and 3) with different frictional coefficient μ such that $\mu_1 > \mu_2 > \mu_3$. Topography features are independent of scan directions in LFM signal because it laterally bends the tip in the same direction while the frictional forces signal changes sign between left and right scan.

PointProbe-Plus™-NCHR made by the company Nanosensors.

2.1.3.2 Lateral Force microscopy

Now that we have described two different AFM modes useful to measure topography, we will describe lateral force microscopy, a very important technique to characterize epitaxial graphene.

While topography indicates the structural order of the surface, lateral force microscopy helps determine what material it is made of and whether or not it is homogeneous. For epitaxial graphene on the Si-face for example, one can have a mixture of SiC or SiO_2 with the buffer layer, a monolayer and a bilayer graphene. While topography changes can be associated with those different types of surface, the presence of SiC natural steps makes it difficult to interpret them. LFM provides a contrast between each of those materials by detecting the differences of friction on the surface.

LFM is performed using the exact same setup as C-AFM. In addition to recording the vertical position of the laser spot on the detector, the horizontal position is also recorded

over time. The lateral deflection of the cantilever is due to the force experienced by the tip as it scans the surface horizontally. Its magnitude depends on the surface frictional coefficient, the topography, the direction and speed of the cantilever scan and on the lateral spring constant. Fig 2.4 illustrate the deflection of the cantilever due to topography and friction. Because the contribution from topography is independent of the scan direction, a subtraction of the left and right scans gives a contrast image that solely reflects the frictional forces.

2.1.3.3 Scanning Tunneling Microscopy

STM utilizes the quantum tunneling effect. In the quantum realm, an electron has a certain probability to go through an energy barrier even if its own energy is lower than the barrier height, as long as the wall are thin enough[92]. In STM, a voltage is applied between a sharp tip and the surface of a material, usually in an UHV chamber. As the distance between the tip and the surface is reduced to several Angstroms, electrons start tunneling through the gap in between. The tunneling current varies exponentially with the gap width[86], making this technique extremely sensitive to height variations. As the tip is scanned across the surface, the current can be maintained constant by a feedback loop that changes the distance between tip and sample and those variations are recorded over time to produce a topography map of the surface. Alternatively, the surface can be scanned at a constant height while measuring the variation in the tunneling current, at the risk however to crash on unexpected protuberances.

The tunneling current is proportional to the local density of state (LDOS) of the surface. A perfectly flat surface with varying LDOS would result in a contrasted STM image that is not reflecting the topography. A STM image is therefore always a convolution of topography and LDOS and it can be delicate to interpret it. The LDOS of a sample can however be measured at each spacial point by sweeping the voltage and recording the current-voltage characteristics (IV curve). The derivative of this curve, or $\frac{dI}{dV}$, is proportional to the LDOS. This measurement is referred to as scanning tunneling spectroscopy (STS).

2.1.4 Low energy electron diffraction

We are now introducing low energy electron diffraction (LEED), which exploits the diffraction properties of incident electron wave functions onto an array of atoms. The surface of a single crystal material is bombarded with a collimated beam of electrons (with incident energy of 20-200 eV). The diffracted electrons are collected on a fluorescent screen, forming diffraction spots[93]. This phenomenon was discovered in 1927 by Clinton Davisson and Lester Germer[94], which at the time confirmed the postulate of wave-particle duality hypothesized by Louis de Broglie in 1924[95]!

LEED is surface sensitive as the incident electrons leave the surface only if they scatter near the surface. It is therefore perfectly suitable for the study of epitaxial graphene as it is a 2D crystal. Samples are mounted on a heating stage in UHV where the surface can be desorbed of contaminants by annealing it. Monochromatic electrons are ejected from a hot cathode held at a negative voltage with respect to the sample before being accelerated and collimated by a series of electronic lenses. Recalling basic diffraction theory, for a beam of electrons accelerated at voltage V (with momentum $\boldsymbol{k_{incident}}$) normally incident to a 1D array of atoms with lattice constant a, constructive interference occurs for scattered electrons with a momentum $\boldsymbol{k_{scattered}}$ making an angle θ with $\boldsymbol{k_{incident}}$ such that:

$$n\lambda = asin(\theta) \tag{6}$$

where n is an integer and $\lambda[nm] = \sqrt{\frac{1.5}{V}}$ is the wavelength of the incident electrons.

This, of course, does not suffice to explain fully the origin of the diffraction pattern in LEED, but captures the essence of diffraction. As discussed in the introduction chapter, graphene is a periodic 2D lattice that can be defined by its unit cell and the unit vectors $\boldsymbol{a_1}$ and $\boldsymbol{a_2}$ (see Fig. 1.2a). The reciprocal lattice is determined by the reciprocal unit vectors $\boldsymbol{b_1}$ and $\boldsymbol{b_2}$ (Fig. 1.2b). The constructive interference occurs when the Laue condition is fulfilled:

$$\boldsymbol{k}^{\parallel}_{\boldsymbol{scattered}} - \boldsymbol{k}^{\parallel}_{\boldsymbol{incident}} = h\boldsymbol{b_1} + k\boldsymbol{b_2} \tag{7}$$

Since $k^{\parallel}_{incident}$ (component parallel to the surface) is null for a normally incident beam, $k^{\parallel}_{scattered}$ is directly reproduced on the screen. The LEED pattern is therefore a direct

representation of the reciprocal lattice of the surface.

LEED is sensitive to only a few atomic layer into the material. For epitaxial graphene on SiC, it is then expected to observe a superposition of signals coming from the graphene layer(s) and the top layers of SiC. Additional features resulting from multiple scattering between layers can arise as well and the interested reader may go to reference [93] for more information.

2.1.5 X-ray photoemission spectroscopy

We are ending this section with a short description of X-ray photoemission spectroscopy (XPS). This advanced technique is based on the photoelectric effect, which is the emission of an electron (referred to as a photoelectron) from a surface due to the absorption of light. It was discovered by Heinrich Hertz in 1887 and explained by Albert Einstein in 1905, which led him to receive the 1921 physics Nobel prize. Robert Millikan experimentally confirmed Einstein hypothesis in 1914, and received the 1923 physics Nobel prize for this work. When the frequency of a photon hitting the surface of a material is larger than the binding energy of an electron in the material, an electron can be ejected from the surface with a maximum possible kinetic energy corresponding the the difference between the photon incident energy and the electron binding energy.

XPS tools are commercially available. Their development has been made possible after studies led by Kay Siegbahn[96] in the 1950s, research for which he was awarded (another one!) the 1981 physics Nobel prize. The sample is placed in a UHV chamber in order to give a meter size mean free path for photoelectrons traveling from the sample to the detector. X-rays can be obtained by emitting electrons from a hot cathode and accelerating them into an anode (typically made of aluminum). When they hit the anode, the deceleration causes the electrons to radiate X-rays which are subsequently filtered and focused to create a beam of monochromatic X-rays. An alternative way to produce high intensity X-rays is to use a synchrotron. Electrons are accelerated to relativistic velocities in a circular motion and eventually wiggled by a series of magnets to produced synchrotron radiation of X-rays.

XPS gives precise information on the chemical composition of the surface of samples,

its contaminants, the stoichiometry of the species and even the chemical bonding between atoms. This information is determined by the specific binding energy of core level electrons, tightly bound to the nucleus. An XPS spectrum is a plot of the intensity of detected photoelectrons versus their binding energy. Each peak of the spectrum is associated with a specific atomic and molecular orbital. C1s for example refers to the electron lying on the s-orbital of the first shell of a carbon atom. Shift in the binding energy from an isolated atom are caused by the polarization of the electron cloud when the atom bonds with another one, and that polarization depends of the nature and number of the bounding atom. Hence, the binding energies of C1s for sp_2 hybridized C-C, sp_3 hybridized C-C, C-Si, C-O, C-H, etc., will all be different from each other, shifted from the original C1s binding energy.

The photoelectric effect can also be utilized to probe the binding energy of valence and conduction electrons. If the momentum of those electrons is also measured, then the band structure of the sample can be reconstructed. Such a measurement is made possible by angle resolved photoemission spectroscopy (ARPES). In ARPES, the energy of photoelectrons is measured for different angles the surface is making with respect to the detector, which is then be converted into a map of the energy versus momentum in the k_x and k_y direction. Therefore, ARPES measurements give the band structure of the surface of 3D materials, and the direct band structure of 2D materials.

2.2 Micro and nano-fabrication

While this work relies strongly on the surface science techniques that have been presented thus far, the core of this thesis is the study of the transport mechanism in the buffer layer. Once the buffer layer is grown and characterized, various devices are built out of it with conventional micro and nano-fabrication techniques. This section will describe those techniques.

2.2.1 Electron-beam lithography

Lithography techniques are used in microelectronics to produce patterns on a sample or wafer. The two most common types are optical lithography and electron-beam lithography (EBL). In both cases, the sample is covered with a polymer material (called a *resist*)

which solubility in a specific solvant (called a developer) depends on the exposure to light or electrons. While optical lithography is compatible with large scale production, resolutions below 1 μm require advanced pieces of equipment that are generally not available on university campuses. On the other hand, because of the smaller wavelength of electrons compared to photons, EBL is able to produce features under 10 nm resolution[97]. The downside however, is that the resist is exposed one point at a time. This makes EBL much slower than optical lithography, which can expose a whole wafer to UV light at once through a mask. As we only study a few devices at a time, EBL is perfectly suitable for our work.

The resist is deposited on a sample by spin coating. The resist is dropped on a sample, subsequently rotated at several thousands rpm giving a thin and homogeneous layer. The sample is then baked on a hot plate to evaporate the solvents, leaving a solid polymer film.

The choice of resist is important and there are two types: the exposed parts of *positive* tone resist are dissolved when dipped in a developer, while *negative* tone resist remains only where it has been exposed. We use poly(methyl methacrylate) dissolve in 6% (PMMA 950 A6) as a positive resist and Ma-N 2400 as a negative resist, both purchased from MicroChem. Following MicroChem's recommendation, the developer for PMMA is a 3:1 mixture of isopropyl alcohol (IPA) and methyl isobuthyl keton (MIBK)[98]. Although not specifically designed to develop Ma-N 2400, we use the developer MF-319[99].

Next, the sample is placed in a scanning electron microscope (SEM) for exposure. A software allows the user to control where the electron beam exposes the resist, usually by the means of a CAD drawing. The exposure time (corresponding to an e-beam "dose") for each point has to be determined accurately, as under exposure leads a pattern not fully developed, and over exposure may result in the pattern being washed away after during the resist development. A dose test consist in producing the same pattern repeatedly and slowly incrementing the exposure time for each to determine the most suitable dose for a specific pattern and/or substrate.

The sample is subsequently dipped into the developer and the exposed (or unexposed, depending on the tone of the resist) parts of the resist are dissolved resulting in a customized microscale mask. At this point, an etch process or a thin film deposition can be performed

and the resist is finally washed away completely by an appropriate solvent such as acetone or 1165 resist remover.

The making of a device often requires multiple steps of lithography. In order to align the current pattern with the pre-existing features of the sample, an alignment step is necessary. Alignment marks are either deposited in the form of metal crosses or, if PMMA is used as the resist, alignment marks are patterned and developed first providing an optically visible landmark around the existing pattern. Optical pictures are then taken in order to quantify the position of the pre-existing features with respect to the alignment marks.

All devices in this thesis were fabricated using a JEOL JSM-5910, a SEM equipped with a beam blanker.

2.2.2 Reactive ion etching

Nanofabrication always involve the removal of material at some stage of the process. Reactive ion etching (RIE) is a dry etch method involving chemical reaction of the surface of a material with the ions of a plasma. One or more gases are sent to a chamber where they are ionized by a high frequency or DC electromagnetic field. For instance, the carbon atoms in graphene react with the energized oxygen ions in the plasma to form volatile CO_2. In the making of sidewall nanoribbons, SiC is etched using a mixture of SF_6 or CF_4 and O_2. In some cases, an argon plasma can be used in which case the etching occurs by sputtering of the material without involving any chemical reaction.

E-beam resists are not very resistant to oxygen etch, but this is not a concern as their thickness is relatively large compared to one or a few graphene layers, so that graphene is fully etched away before the resist disappears.

2.2.3 Thin film deposition

Thin films are layers of material ranging from a monolayer (like graphene) to several microns thick. Metal thin films are used as drain and source materials, top gates, or interconnects, while dielectric thin films serve as gate insulators or as protective and capping layers[97]. We use thin film technology for all the above purposes in the making of buffer layer devices.

There are two main processes of deposition of thin films: chemical and physical deposition.

2.2.4 Chemical deposition

Chemical deposition involves the reaction of one or multiple precursors (in the form of a gas or a liquid) at the surface of a substrate, leaving a solid layer after the process. Atomic layer deposition (ALD)[100], chemical vapor deposition (CVD)[101] and electroplating[102] are examples of chemical deposition. They tend to be non directional, meaning that the obtain film will cover most of the exposed surface, including sidewalls, with minimal thickness variation.

We use ALD for the deposition of aluminum oxide (Al_2O_3) which serves both as a insulator for top gated buffer layer devices and as a protective layer to prevent air contamination on the buffer layer (see section 4.1.3). Trimethylaluminum (TMA, $Al_2(CH_3)_6$) is sent into the chamber in a short pulse and chemisorbs on the hot surface (200°C) while the remaining gaseous TMA is pumped out. Water vapor is then sent in a sequential pulse and reacts with the adsorbed TMA. CH_3 forms CH_4 with the hydrogen of water and Al reacts with oxygen forming one atomic layer of Al_2O_3 as this reaction is self-terminating. The process is repeated for many cycles until the desired film thickness is reached. ALD is a selective method of deposition, where the growth mode depends on the substrate. Three growth modes are identified in the literature[100]: Frank-van-der-Merwe is the ideal growth mechanism where the film is deposited layer by layer, Stranski-Krastanov growth first nucleates as a layer but quickly forms islands once the substrate is covered, and Volmer-Weber growth nucleates into separate islands. The latter case is the worse case leading to a rough surface and potentially numerous pinholes in the film.

Al_2O_3 deposition by ALD on pristine graphene is known not to work: indeed, a graphene surface free of defects is chemically inert[103]. Numerous methods have been proposed to overcome this problem[104], one being to deposit a seed layer of Al_2O_3 using a physical process rather than a chemical one. We adopted this solution in our fabrication scheme.

2.2.5 Physical deposition

Physical deposition techniques can be made a lot more directional than ALD, with minimal coating on sidewalls of the material and resist. As we already mentioned, it is less sensitive to the chemical reactivity of the surface. They are preferred for the lift-off process, described later in this section. Magnetron sputtering deposition[105], thermal evaporation[97] and electron-beam (e-beam) evaporation[106] are examples of physical deposition. We use a thermal evaporator to deposit aluminum oxide directly on graphene and the buffer layer and as a seed layer for ALD. A metal boat, typically made of tungsten, is heated by passing a high current through it (I >100 A). The boat contains pure aluminum pellets which melt when the boat temperature reaches the melting point of Al at 660°C. This source is placed in a vacuum chamber and the sample is placed in front of it. Because of the long mean free path of evaporated particles in a vacuum of 1×10^{-7}, they travel directly to the sample where they slowly form a thin film. The thickness of deposited material is monitored by a piezoelectric crystal which frequency changes with the thickness of the film deposited on it. In vacuum, the film has the same composition as the source (in this case, Al). To create an aluminum oxide film, a low pressure (around 1×10^{-5}) of pure oxygen gas is introduced near the source to oxidize the Al particles before deposition on the sample[107].

Metal thin films are used to contact graphene and/or the buffer layer. Titanium (Ti), palladium (Pd) and gold (Au) are commonly used for contacting graphene. E-beam evaporation is a better suited technique to evaporate those metals compared to thermal evaporation, as it avoids any possible contamination from the boat. An E-beam evaporator (see Fig. 2.5) is composed of a high or ultra high vacuum chamber, metal sources in refractory crucibles, an E-beam source, a shutter to control the deposition time precisely, a sample stage and a crystal monitoring the deposition rate and thickness of the film. The e-beam is focused onto the metal source by a magnetic field to locally melt it. This local heating and the fact that the crucible is water cooled ensure that the crucible containing the metal source does not heat up to too high temperature as it does in thermal evaporation. multiple sources are stored in the chamber and can be selected remotely, allowing sequential depositions without exposing the sample to air. The sample is placed on a stage situated 50 to 100 cm away

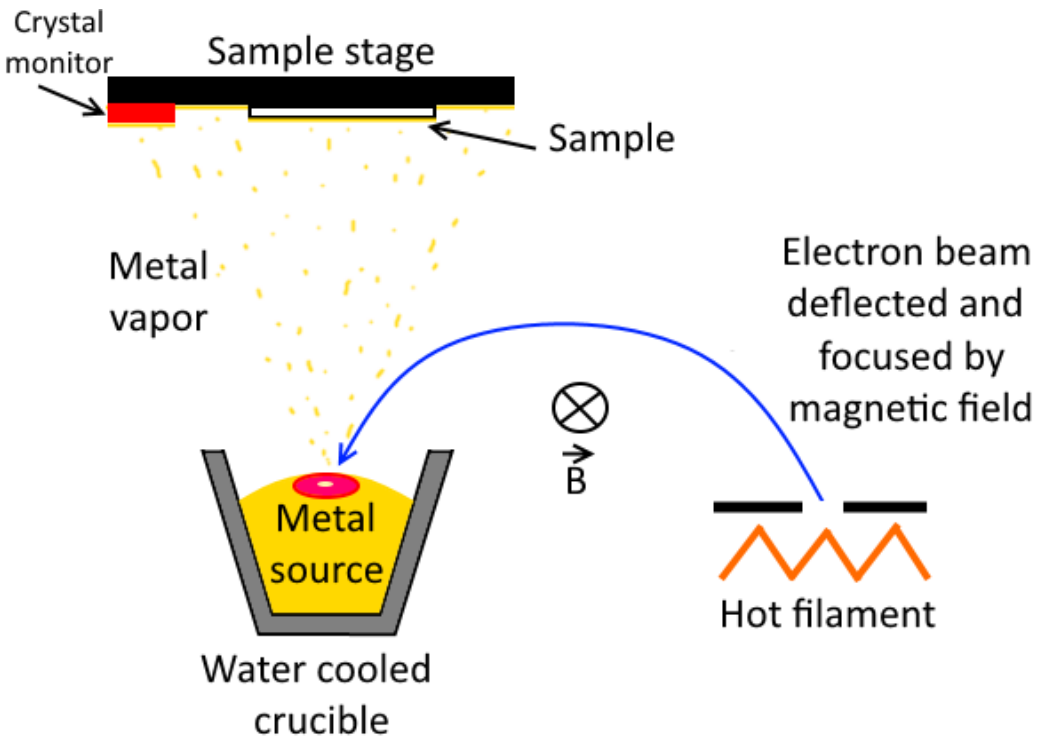

Figure 2.5: Principle of e-beam evaporation. A beam of electron is focused on the metal source to melt it locally. The metal vapor travels to the sample through the high vacuum chamber and the deposition is monitored by the crystal monitor.

from the source. On some evaporators, the stage can rotate continuously during deposition to enhance the film uniformity.

We typically use a double layer consisting of 20 nm of Pd deposited at a rate of 0.7 Å/s on the graphene and 30 nm of Au deposited at 1 Å/s on top of it.

2.2.6 Lift-off

In order to produce patterns of metal films, the so called lift-off method is used. A pattern is written on a positive tone resist (PMMA) and developed, leaving resist solely around the pattern. The metal film is then deposited. After deposition, the resist is dissolved in an appropriate solvent and the film deposited on top of the resist is "lifted off" the sample, while the film inside the developed pattern remains. It is important for the deposition to be as directional as possible to prevent deposition on the sidewalls of the resist and the film to be discontinuous at the edge of the pattern, otherwise the film made be washed away everywhere.

2.2.7 Typical process flow

We have now introduced all the fabrication techniques used to make buffer layer devices. Fig 2.6 show a typical graphene device fabrication process flow, from the growth of graphene to the device being ready for electrical characterization.

2.3 Transport measurement

We end this chapter with a presentation of electronic transport measurement techniques. They consist in measuring electrical resistance in various conditions, such as in magnetic field, as a function of temperature or the composition of environment.

2.3.1 Four point probe stations

Many resistance and resistivity measurements involve four leads (Van der Pauw method and Hall effect measurement[108], four point probe technique[109], etc.), hence the development of four point probe stations. Four sharp metallic tips are placed on stages capable of micrometric displacement in all three directions. The tips can be lowered directly on a

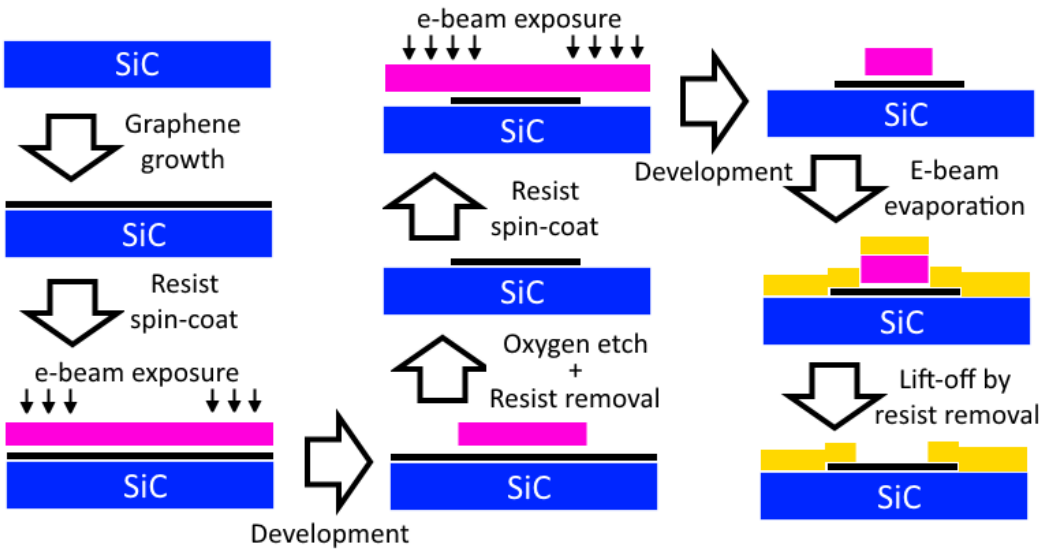

Figure 2.6: Typical process flow for epitaxial graphene device fabrication. If sidewall nanoribbons are part of the device design, a lithography and RIE steps are added before the growth of graphene. Top gated devices requires to add multiple lithography and deposition steps at the end.

sample, or on lithographically patterned lead pads. Two of them are usually used to inject current and the two others are measuring a voltage.

For low enough resistance (on the order or less than 1 $M\Omega$), a lock-in amplifier is well suited to perform electrical characterization. The current is injected by applying a low frequency (10-20 Hz) AC bias voltage V_{bias} across a series resistance R_{series} much larger than the sample resistance. This induces a known AC current $I = V_{bias}/R_{series}$ through the sample. The response of the device to that input current is a measured voltage V_{meas} with same frequency as I. Exploiting the orthogonality of sinusoidal functions (defined as $\int_0^\infty \sin(\omega_1 t)\sin(\omega_2 t)\mathrm{d}t = 0$ for $\omega_1 \neq \omega_2$), the lock-in integrates the product of the output and input signals over time to cancel any signal with a frequency different than the set frequency, such as random noise.

Our lab is equipped with a probe station operating in air and one operating in vacuum or in a specific environment such as pure oxygen or nitrogen. In addition, a resistive heater made of a nichrome wire allows to anneal the sample off of its adsorbates in the vacuum probe station (up to 400°C). On the other hand, the air probe station allows for a quick Hall measurement (see next section) as a small permanent magnet (0.15 T) can be inserted

just below the sample. Much stronger magnetic field (up to 9 T) can be obtained with the superconducting magnet of our cryostat.

2.3.2 Low temperature transport

A cryostat is an advanced type of refrigerator capable of reaching cryogenic temperatures. Our system is a cryogen-free (no need to fill it with liquid helium) superconducting magnet with variable temperature insert from Cryo industries of America, Inc. It is equipped with a two stages cold head from Sumitomo Heavy Industries operating on the Gifford-McMahon refrigeration cycle. Basically, helium gas is compressed to high pressure (300 PSI, which is about 20 times the atmospheric pressure) in a compressor and expanded in the cold head resulting in cooling power.

This cools down the magnet to about 3.3 K. Heat exchange to the sample is controlled by the presence or not of He both in the sample space and the tube surrounding it, which allows to operate the superconducting magnet below 4 K while the sample is held at high temperature. The temperature in the sample space can be varied from 4.2 K to 420 K thanks to a resistive heater placed next to it. A lower sample temperature of 1.6 K can be obtained by pumping on the surround tube thereby reducing its pressure of liquid helium in the same volume and therefore its temperature. To maintain that temperature over time, the quantity of pumped He and injected He gas must be balanced. Finally, four resistive sensors monitor the temperature in the sample space, the magnet, and the two stages of the cold head.

Electrical connections with the outside are made possible via feedthroughs all the way to a sample holder. The sample is glued and wirebonded to a chip carrier which is plugged in the sample holder.

The sample can be oriented either perpendicular or parallel to the magnetic field, by choosing the appropriate sample holder. In the perpendicular to the field configuration, the Hall effect can be measured. As mentioned previously, this can be performed on a sample at room temperature, which comes handy in the case of the highly insulating buffer layer at low temperatures (section 4.5.2). The Hall effect is used to measure the charge carrier

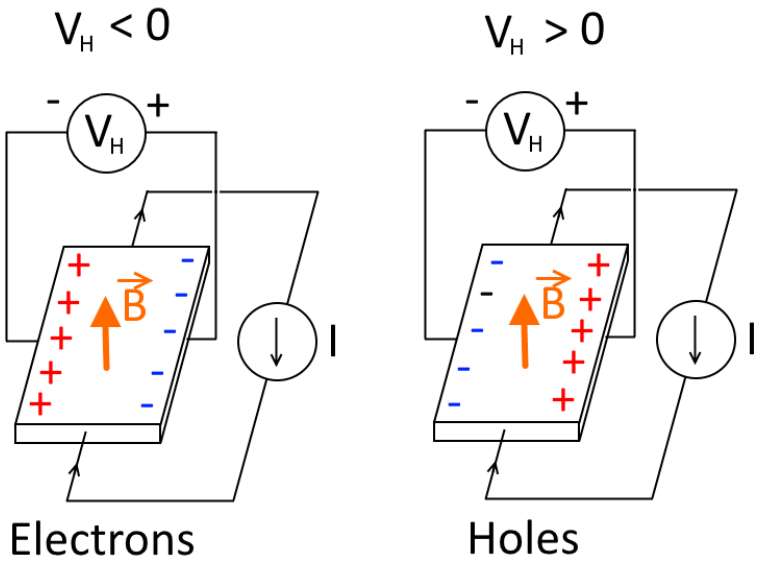

Figure 2.7: The Hall effect for negative charge carrier (electrons) and positive ones (holes). The sign of the Hall voltage depends the sign of the charges.

type and concentration in semiconductors. It originates from the magnetic component of the Lorentz force $\boldsymbol{B}$ experienced by a charge q (positive or negative) moving at a velocity $\boldsymbol{v}$ in a material subject to a magnetic field $\boldsymbol{B}$:

$$\boldsymbol{F_m} = q\boldsymbol{v} \times \boldsymbol{B} \tag{8}$$

Therefore, a magnetic field perpendicular to the plane of the electrical current I in a thin slab (thickness t) causes the charge carriers to deviate towards one side of the slab. They accumulate on the side inducing a potential difference V_H in the slab perpendicularly to the direction of current as depicted in Fig. 2.7. The Hall coefficient, defined as $R_H = \frac{V_H t}{BI}$ is related to the charge density n and charge carrier sign:

$$R_H = \frac{1}{qn} \tag{9}$$

If one also measure the conductivity σ of the material, the knowledge of n allows to extract the carrier mobility μ as $\sigma = ne\mu$.

CHAPTER III

REVIEW OF THE EPITAXIAL GRAPHENE BUFFER LAYER

This chapter is dedicated to an overview of the buffer layer. Information on the atomic and electronic structure of the buffer layer is crucial in order to interpret the transport properties given in chapter 4 accurately. While many groups have attempted to characterized the buffer layer with surface science techniques, the nature of the interactions between the carbon atoms of the buffer layer and the silicon atoms of SiC remains a subject to controversies. My interest here is to first give the reader an understanding of the atomic morphology of this unique graphene layer. Second, most of those results have served as references for the production and quality check of the buffer layer samples produced throughout this thesis research work. Therefore, some of the figures contained in this chapter are my own data. Others will be annotated with a reference.

3.1 Atomic structure

Chemical functionalization has been one avenue to produce a semiconducting form of graphene. The chemical bonding of atomic species at the surface of graphene breaks the A and B sub-lattice symmetry and can create a band gap[110, 111]. The main hurdle with this path is the inherent disorder brought by the functionalization of the sp^2 bonds.

A more ordered functionalization can also be triggered by interactions with the substrate. Logically, this process is dependent on the strength of those interactions, the ordering of the substrate itself and the alignment between the substrate and the graphene lattice. There are no evidence for example that the $(000\bar{1})$ face of SiC induces a functionalization of the first layer of C-face graphene, while the (0001) face does. Some kind of "buffer layer", i.e. a graphene layer functionalized to the point of making the Dirac cone vanish, have been observed for epitaxial graphene on certain metals. In some cases such as graphene grown epitaxially on iridium, the incommensuration between graphene and the substrate merely imposes a Moiré pattern and induces replicas cones and minigaps in the band structure

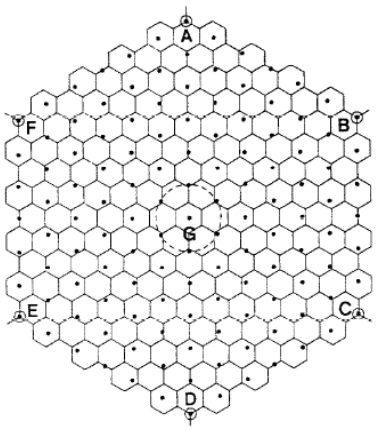

Figure 3.1: A model of a graphene layer (honeycomb lattice) grown on 1x1 Si-terminated β-SiC(111) (dots). A,B,C,D,E and F indicate positions where the C atoms on the top layer coincide exactly with the Si atoms on the second layer. The dotted circle, G, outlines positions where the C atoms and Si atoms nearly coincide. The graphene honeycomb spacing is 2.46 Å and the Si-Si spacing is 3.1 Å . Reproduced from [114].

as observed in ARPES measurements[112]. In other cases however, the band structure is profoundly modified. For instance, the first epitaxial graphene layer on ruthenium is also a true graphene layer but periodically interacts with the underlying substrate giving rise to a large corrugation following a Moiré pattern on top of the graphene 1×1 structure[39]. The band structure does not have a Dirac cone unless some kind of intercalation (by Au atoms for example) decouples the layer into quasi free-standing graphene[113]. As it will be discussed in chapter 5, the similarities between the buffer layer on Ru and the one on SiC could extend to their electronic properties and the localization of the electrons.

3.1.1 LEED pattern and STM measurement

As mentioned in the previous chapter, Van Bommel first observed the $6\sqrt{3}$x $6\sqrt{3}$R30°(SiC) reconstruction[26] (later referred to as $6\sqrt{3}$) but was not aware of the existence of a graphitic "buffer layer". In the 1990s, STM experiments on UHV annealed cubic β SiC(111) surfaces[114][115] (which is equivalent to Si-face of 4H and 6H SiC) as well as on 6H Si-face[53] revealed a 6x6 periodicity superimposed with the 1x1 graphene lattice, while LEED consistently displayed $6\sqrt{3}$ as seen on Fig. 1.6. The authors proposed a model of an incommensurate monolayer graphite (the name graphene was only proposed a few years later) laying on top of bulk SiC to explain the discrepancy. In that model the true periodicity of

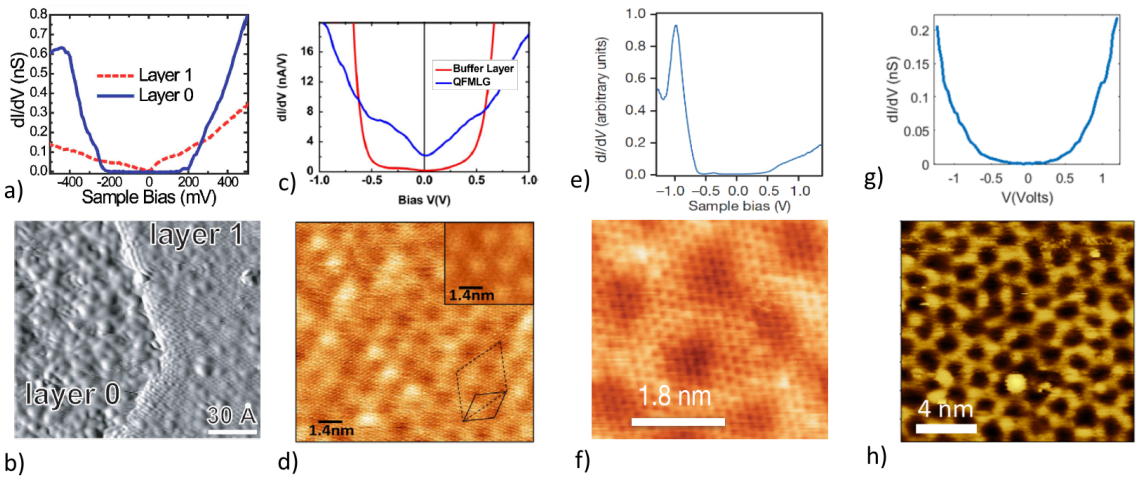

Figure 3.2: STS and STM images taken on the buffer layer. a) and b) are measured on a UHV sample[116], STM tunneling voltage V_t=0.6V and current I_t=100pA , c) and d) are also a UHV sample measured at room temperature[117], V_t=1.7V and I_t=300pA, e) and f) are mearured on a sample grown by the CCS method[77], V_t and I_t not indicated, and g) and h) are taken on one of our CCS grown samples with the help of P. First and H.-J. Wu, V_t=1.0V and current I_t=100pA.

$6\sqrt{3}$ is created by each carbon atom that aligns on top of a silicon atom (points A,B,C,D,E and F in Fig. 3.1). The 6x6 unit cell is defined by three of these points (such as B, C and D) plus a carbon hexagon surrounded by 6 silicon atoms (point G).

Still, the authors considered that first carbon layer to be a free standing graphene sheet. A subsequent STM study[118] showing large area 6x6 periodicity, coupled with X-ray photoemission spectroscopy (XPS) adopted the concept of a carbon nanomesh with a mixture of carbon atoms that covalently bonds to the substrate (S_2 peak in XPS data) and some that lie freely above the surface (S_1 peak). It wasn't until 2007 that numerical calculations[119][64] made on unit cells smaller than $6\sqrt{3}$ predicted the presence of an insulating "buffer layer" which interaction with the substrate would dramatically change its π-bands compare to pristine graphene. STS revealed the presence of a gap in the density of states around the E_F of about 400meV[116]. Since then however, STS measurements consistently observed a gap around 1 eV[117][77][120][121]. Fig. 3.2 compare the STS and STM images from three different papers, with a), b),c) and d) measured on UHV grown samples and e) and f) grown via the CCS method with a recipe optimized for the growth of sidewall graphene nanoribbons. The long range ordered 6x6 as well as the graphene lattice

is visible on the STM image d) confirming the continuity of the graphene layer, and image f) shows a higher definition of the unit cell. g) and h) are measurements taken on one of our own CCS grown samples at room temperature, confirming the consistency of STS and STM with previous studies.

3.1.2 Intercalation of the buffer layer

One of the most important discovery made on the buffer layer is that it can be converted into a quasi free-standing graphene (QFSG) layer by intercalating chemical species at the SiC interface. This confirmation that the buffer layer is structurally graphene was initially given by Riedl *et al.*[122]. They showed that the buffer layer converts to a slightly p-doped QFSG layer upon annealing between 600° and 1000° in molecular hydrogen at atmospheric pressures. Later on, the structural integrity of the QFSG thereby produced was confirmed by STM measurements[117]. X-ray reflectivity (XRR) indicates that it is lifted upwards by 2.1 Å compared to the buffer layer and is indistinguishable from other graphene layers on top of it, if there are any[123]. Transport measurements performed on QFSG indicate that it is of superior quality than a regular Si-face monolayer (that is, a monolayer graphene on top of the buffer layer) with mobilities reaching 3100 $cm^2V^{-1}s^{-1}$ at room temperature and a reduced full width at half maximum of 24 cm^{-1} for the Raman 2D peak[124]. this 2D peak is shift to lower values indicating the presence of tensile strain. Upon intercalation, it has been shown that the SiC surface is saturated with hydrogen bonds, and that the process can also lead to local defect in the form of sp^3 C-H bonds[125].

For reference, here are the other species known to intercalate under the buffer layer: Al[126], Au[127], Bi[128], Ca[129], Cu[130], F[131], Fe[132], Ge[133], H2O[134], Li[135], Mn[136], Na[137], O_2[138], Pb[139], Pt[140], Si[141], Sn[142], Yb[143]. The properties of the obtained graphene layer changes with the intercalated atoms. For instance, Li intercalation occurs at room temperature and forms a n-doped graphene layer, and Pb induces a new Moiré pattern.

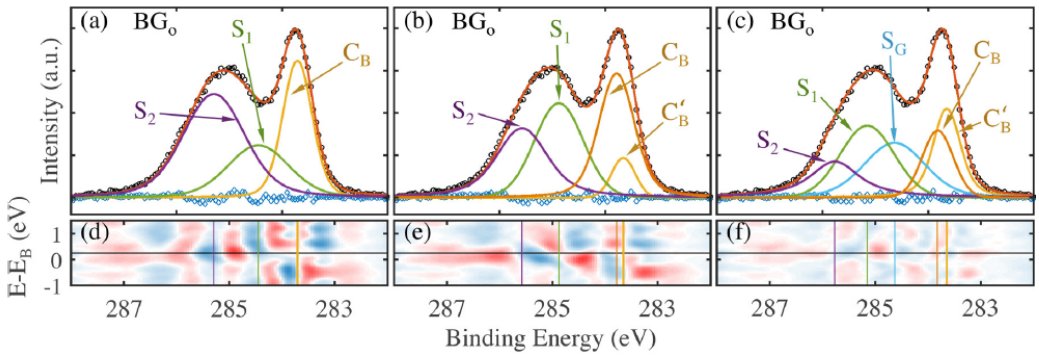

Figure 3.3: The C1s spectral decomposition for a buffer layer (BG_0) film. The fits are at a photon energy of E-$E_{photons}$ = 0.25 eV. The residual maps [(d), (e), (f), (i), and (j)] for each fit are shown as a function of E-$E_{photons}$ and binding energy. Vertical lines in the maps mark the best-fit binding energy peak positions of each component. (a) C1s spectra using a 3-component fit with two buffer components, S_1 and S_{B2}, plus a bulk SiC component C_B. (b) A 4-component fit similar to (a) but with an additional component labeled C'$_B$. (c) A 5-component fit similar to (b) but with the additional component S_G. From reference [67]

3.1.3 XPS analysis

We have already mentioned that the XPS spectrum of the buffer layer has multiple components. Ascribing the XPS components to carbon species has been subject to controversies in the past, but a more recent and careful analysis identifies three distinct components in the buffer layer structure[67] (see figure 3.3). It was shown that using only the two component S_1 and S_2 did not give the best fit of the experimental data. In addition, with the knowledge of a quasi $6\times6_{SiC}$ reconstructed interface under the buffer layer[66], it seems that considering a single component for the contribution from SiC to the C1s spectrum is only an approximation. The fit residuals are minimized (Fig. 3.3c and f) by adding one component to the SiC contribution and one to the buffer layer. The interpretation and justification of the three buffer layer XPS components is facilitated by a combination of X-ray reflectivity (XRR) and X-ray standing waves (XSW) measurements which also identifies three different atomic species in the buffer layer, each residing at an different average distance from the substrate. In light of this, S_G was confidently associated with carbon atoms residing far away from the substrate, and S_1 with atoms the closest to the substrate and bonding to Si atoms. Finally, this model attributes S_2 to intermediate atoms between S_1 and S_G.

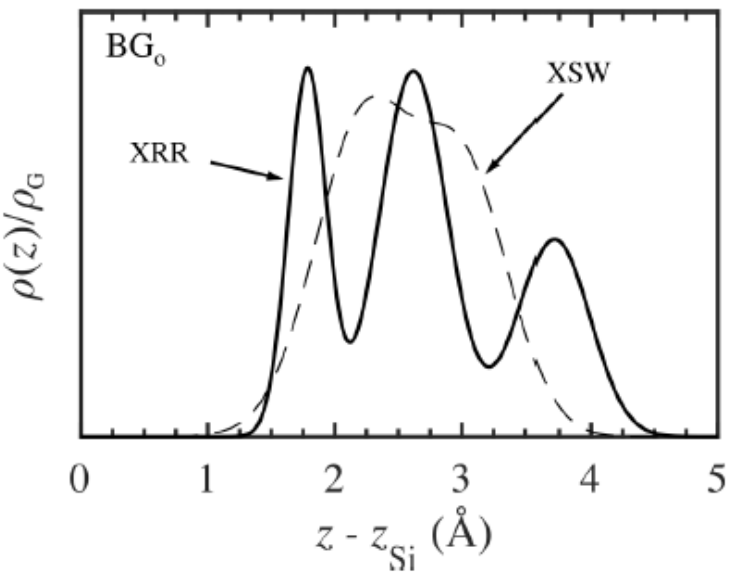

Figure 3.4: A comparison of the buffer layer vertical density distribution, ρ(z), derived from XSW (dashed line) and XRR (solid line). The density is normalized to the density of a graphene layer. Reproduced from [67].

3.1.4 Measurement of the buffer layer corrugation

The XRR and XSW techniques mentioned above give a quantitative measurement of the amplitude of corrugation of the buffer layer. The average minimum distance from the substrate is found to be around 1.9 Å and the width of vertical distribution is 2.4 Å[67]. This is illustrated in Fig. 3.4.

Other techniques have also been used to estimate this corrugation amplitude, such as STM[118] where they find a height difference up to 3.5 Å between bottom and top of the corrugation. Smaller differences were observed for films annealed for a shorter time, indicating a certain dependence of the morphology on the recipe used, at least for sample grown in UHV. The pattern in STM measurement was however alternatively considered to be due to electronic effects[144], indicating the difficulty to make strong conclusions based on STM measurements only. TEM measurements (Fig. 3.5c and d) found an average smallest distance to the substrate of 1.9 Å and an amplitude of 0.9 Å only[68]. This discrepancy with the XRR results may be due to a lower resolution of TEM compared to X-rays, or due to the sample preparation for TEM measurements. As such, the amplitude given by XRR

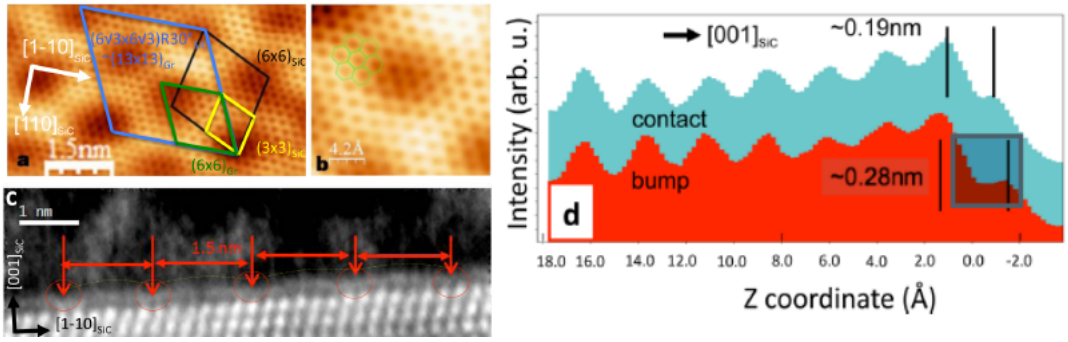

Figure 3.5: Top and side views of the buffer layer structure. a) STM image (I = 0.25 nA, V = 1.5 V) of the buffer layer, showing the quasi-6×6$_{SiC}$ periodicity (black diamond). b) Close-up on the image shows the graphene honeycomb structure without hexagonpentagonheptagon defects. c) TEM image of a cut through the buffer layer grapheneSiC interface. The dotted line is a guide to the eye above the buffer layer to show the bonding points of the buffer layer to the substrate. The overall periodicity between bonding points is 1.5 nm, compatible with a 6×6$_{SiC}$ period. (d) Vertical profiles of the interface in c have been obtained by averaging the TEM data over several regions where the buffer is attached to the substrate (contact) and where it is decoupled (bump). The red arrows in panel c indicate where the contact profiles were measured. Reproduced from [68]

will be used in our analysis later on.

3.1.5 Comment on the nature of the interactions

The distance between the substrate and the closest carbon atoms is about 1.9 Å which is essentially the same as a Si-C bond in SiC. The S1 peak in XPS is also close to the binding energy of Si-C in SiC once the overall shift of the σ-bonds of 1 eV downwards is taken into account[63] (see section 3.2 below). This has lead some confusion in the literature about whether or not there is a sp^3 character in the bonds between those carbon atoms and the substrate. Some references avoid the nomenclature all together and simply talk about covalent bonding[63, 145] while others consider the mixture of sp^2 and sp^3 as the origin of the buffer layer band structure[66, 67].

A criteria on the character of carbon bond was proposed as a function of the angle between the bonds of a carbon atoms[146]. Fig. 3.6 shows the evolution of the angles between a π-orbital and the other bonds as a function of the hybridization character which can be completely sp^2 (on the left side of graph), completely sp^3 (on the right side) or a mixture of both. Note that the bond takes a more sp^3 character only past an angle of 105°.

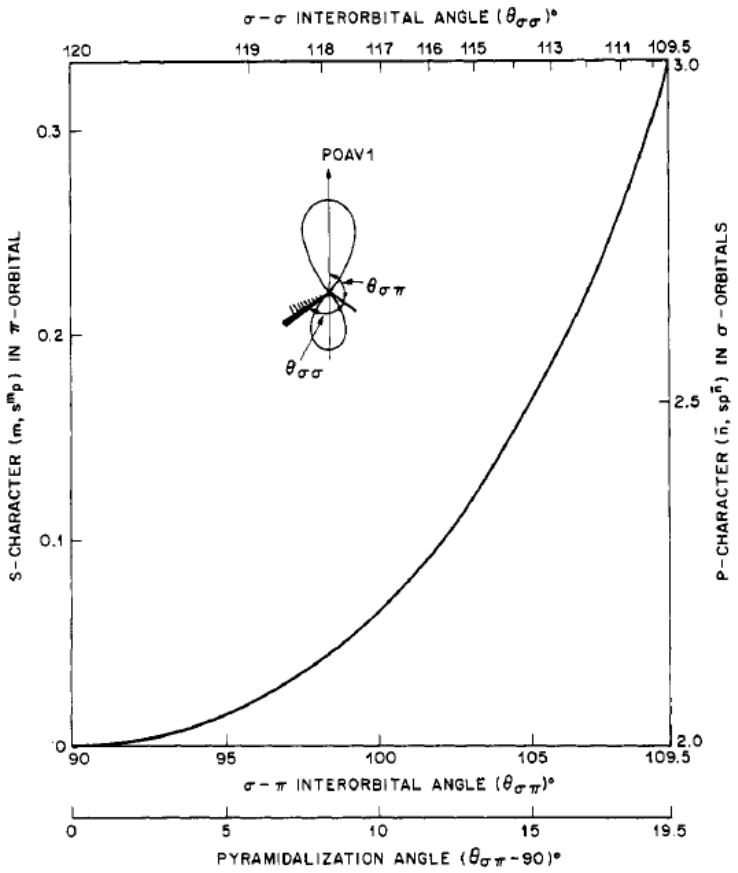

Figure 3.6: Relationship between the σ-σ and σ-π interorbital angles and the hybridization at a carbon atom between the extremes of sp^2 (planar geometry) and sp^3 hybridization (tetrahedral geometry). Reproduced from [146]

While the measure of the bond angles between carbon atoms in the buffer layer has not be quantified, atomic resolution STM and TEM (Fig. 3.5) qualitatively show a relatively smooth corrugation. There is no doubt that a careful study of the exact structure of the buffer layer and its bond angles would bring further insight on the matter. In addition, the ease of intercalation of species decoupling the buffer layer (at room temperature in some cases) from the substrate is intriguing and seems also to argue in favor of weaker interaction than pure covalent bonding. The relevance of this question will come to light in chapter 5 where the transport properties of the buffer layer are interpreted.

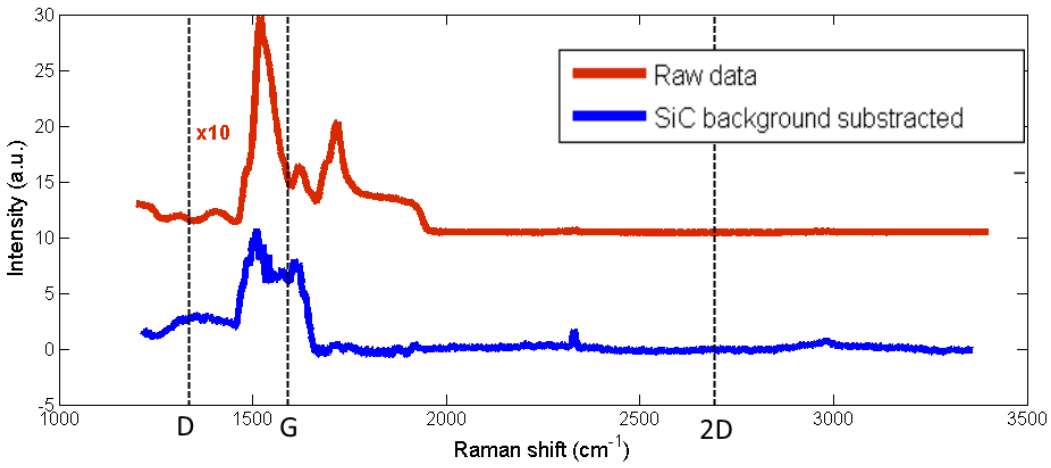

Figure 3.7: Example of a Raman spectrum of a buffer layer sample grown via CCS.

3.1.6 Raman spectroscopy

Epitaxial graphene is well characterized by Raman spectroscopy, and the buffer layer has its own Raman signature, which remains relatively unexplained. Fig. 3.7 shows a typical Raman spectrum of the buffer layer. The 2D peak characteristic of graphene is absent, a broad peak is found around 1355 cm^{-1} which corresponds to the D peak position, and two broad peaks are resolved around 1480 cm^{-1} and 1580 cm^{-1} the latter being the position of the G peak in graphene. A non zero intensity is present between those two peaks. Fromm *et al.*[147] attempted to identify the Raman spectrum of the buffer layer and associated it with a vibrational density of states. Their model qualitatively agree with some of the observed features but does not reproduce the full spectrum.

While the Raman spectrum of the buffer layer is yet to be explained quantitatively, it is a quick and powerful characterization of the film. Some discrepancy between experiments can be found with sometimes the observation of a higher D peak, which could be ascribed to more defective films[148][149].

The Raman spectra obtained for the samples measured in the next chapter qualitatively agree with those published in references [147] and [67], the latter being the reference from which we take the buffer layer corrugation amplitude.

3.2 Band structure

3.2.1 ARPES measurements and calculations

ARPES measurement were done on UHV grown sample revealing certain aspects of the band structure of the buffer layer[63]. Fig. 3.8 shows the obtained band dispersion along the Γ-K and Γ-M directions of the brillouin zone. Graphene like σ bands are observed between 5.1 and 22.7 eV which is the same width (17.6 eV) as for graphene. This indicates that the nature of C-C in plane bonds is very similar to that of graphene and that the average C-C distance is the same. This conclusion is corroborated by the similar size of Brillouin zone in LEED pattern of monolayer graphene and buffer layer[63]. However, compared to pristine graphene, the whole bands are shifted 1 eV down in energy. Si-face monolayer bands are shifted about 0.4 eV down due to spontaneous n type doping attributed to the substrate charge transfer and a similar explanation for the buffer layer is plausible but other effects are also to be taken into account. Indeed, the π bands are dramatically changed compared to graphene and up to this day, the features that "replace" the graphene bands are yet to be explained fully. The shape of the intensity centered around Γ suggest a dispersive π band but shifted by 3.2 eV down with respect to graphene. The brightest bands cross each other around 3.2 eV below the K point of graphite, and their highest energy can be seen around 2.3 eV. Emtsev *et al.*[63] compared this shift in energy to a mechanism similar to graphene grown via chemical vapor deposition (CVD) on nickel (111) surfaces where a lowering of the π bands was attributed to partial hybridization with the states of the substrate[150].

In addition to the shift, there are multiple reflection planes between Γ and K. This has been attributed to band folding due to the additional periodicities in the buffer layer[63]. Above 2.3 eV, Emtsev *et al.*[63] concluded that the spectral intensity is due to two non dispersive surface states g_1 and g_2 situated at 0.5 and 1.6 eV below E_F. However, more recent ARPES measurements done on samples grown by the CCS method, with a much higher resolution in energy above 3 eV and data taken in all momentum directions revealed that those two bands are actually dispersing states[65], with no visible intensity above 0.5 eV, as shown in Fig 3.9c.

While density functional theory (DFT) calculations done on a commensurate graphene

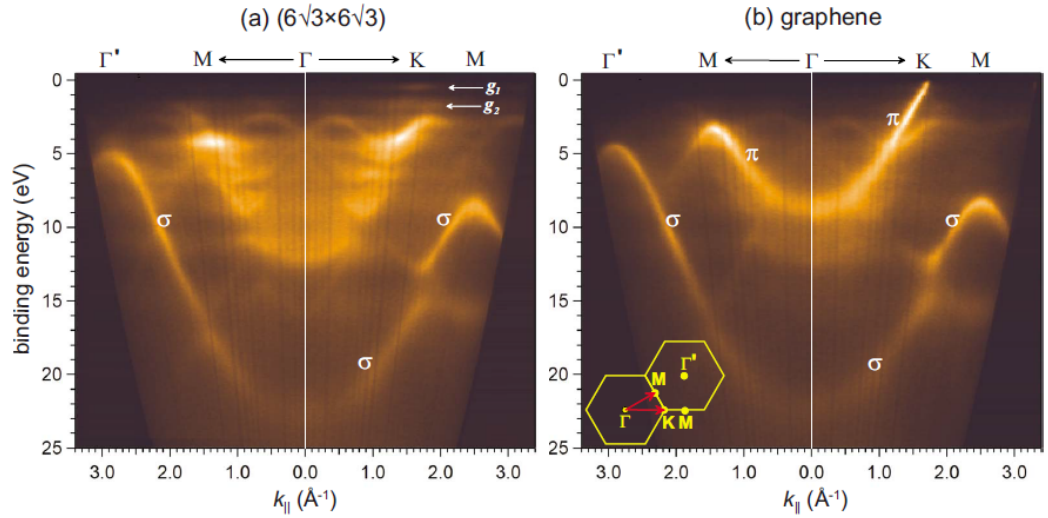

Figure 3.8: Photoemission intensity map vs binding energy and parallel electron momentum of UHV grown a) buffer layer and b) monolayer graphene on top of the buffer layer. Reproduced from [63].

layer with a $6\sqrt{3}$ unit cell on top of a truncated bulk SiC failed to predict this band gap[145], it presents some interesting resemblances in the band structure compared to the ARPES data as highlighted in Fig. 3.9. The calculation (displayed in a) yields of lots of bands that are not presents in the experiment, but a lot of the features visible in the ARPES find a close match in the simulated band structure for energies below -3 eV. Note that the bands crossing around 3 eV below the K point of graphene are already predicted in the earlier calculation on a $\sqrt{3}$x$\sqrt{3}$R30°[64]. Panel c) of Fig. 3.9 is reproduced from Nevius *et al.*[65] where the authors compare the low energy ARPES spectrum (above -3 eV) to the DFT results and argue that despite the lack of band gap, the produced bands present some similarities with their experimental data. In addition to that, the calculations in [145] yield a 6x6 quasi-periodicity in simulated STM images, in agreement with the numerous experiments. Yet, the picture remains incomplete and more study needs to be done to unveil the origin of the band structure of the buffer layer. Recent surface X-ray diffraction experiment (XRD) indicates an incommensuration between the buffer layer and SiC[66]. The incommensuration between the buffer layer and the bulk SiC creates a mutual structural modulation between the graphene lattice and SiC. The periodicity of this modulation was shown to be $\lambda = 6(1+\delta)a_{SiC}$ where $\delta = 0.037$. It was also shown by tight-binding calculations that the

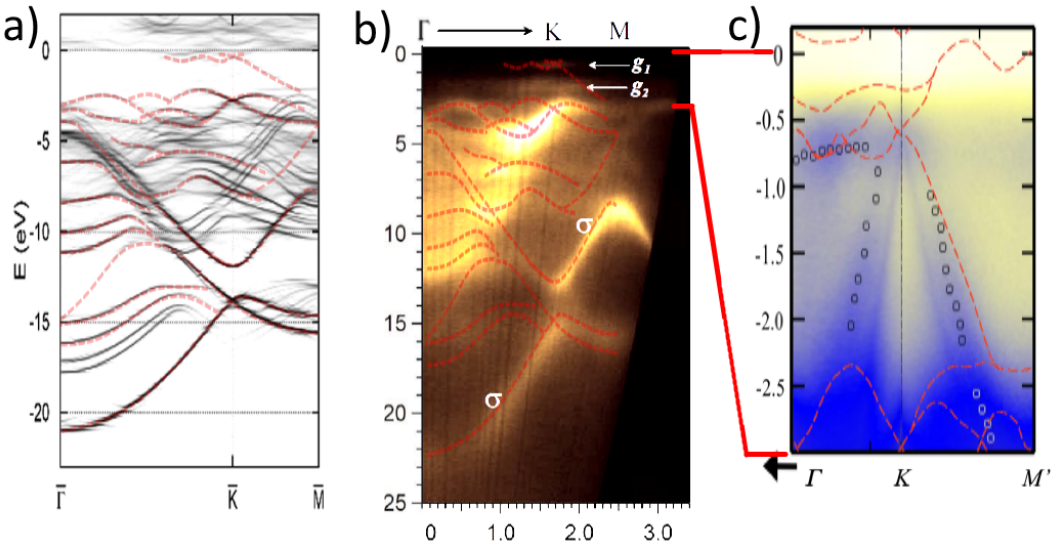

Figure 3.9: Comparison of ARPES data with DFT calculated band structure. a) DFT calculated bands reproduced from [145]. Red dashes are corresponding to the selected DFT bands that found a close match in ARPES data. b) ARPES data with overlaid selected bands from DFT calculation. Reproduced from [63] c) Low energy ARPES data with overlaid bands from DFT calculation. Reproduced from [65]

commensurate tight-binding model does not yield a semiconducting buffer layer while the incommensurate one results in a band gap of 0.8 eV. In light of this, future theoretical modeling aiming to accurately describe the buffer layer band structure should consider that incommensuration in the calculation.

3.2.2 Conduction band

Since ARPES is only sensitive to occupied states, the conduction band cannot be probed with this technique. It is known from STS that there are electronic states available around 0.5 eV above the Fermi level, but their dispersion is not determined. Angle-resolved inverse photoemission spectroscopy (ARIPES) follows a reversed principle to ARPES by initially populating the unoccupied states by a beam of incident electrons. A photon flux is generated by the radiative transitions of the incoming electrons into unoccupied states in the sample. This flux is measured in order to reconstitute the band structure. This technique was used on the $6\sqrt{3}$ phase of SiC (and therefore the buffer layer) but it did not resolve graphite related states below 2 eV[82]. As UHV grown samples have proven not to give the best resolution of the band structure of the buffer layer, this does not give definitive conclusions on

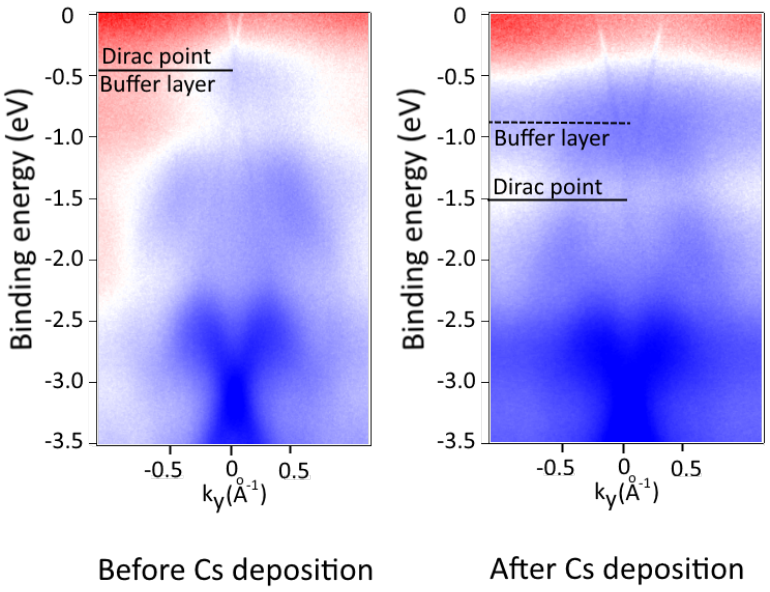

Figure 3.10: Comparison of ARPES data before and after Cs depostition. The Dirac point from the small coverage of monolayer graphene is shifted 1 eV down while the top of the buffer layer band is only shifted about 0.3 eV.

the conduction band of the buffer layer. In an attempt to study the conduction band of the buffer layer, we performed ARPES measurement at the CASSSIOPEE beam line of the Synchrotron SOLEIL in collaboration with Dr. Antonio Tejeda, Dr. Amina Taleb-Ibrahimi and Dr. Maya N. Nair. Cesium (Cs) was used to electron doped the buffer layer, as Cs deposition on epitaxial graphene is known to shift the Fermi level up by 1 eV[151]. The deposition is done in situ the ARPES system and the sample is measured before and after deposition. The sample contains some traces of monolayer graphene on the step edges giving rise to a faint Dirac cone in the ARPES data (Fig. 3.10). It serves as a reference to see the doping level in the sample. As it can be seen in the data presented in Fig. 3.10, the Dirac point of graphene is shifted about 1 eV down but the top of the valence band of the buffer layer is only shifted about 0.3 eV down and no conduction band is observed. While we only show the ARPES data around the K point, no conduction states were revealed over the whole Brillouin zone. It is not known at this time why the electrons from the Cs did not populated higher states in the buffer layer, but one would expect that such a high level of doping to start populating the bottom of the conduction band if there was a symmetry between holes

and electrons as predicted by the tight-binding model of reference [66]. This arises questions concerning the presence of a dispersive conduction band or not above the Fermi level.

We have now described what is known of the atomic and electronic structure of the buffer layer. The possibility to convert it into a good quality QFSG layer indicates it is a continuous graphene layer. The periodic interaction with the underlying SiC, while not fully determined in nature, induces a large hexagonal corrugation of 2.4 Å. Electronically, the density of state vanishes around the Fermi level in a 1 eV gap. While the valence band has been resolved as a wide but dispersive band, the conduction band remains unknown. Electrons above the Fermi level should however be the one participating in the conduction, if there is any, and transport studies are needed to determine the charge carrier dynamics of the buffer layer.

CHAPTER IV

TRANSPORT MEASUREMENTS ON THE BUFFER LAYER

The most recent studies of the buffer layer have been motivated by the idea that the buffer layer is an ordered semiconducting form of graphene and could potentially be utilized for conventional field effect transistors[65, 66, 152, 67]. Despite this claim, the buffer layer carrier mobility or its current switching capability have not been investigated. In fact, a study of the electronic transport or device fabrication is completely missing in the literature except for some preliminary experimental data presented in the PhD dissertation of Dr. James Palmer[153]. His work focused mainly on very short channel buffer layer devices and concluded that most of their resistance was situated in the Schottky barrier between the graphene leads and the buffer layer. While those short channel devices did not have any field effect response from a top gate, it was demonstrated that some devices with longer channel displayed an on/off current ratio $\frac{I_{on}}{I_{off}} = 10^3$. However, the minimum resistance of those gatable devices was very large: around 200 $M\Omega$.

In this chapter, I demonstrate that the electronic transport in the buffer layer is dominated by Mott variable range hopping conduction and that it displays more an insulating behavior than a semiconducting behavior. In the first section, I describe some device fabrication considerations specific to the buffer layer. In the second section, I examine the influence of the contacts and establish that the main contribution of the resistance comes from the buffer layer channel itself when the samples have been desorbed from air contaminants. Section 3 addresses the modulation of the conductance of buffer layer devices through the adsorption of different gases and in response to a gate voltage. I report about some experimental attempts to measure the influence of a strong perpendicular magnetic field in the buffer layer in section 4. Finally, section 5 presents the results of two-point resistance measurements as a function of temperature and electric bias. The analysis shows how it fit perfectly the model of Mott variable range hopping in two dimensions.

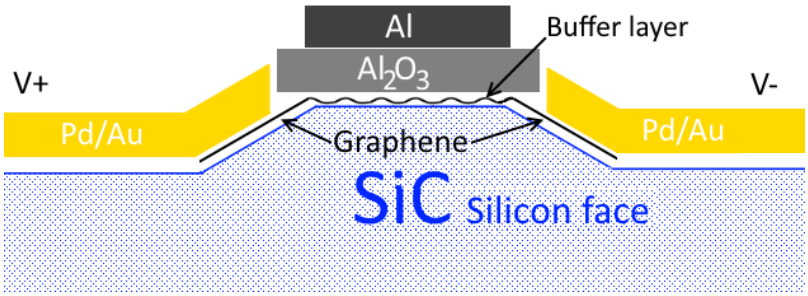

Figure 4.1: SWGNRs and buffer layer seamlessly connected in a top gated device geometry.

4.1 Device fabrication considerations

The fabrication of buffer layer devices presents some unique challenges that we underline in this section. The preparation of the SiC surface before growth, the growth itself and the importance on the packaging of the devices are all addressed.

4.1.1 SiC surface preparation for buffer layer devices

As described in section 1.3.3, SWGNRs form on the sidewall of natural SiC steps and would short a device built on a area that is not free of such steps. On the other hand, those nanoribbons can be grown in a controlled manner and utilized as electrical leads to inject current in the buffer layer, as SWGNR are seamlessly connected to the buffer layer on top of the trenches (see Fig. 1.8 of section 1.3.3). Fig. 4.1 shows a proposed geometry for a top gated buffer layer device, where the channel is made of the buffer layer grown on top of an etched trench. The seamlessly connected SWGNRs act as source and drain for the device. Alternatively, devices can be built with Pd/Au contacts directly deposited on a SiC step free buffer layer area.

The issue is that step flow and step bunching naturally occur on the Si-face of SiC during graphene and buffer layer growth[154]. In order to gain a control of the step flow, amorphous carbon corrals have been proposed as a mean to pin the SiC surface during growth, forcing the steps to bunch at those carbon barriers and creating large flat terraces during graphene or buffer layer growth[155]. More generally, promoting a large step bunching during or before graphene growth allows to produce large step free buffer layer areas. We adopted a method along those lines, referred to as "face-to-face" annealing[156]. It consists in stacking

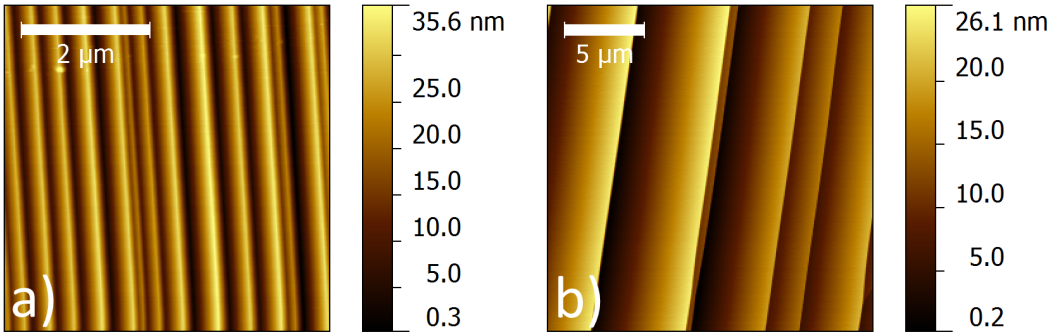

Figure 4.2: NC-AFM topography images of SiC surface after face-to-face annealing for a) 4° off-axis 4H SiC and b) on-axis 4H SiC.

two (or more) pieces of SiC in a closed (no leak hole) graphite crucible, with their (0001) surfaces facing each other. Due to this confinement and the exchange of Si atoms from one surface to the other, graphene growth is inhibited up to at least 1700°C in an argon background pressure above 1 atm. Step flow and step bunching on the two (0001) surfaces are then largely promoted: Fig. 4.2 shows the result of such an annealing for two hours for (a) a 4° off-axis SiC wafer and (b) an on-axis wafer. The smaller the miscut angle is, the larger the terraces can be obtained.

The recipe systematically used to produce large terraces with a step height above 10 nm is the following: up to six samples at a time are placed in the graphite crucible, Si-face placed face-to-face two by two. The chamber is pumped down to a pressure below $5{\times}10^{-6}$ mbar and the crucible is heated to 800°C for 30 minutes. Just before the end of this heating step, the vacuum pump is stopped and 4 sccm of argon is flown in the chamber at about 16 PSI. The temperature is then increased at a rate of 10°C/s up to 1700°C where it stays for two hours before cooling down to room temperature, still under Ar flow. If the same process is performed at a lower temperature, the step height is significantly reduced. For instance, annealing an on-axis SiC sample at 1550°C creates steps around 5 nm high only, and the surface is not stable during the subsequent growth of the buffer layer. Fig. 4.3 a) and b) shows the meandering of steps due to the growth process, and "canyons" forming inside the terraces for steps averaging around 5 nm high. The surface structure has a much higher probability to be preserved when the steps are higher than 10 nm, as shown in Fig.

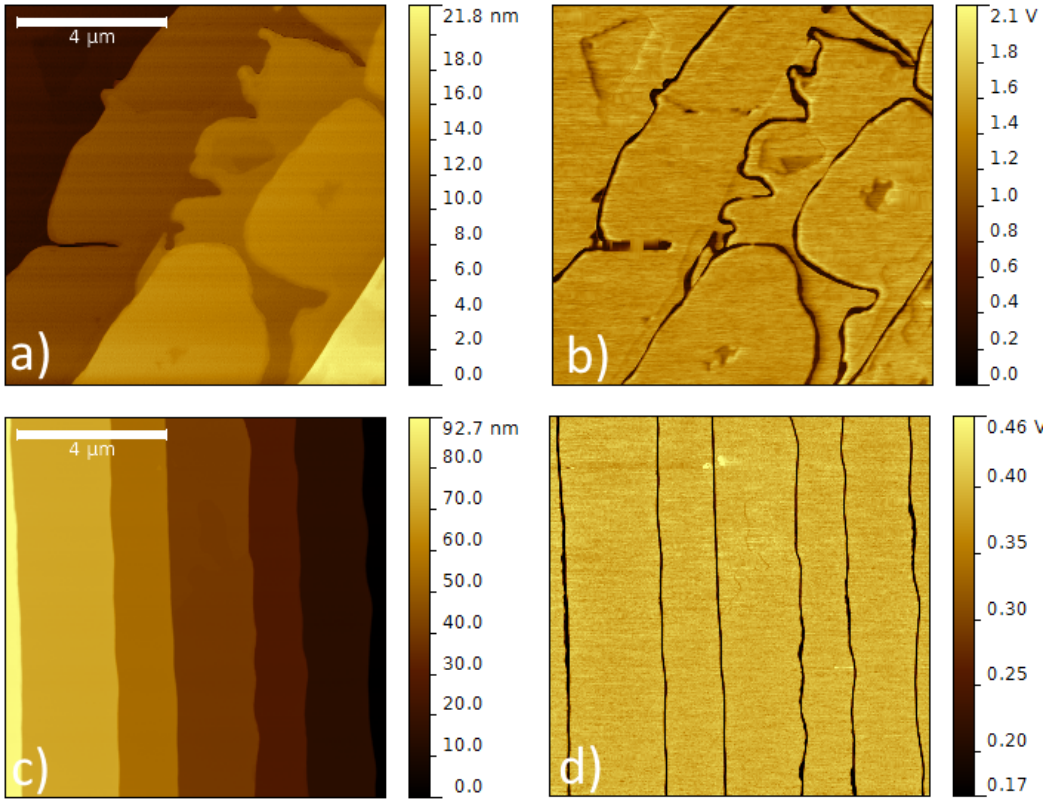

Figure 4.3: C-AFM topography images of SiC surface after growth of the buffer layer succeeding face-to-face annealing at a) 1550°C (with its corresponding LFM image in b) and c) 1700°C (LFM in d). Dark contrast in LFM corresponds to graphene ribbons.

4.3 c) and d).

In the case of SWGNR-contacted buffer layer devices, nanostructures are patterned and etched with RIE on large SiC terraces before growth. Hall bar geometry and two-terminal devices can be made, as shown by AFM and LFM images in Fig. 4.4. A subsequent patterning and a RIE etching with O_2 define the device geometry by removing the extra buffer layer and graphene shorts between terminals. Pd/Au is finally deposited on the SWGNRs or directly on the buffer layer (Fig. 4.5) for wire-bonding.

4.1.2 Growth parameters

More than 200 buffer layer samples were grown throughout this work. As mentioned in section 2.1.1, the CCS method was use to produce the graphene. The crucible used for the growth of the buffer layer has an inner diameter of 4.5 mm, a depth of 8 mm (once the

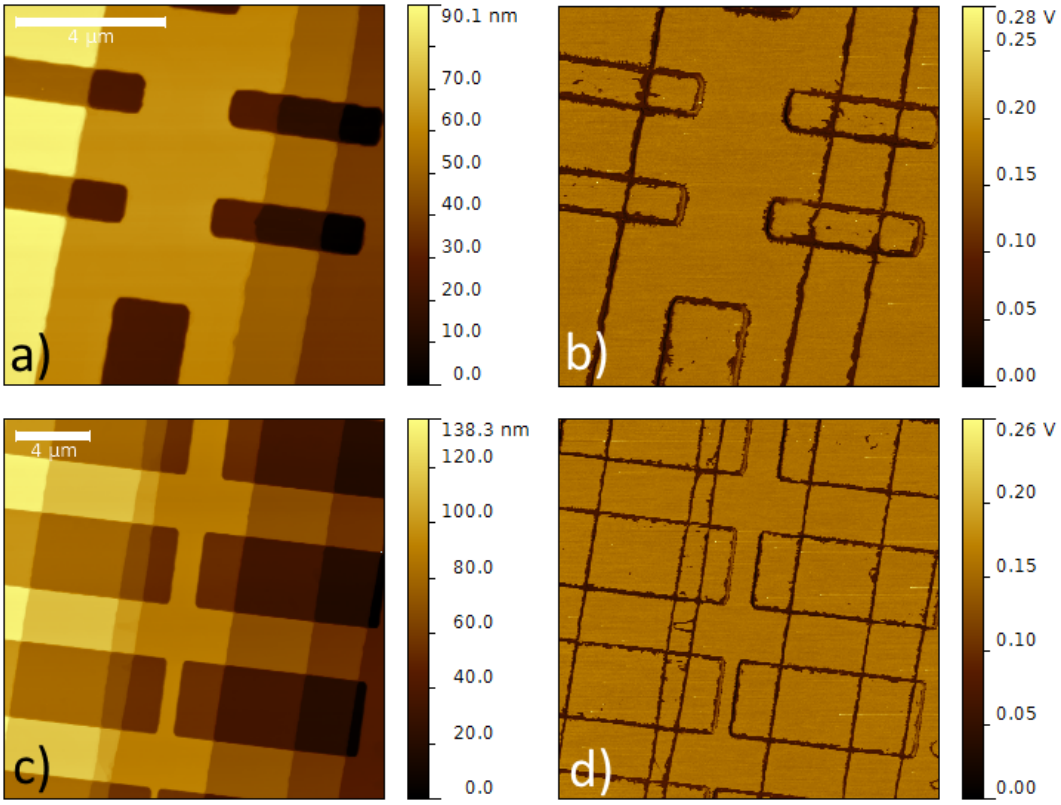

Figure 4.4: Examples of nanostructures for graphene contacted buffer layer devices. a) AFM image and b) corresponding LFM of a Hall bar device after graphene growth. c) AFM image and d) corresponding LFM of a series of two-terminal graphene contacted devices. Dark contrast in LFM is low friction graphene ribbons.

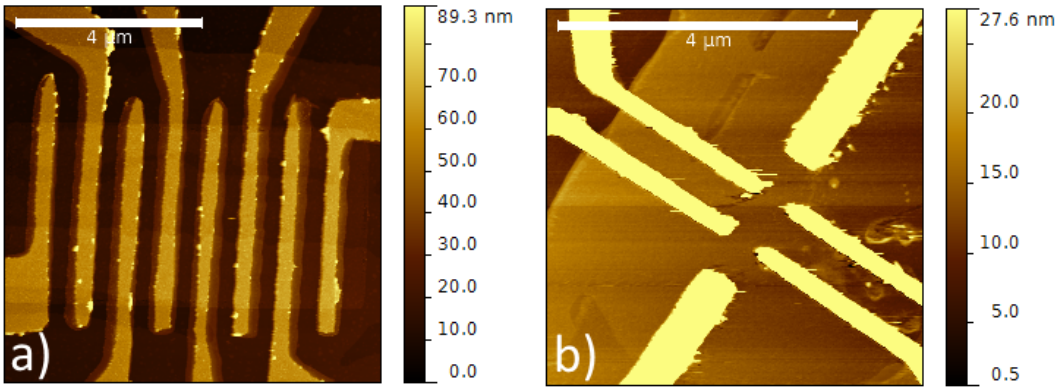

Figure 4.5: NC-AFM topography images Pd/Au contacts directly deposited on the buffer layer. a) In line contacts b) Hall bar geometry.

cap is on) and leak hole of 0.5 mm in diameter and 6.6 mm long. Recipes varies slightly depending on the desired result. The chamber is pumped down to 1×10^{-6} mbar before baking the sample for 20 min at 800°C to desorb air impurities. A step at 1250°C for another 20 min is systematically used to decompose the oxide layer that forms naturally on the SiC surface exposed to air. The buffer layer eventually grows at 1440°C. Annealing SiC for 20 min at this temperature will produce a surface almost free of graphene growth on the step edges, ideal for contacting the buffer layer with metal contacts. Annealing for an extra 10 min (30 min total) results in higher amount of graphene growth, as shown by LFM in Fig. 4.4 b and d. The consistency of the buffer layer growth is also checked with Raman spectroscopy.

4.1.3 Sample packaging and definition of a "clean" device

As it will be discussed in details in section 4.3.1, the resistance of buffer layer devices is strongly dependent on the presence of adsorbates. Consequently, a thick protective layer of Al_2O_3 is deposited on the devices in order to study their intrinsic behavior. The samples are left bare when their purpose is to study the effect of the environment, as in section 4.3.1.

Once the Pd/Au contacts are deposited on a sample, it is annealed at 500°C for 20 min in vacuum, at a base pressure of 2×10^{-7} mbar. This process desorbs most of the loosely bound contaminants, while leaving the metal contacts intact, as confirmed by AFM characterization. The fabrication process leaves resist residues in the area of the devices, and their composition is likely to change during annealing (such as pyrolysis). However, as it will be demonstarted shortly, the effect of annealing on the conduction is reversible upon re-exposure to air and it does not seem that the decomposition of the resist residues affects the transport properties of the devices. The sample is then cooled down and 30 nm of Al_2O_3 is deposited by thermal evaporation. The sample is transferred to an ALD chamber immediately (the sample is exposed to air for about 20 seconds during the transfer) and another 50 nm of Al_2O_3 is deposited. After such a procedure, the samples behave the same electrically as when they are measured after annealing in a vacuum probe station without

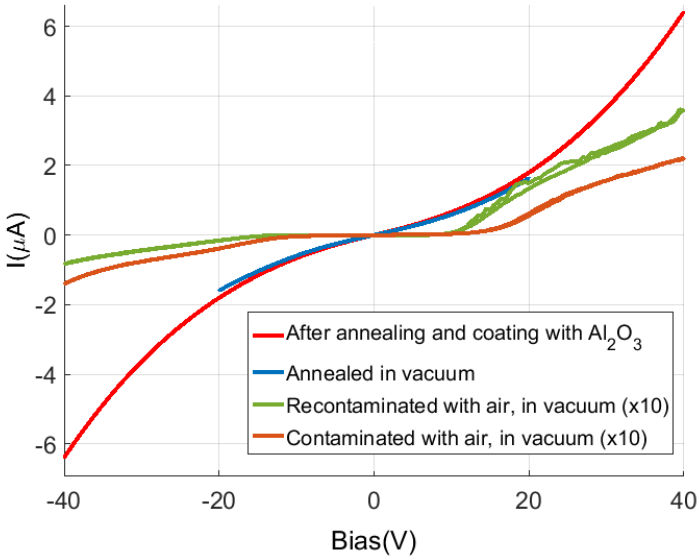

Figure 4.6: IV curves of a graphene contacted two-terminal buffer layer device in different conditions. Coating the device with Al_2O_3 (red curve) has a similar effect as measuring the device annealed in a vacuum probe station (blue curve). Data for the contaminated device was multiplied by a factor 10 for visibility (green and brown curves).

any protective layer. A sample that is measured in either of those conditions will be referred to as a "clean" sample.

Fig. 4.6 represents the current-voltage (IV) curve of a graphene contacted two-terminal device measured in air, in vacuum after a 300°C annealing, and with a protective layer of Al_2O_3 deposited after annealing at 500°C. There are significant differences between the IV curves before and after cleaning the surface. First, the resistance of the device around zero bias decreases upon annealing by a factor 500. Second, the IV curves of the clean device are symmetric with respect to positive and negative bias voltage, contrary to the devices exposed to air. This leads us to discuss a potential contribution from the contacts in the device resistance.

4.2 Contact vs bulk resistance for clean samples

This section addresses the question of the presence of a Schottky barrier at the junction of graphene or metal and the buffer layer. As mentioned at the beginning of this chapter, the early analyses of the transport in buffer layer devices viewed the Schottky barrier to be

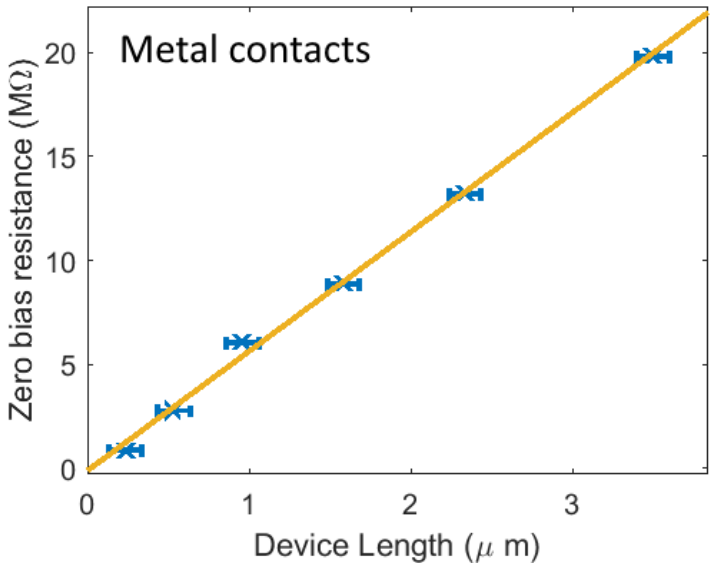

Figure 4.7: Zero bias resistance of a series of Pd/Au contacted clean buffer layer devices plotted versus the length of the devices.

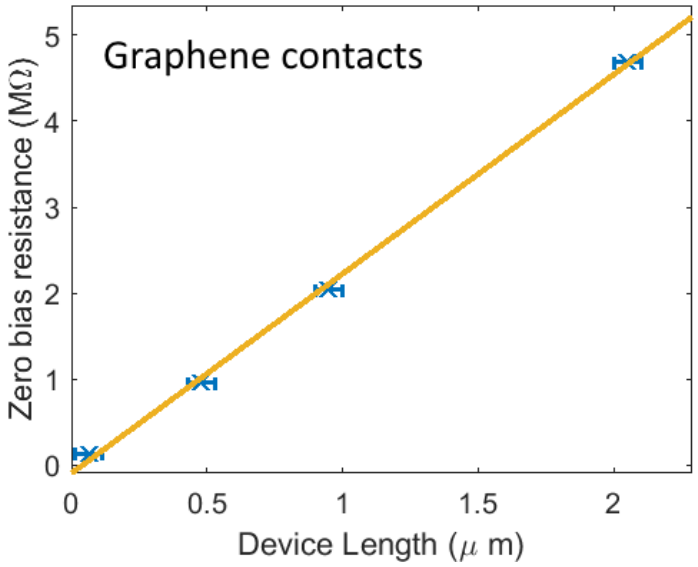

Figure 4.8: Zero bias resistance of a series of graphene contacted clean buffer layer devices plotted versus the length of the devices.

the dominant source of resistance[153]. With the improved fabrication process developed in this work, we are able to produce buffer layer devices with a well defined geometry and dimensions, allowing us to do a more quantitative study. We will present two independent arguments in favor of a channel dominant device resistance when the sample is clean. The first argument is the dependence of the resistance on the channel length, as discussed in this section. The second one is simply that the conduction model that fits the resistance data in section 4.5, i.e. Mott variable range hopping in two dimensions, does not correspond to a contact effect, but can only be interpreted as the resistance of the channel.

A series of devices with varying channel length have been fabricated with Pd/Au contacts as well as with graphene contacts. The two point resistance of each device is measured after annealing in vacuum and plotted versus the channel length in Fig. 4.7 for metal contacts and in Fig. 4.8 for graphene contacts. Both series of devices are about 4 μm wide. The resistance is clearly an increasing function of the channel length, and a rough estimate of the contact resistance can be extracted from the intercept at zero length. Given the error bar In both cases, it is virtually negligible compared to the 10 to 20 MΩ bulk resistivity (extracted from the slope).

So far, the question of contact contribution was only addressed for clean samples, where it was demonstrated that the bulk resistance is dominating. We will now consider how the effect of the adsorption of gases on the buffer layer devices.

4.3 Modulation of the conduction

The conductance of buffer layer devices can be modulated in response to external parameters. In particular, the change in conductance induced by the absorption of gases is investigated. We also show that the current in the buffer layer can be slightly tuned by applying a voltage to a top gate, and how this response is consistent with electron conduction rather than hole.

4.3.1 Effect of the environment

The difference of behavior between air contaminated devices and annealed ones is striking. While the behavior of clean devices will be well understood by the end of this chapter, the

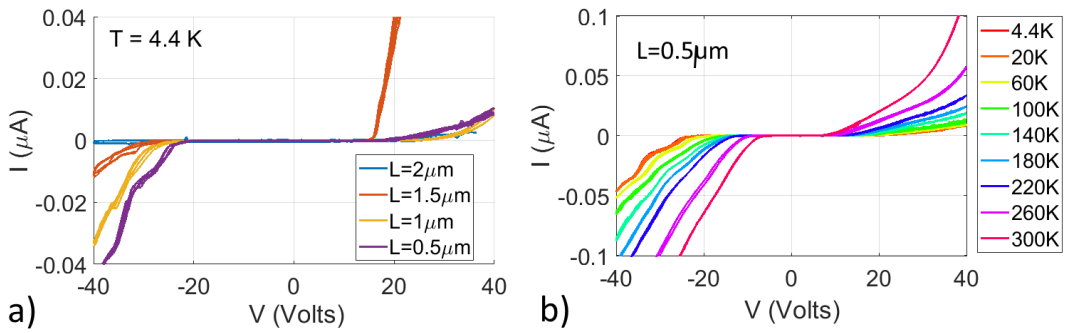

Figure 4.9: a) IV curves of graphene contacted devices exposed to air. Each device length is indicated in the legend, showing that the positive voltage part of the curve does not scale with the length of the device. b) IV curves at different temperatures for one of the devices. The structure in the IVs is more pronounced at low temperature.

conductance of contaminated devices appears to have a more complex origin. It is clear however that contact effects become prominent. Fig. 4.9 shows how the IV curves shape changes with each device and with the positive and negative bias for SWGNR contacted devices when they are contaminated with air. The curves are measured on the same series of devices as in Fig. 4.8. While the current on the negative voltage side increases as the length of the device decreases, the current on the positive voltage side does not follow the same trend This indicates that the channel resistance is not the only limiting effect, and the contacts need to be taken into account as well for uncleaned devices. A closer look at the edge of graphene contacts indicates that it is not a straight line but is rather quite a meandering edge, as shown in the LFM image of Fig. 4.10. The contour of each contact is different and mini graphene ribbons extend into the buffer layer channel. No attempt is made here to interpret how this would affect the IV curves quantitatively, but we simply suggest qualitatively that the structure of the IV curves is related to the specific shape of each contact. If the current injection at the contact/buffer layer junction is limited by a Schottky barrier, then the area (or in this case the line) of contacts determines the resistance: a larger contact would have a lower resistance. In addition, the structure of mini ribbons could have some charging effect as in a quantum dots leading to the structure in the IVs, which would be different for each contacts. Similar effects are observed for metal contacted devices but with less asymmetry between positive and negative bias voltage at

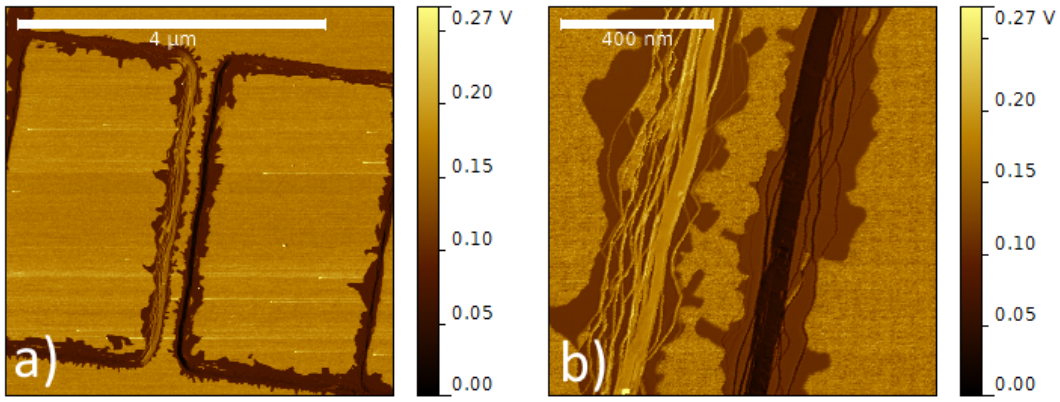

Figure 4.10: LFM images showing that the edges of graphene are meandering and therefore quite different from one another. Image b is a zoom in image a.

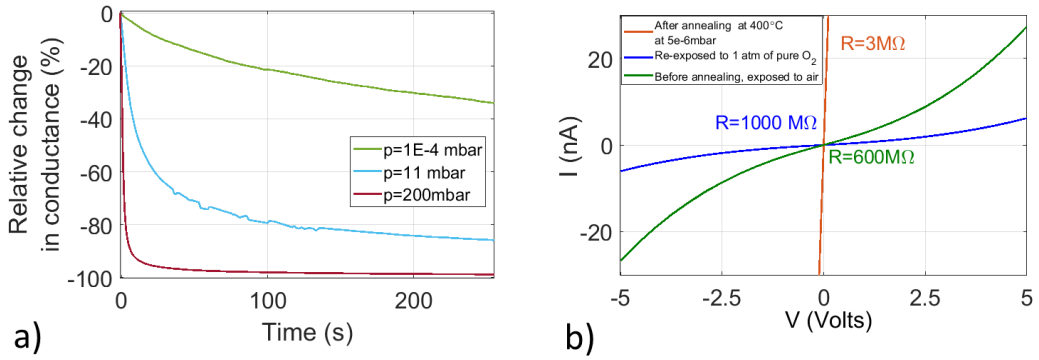

Figure 4.11: Effect of oxygen adsorption on a metal contacted buffer layer device. a) Relative change of conductance after introduction of oxygen at time t=0s. b) IV curves of the devices in different conditions.

room temperature and no pronounced structure, most likely due to the fact that metal contact edges are much straighter that graphene ones. Finally, the injection of charge carriers may be different between metal and graphene contacts due to the fact that in the case of graphene, the contact is between two 2D materials versus 3D to 2D in the case of metal contacts.

A small survey is performed to identified some of the gases having an effect on the buffer layer devices not coated with any protective layer. The devices are first annealed around 300°C for 1 hour in vacuum in order to desorb the loosely bound contaminants. Upon cooling down to room temperature, a constant bias voltage is applied to the two-terminal device and the current is measured with a lock-in over time. Gas is then introduced into the chamber as the current is still measured over time. The introduction of 99.999% pure

nitrogen, helium, or hydrogen at room temperature does not affect the conductance of the devices at pressures up to several hundreds of millibar. However, Fig. 4.11a shows the relative change in conductance over time of a metal contacted buffer layer device when a pressure of 99.999% pure oxygen gas is introduced in the transport measurement chamber (environment controlled probe station). Each curve is measured after annealing the sample at 300°C for 1 hour in vacuum before introduction of oxygen in the chamber. Qualitatively, the rate of the process is an increasing function of the oxygen pressure. It is reasonable to assume that the process follows a simple Langmuir equation $K_a P(1-\theta) = K_d\theta$, where K_a and K_d are the rate of adsorption and desorption, dependent on the temperature and on the pressure P. θ is the coverage of the surface. It is interesting to note that the adsorption of oxygen on buffer layer devices is not a reversible process at room temperature. Indeed, simply evacuating the chamber off its oxygen pressure does not recover the original conductance, but merely stops the process of additional adsorption. This means that the rate of desorption of oxygen on the buffer layer is much slower than the rate of adsorption. As the rate of desorption is a function of the temperature, annealing the sample increases the process of oxygen desorption from the surface.

The conductance eventually saturates to a minimum value, as observed after a long exposure to oxygen. Fig 4.11b shows the IV curves of the same device in air, after annealing in vacuum, and after exposure to 1 atm of oxygen until saturation of the conductance. The resistance is the highest for the sample exposed to 1 atm of pure oxygen. This shows that oxygen is most likely the main component of air influencing the behavior of buffer layer devices exposed to ambient conditions.

It is known that oxygen is an electron acceptor when adsorbed on graphene[9]. As a result, it is not unexpected to observe a decrease in conduction when the buffer layer is exposed to oxygen if electrons are the main charge carriers (see next section on the effect of a top gate). However, if the buffer layer had the properties of a semiconducting form of graphene, one would expect a strong p-doping process to eventually remove all conduction electrons and starts populating the valence band with positive holes. Once the Fermi level is thereby placed near or in the Valence band, the conduction increases again

and occur via holes, but this is not observed in our experiment. there seems to be a lack of symmetry between electrons and holes in the buffer layer. It is possible that the doping induced by oxygen adsorption is not strong enough to access the valence band, but ARPES measurements indicate that the Fermi level in undoped buffer layer is only 0.5 eV above it.

It is also known that oxygen adsorption on semiconducting carbon nanotubes induces a Schottky barrier at the contacts[157, 158], which, as we discussed previously, is very likely to happen for the buffer layer. Further determination of the barrier height as a function of oxygen coverage on the device could be interesting.

A similar effect was observed with water vapor as the adsorbing gas, but the purity of the water was not controlled as well it was for other gases. However, water is also known to p-dope graphene like oxygen[9].

We also study the effect of the presence of ammonia (NH_3). NH_3 is a known electron donor to graphene and carbon nanotubes[9, 159]. In contrast to the case of oxygen adsorption, the NH_3 desorption process seems to have a much higher rate. Fig 4.12 shows the relative change of conductance over time when successively filling the transport chamber with 10 mbar of pure NH_3 and evacuating it. Before the experiment, the chamber is evacuated to 1×10^{-6} mbar and the sample is annealed to 300°C for 1 hour. As expected, the presence of the gas increases the conductance indicating an electron doping effect adding charge carriers to the device. The saturation is reached within a couple seconds and evacuating the chamber restores the initial state. An additional effect seems to be present in the experiment. Indeed, the overall conductance is slowly decreasing overtime regardless of the presence of NH_3 or not. This remains unexplained, although the simplest hypothesis would be that somehow the sample gets slowly contaminated overtime with a non reversible process at room temperature, such as oxygen. The NH_3 bottle is 99.9999% and the gas is sent through a purifier so the source of contamination has not been identified and the experiment should be repeated in a different chamber.

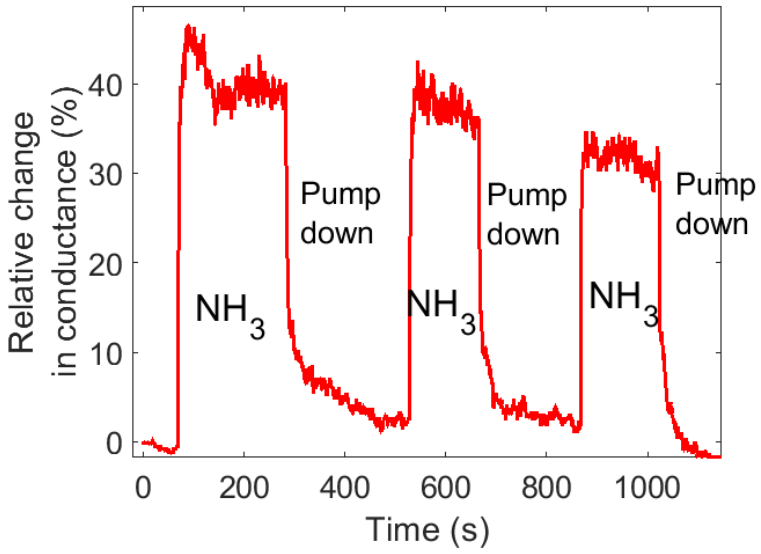

Figure 4.12: Effect of ammonia adsorption on a metal contacted buffer layer device. The relative change of conductance is measured over time. The higher conductance state is observed when the chamber is filled with 10 mbar of NH_3 while the lower conductance is when the chamber is evacuated.

4.3.2 Gated devices

The change in conductance of buffer layer devices in response to the adsorption of gases indicates that the Fermi level is not pinned and can be shifted. In this section, we address the field effect in the devices by fabricating and measuring top gated clean buffer layer devices. A thin film of Al_2O_3 is deposited on top of SWGNR contacted buffer layer devices after annealing in vacuum, as described in section 4.1.3. The film thickness is about 30 nm in total (10 nm deposited by thermal evaporation and 20 nm of ALD). A trilayer Al/Pd/Au is deposited and patterned on top of the devices to produce the gate metal. IV curves are recorded for different gate voltages and temperatures. Fig. 4.13 shows how the current changes with the applied gate voltage in a top gated SWGNR contacted buffer layer device for temperatures between 50 K and 300 K. The bias voltage is held constant at 1 V. The measurement is performed in DC conditions. For temperatures under 50 K, the conduction is below the minimum current measurable by the Keithley 2400. A positive voltage applied on the gate enhances the current while a negative voltages reduces it, which is consistent with electrons being the charge carriers in the device. The highest current ratio between

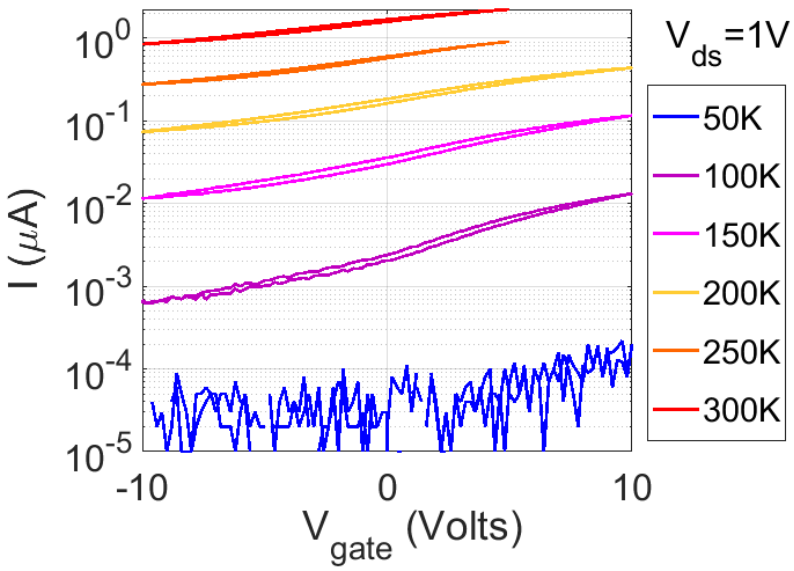

Figure 4.13: Log plot of the current versus gate voltage for V_{bias} = 1 V, measured at various temperatures.

V_{gate} = -10 V and V_{gate} = 10 V is $I_{on/off}$ = 20 at 100 K. The conductance versus gate voltage characteristics do not have an ambipolar characteristic nor a minimum conductance which is inconsistent with the idea that a semiconducting buffer layer. The electron mobility μ can be estimated by the relation[160]:

$$\mu = \frac{\partial I}{\partial V_{gate}} \frac{1}{V_{bias}} \frac{L}{W} \frac{1}{C_i} \tag{10}$$

where L and W are the channel length and width and C_i is the capacitance per unit area of the gate dielectric. In our case, C_i = 29.5 nFcm^{-2} for 30 nm thick Al_2O_3 with ϵ_r estimated at 9.8. The device is 1.2 μm long and 5 μm wide. From the measurement at 300K in Fig. 4.13, this gives a mobility μ = 0.97 cm^{2}V^{-1}s^{-1}. As a comparison, the monolayer graphene grown on top of the buffer layer has a typical mobility μ > 1000 cm^{2}V^{-1}s^{-1}.

4.4 Magneto-transport

The study of the electrical resistivity as a function of an applied magnetic field can provide information about the behavior of the charge carriers in a material[161], such as the carrier type and concentration. Unfortunately, no response above the noise level from a perpendicular magnetic field was observed in the buffer layer. Only an upper limit of the carrier

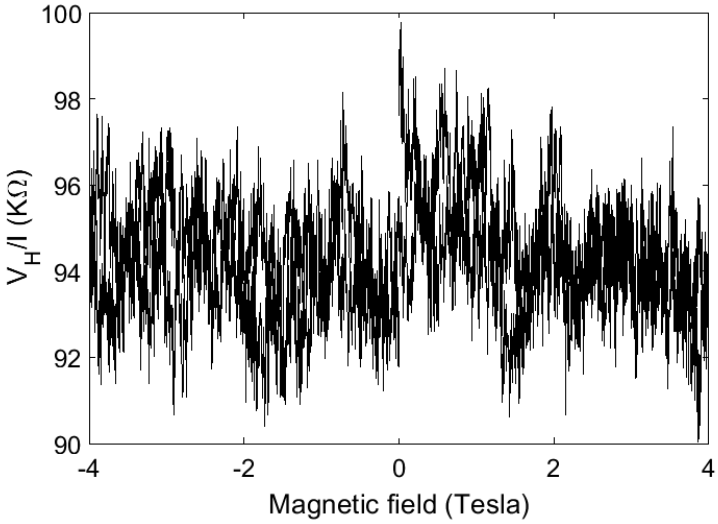

Figure 4.14: Hall voltage measurement at 420 K of a graphene contacted Hall bar measured as a function of an applied perpendicular magnetic field.

mobility in the buffer layer is derived from the data.

4.4.1 Hall measurement

Graphene contacted buffer layer devices in the shape of a Hall bar (Fig. 4.4 a and b) are measured. Fig. 4.14 shows the Hall voltage divided by the current in the device measured at 420 K for a magnetic field swept between -4 T and 4 T. There seems to be two types of noise, a high frequency one and some slower drift drift, but no periodicity is observed. Overall, there is no visible response of the Hall voltage to the applied perpendicular magnetic field. Given the noise level of approximately 4 kΩ , an upper limit for the Hall coefficient is $\frac{4k\Omega}{8T}$ = 500 Ω/T which would correspond to a minimum value of 1.25×10^{12} $cm^2V^{-1}s^{-1}$ for the carrier density. Given a low bias resistivity of 20 $M\Omega_\square$ for this device, the mobility would be at most 2.5×10^{-5} $cm^2V^{-1}s^{-1}$. This is only an estimate and the high resistance of the device makes the measurement difficult. As it was shown in section 4.3.2, the field effect mobility is much larger. One may note that the Hall voltage is quite large overall because of the high resistivity of the buffer layer and an unavoidable small misalignment of the contacts in the Hall bar geometry. This makes the measurement not very reliable. Nevertheless, the high resistivity and the lack of Hall effect suggest a low mobility of the charge carriers in

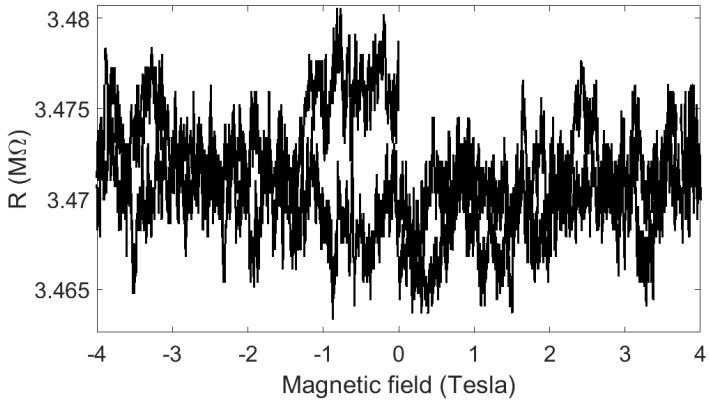

Figure 4.15: Magnetoresistance measurement at 420 K of a graphene contacted two-terminal device measured as a function of an applied perpendicular magnetic field.

the buffer layer.

4.4.2 Magneto-resistance

Magneto-resistance is the change of resistance of a device in response to an applied magnetic field. It can be positive of negative[162], or oscillating with the magnitude of the applied field[3]. It is often linked to the localization and delocalization of the charge carrier in the presence of a magnetic field.

We performed magnetoresistance measurement on both graphene and Pd/Au contacted buffer layer devices and observed no change above the noise level in the resistance in response to a perpendicular magnetic field up to 4 T, at high and low temperatures. Fig. 4.15 shows an example of magnetoresistance measured at 420 K for a graphene contacted device.

4.5 Observation of Mott's variable range hopping

The high resistivity of the buffer layer and the lack of Hall effect or magnetoresistance has left us with little to work on so far, and a model describing the conduction of the charge carriers in the buffer layer needs to be identified. In this section, the effect of temperature and applied electric bias are considered, and it is shown that the data fit extremely well the Mott variable range hopping conduction model.

Temperature always plays an important role in electronic transport, and even a lack of any temperature dependence is a meaningful piece of information[163]. Similarly, the

relationship between bias voltage or bias electric field and the conductance of the device helps identify potential transport mechanisms occurring in the device.

4.5.1 Data acquisition

IV curves are measured over a range of temperature from 4.5 K up to 420 K. The temperature is controlled within 0.001 K by a PID controller. IV curves are performed by sweeping the bias voltage across two terminal devices from a Keithley 2400 DC power supply and the drawn current is measured at each point. This has been done systematically over several tens of devices fabricated on 6 different samples. The data represented in this chapter focuses on four different devices. Devices A and C are 4 μm wide SWGNR contacted buffer layer devices, with a channel length of 1 μm. They have been annealed at 500°C in vacuum and covered with 70 nm of Al_2O_3, 20 nm of it thermally evaporated and 50 nm deposited by ALD. Devices B and D are 4 μm wide Pd/Au contacted buffer layer devices, 0.3 μm long, not covered by any protective layer. They were however annealed in vacuum at 150°C in the cryostat before the measurement. They are therefore all considered to be clean devices. Fig. 4.16 shows the sets of IV curves measured for device A and device B. The curves are non linear and are symmetrical between positive and negative bias voltages. Device A shows little temperature dependence below 100 K for high bias voltage, while for device B it seems less temperature dependent up to 220 K. The analysis in the next two sections shows however that both devices have the same temperature dependence at low bias and same bias voltage dependence at low temperature.

The non-Ohmic behavior of the devices is intriguing. Non-Ohmic resistive effects usually occur in complex components such as semiconductor PN junctions, or at the contacts[163]. There is no evidence for doping inhomogeneity in the buffer layer, although fabrication processes can sometimes lead to local doping[164]. We have already addressed the issue of the contacts for clean buffer layer devices, but a third possibility for non linear conductance is hopping conduction[165], which displays characteristic electric bias and temperature dependence.

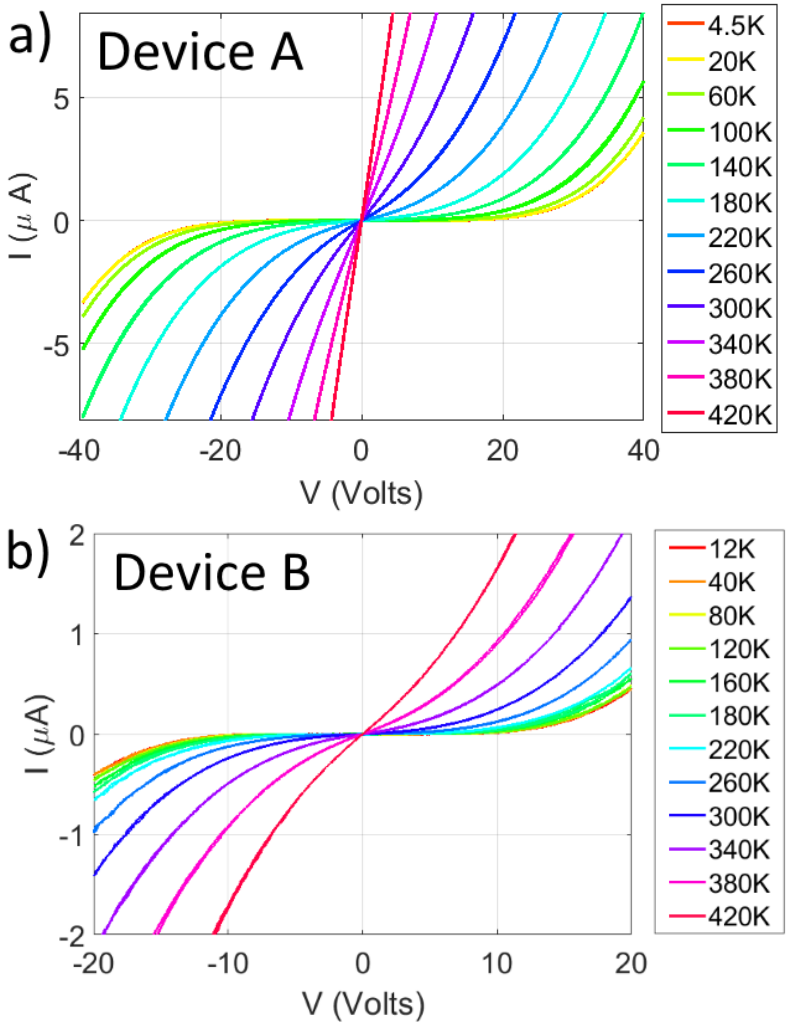

Figure 4.16: IV curves for a) device A and b) device B. As device B is measured in vacuum, the lack of exchange gas did not allowed the sample to cool all the way down to 4.5K.

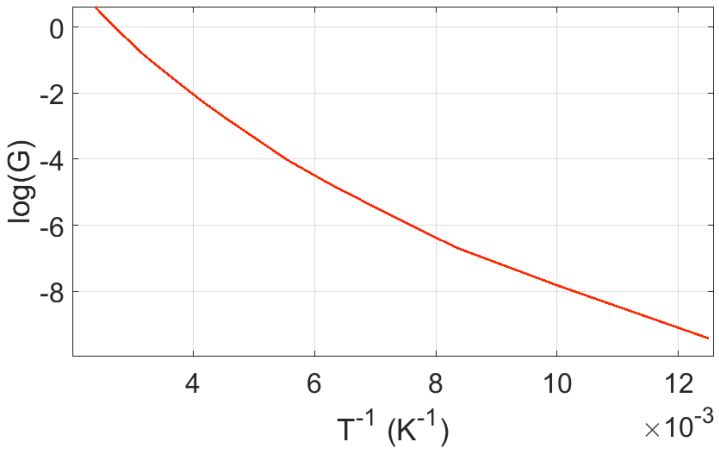

Figure 4.17: Temperature dependence of the zero bias conductance of device A tested for an Arrhenius behavior. The curve is not a straight line showing the absence or such a behavior.

4.5.2 Temperature dependence at low bias voltage

We are first considering the conductance at low bias voltage. Doped semiconductors show an Arrhenius behavior between the conductance G and the temperature T[161]:

$$G(T) = G_0 \, exp\left(- \frac{E_A}{k_B T} \right) \tag{11}$$

where G_0 is a frequency factor and E_A is an activation energy. Other physical phenomena display such a general behavior, such as the activation of charge carriers over a Schottky barrier for example[163]. The plot of the logarithm of the conductance versus $\frac{1}{T}$ for a system following an Arrhenius dependence on temperature should be a straight line. This is however not observed in the buffer layer, as exemplified in Fig. 4.17 for device A.

The curve is not straight, but there seems to be some kind of exponential relationship. We therefore postulate the following Ansatz:

$$G(T) = G_0 \, \exp\left[- \left(\frac{T^*}{T} \right)^{\alpha} \right] \tag{12}$$

where T^* is a constant with the dimensionality of temperature and α an exponent to be determined. The resistance curve derivative analysis (RCDA)[166] is used to find α. The quantity w is defined as:

$$w = \frac{d \log(G)}{d \log(T)} \tag{13}$$

which can be shown to be equivalent to

$$w = \alpha\left(\frac{T^*}{T}\right)^{\alpha} \tag{14}$$

Taking the logarithm of equation 14, it becomes:

$$\log(w) = \log(\alpha) + \alpha\log(T^*) - \alpha\log(T) \tag{15}$$

Therefore, a plot of log(w) versus log(T) is linear with a slope of -α. One down side of this procedure is that it requires smooth data to calculate accurate derivatives or the resulting plot is too noisy to accurately determine the slope. For some sets of data, the RDCA does not result in a meaningful or accurate value of α, but for devices with a better defined temperature dependence, values around 1/3 come up from the analysis as shown in Fig. 4.18 for devices A, B, C and D. This confirms the following relationship:

$$G(T) = G_0\ \exp\left[-\left(\frac{T^*}{T}\right)^{\frac{1}{3}}\right] \tag{16}$$

The logarithm of the low bias conductance can therefore be plotted against $\frac{1}{T^{1/3}}$ which gives a linear plot over the range of temperature and current where equation 16 is valid. As seen in Fig. 4.19, the equation is valid over a several decades of current. The lower temperature of the validity range is limited by the minimum conductance measurable in the setup (around exp(-10) or 4.5×10^{-1} nanosiemens). The values of T^* for device A,B,C and D are reported in Fig. 4.24. They are around 10^6 K.

Equation 16 corresponds to Mott's variable range hopping in two dimensions[167], indicating that it is the dominant mechanism of conduction in the buffer layer. We shall describe its physics in the following section.

4.5.3 Variable range hopping conduction

Variable range hopping conduction was first derived to describe low temperature conduction of negatively doped semiconductors[167]. Here, we introduce the theory following Mott's original work, applied to the case of two dimensional materials. At room temperature, electrons induced by the randomly distributed impurities (dopants) jump to the conduction band and are free to move through the lattice (left on Fig. 4.20). At low temperatures

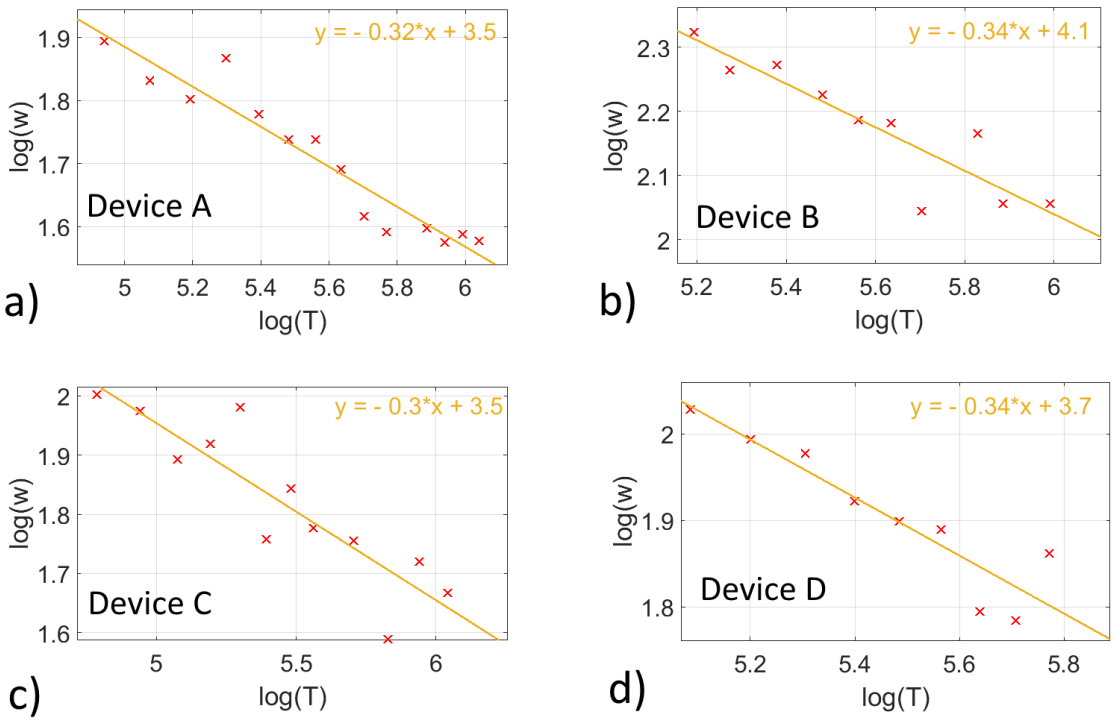

Figure 4.18: Resistance curve derivative analysis of the temperature dependence of the low bias voltage of devices A, B, C and D. They all give a value of α around 1/3.

however, they are localized by the attractive coulomb potential created by the ion and can only move by hopping from one site to another available site (right on Fig. 4.20). The localized electrons can be model as an exponentially decaying wave function centered at the position of the impurity site. The tunneling probability from one site i to another site j is:

$$P = \exp\left(\frac{-2R_{ij}}{\xi} - \frac{E_{ij}}{k_B T}\right) \tag{17}$$

where R_{ij} is the spacial distance between site i and site j, ξ is the localization length representing the attenuation length for a hydrogen-like localized wave-function, and E_{ij} is the energy spacing between the two sites. The first term in the exponential term favors shorter distance hops, while the second term gives a higher hopping probability for sites with small energy difference. The competition between those two terms gives rise to variable range hopping. In its first derivation, Mott made the simple assumption that the further away from the site the higher probability there is to find a state with energy close to the initial state. Assuming that the density of states (DOS) $N(E_F)$ around the Fermi level E_F

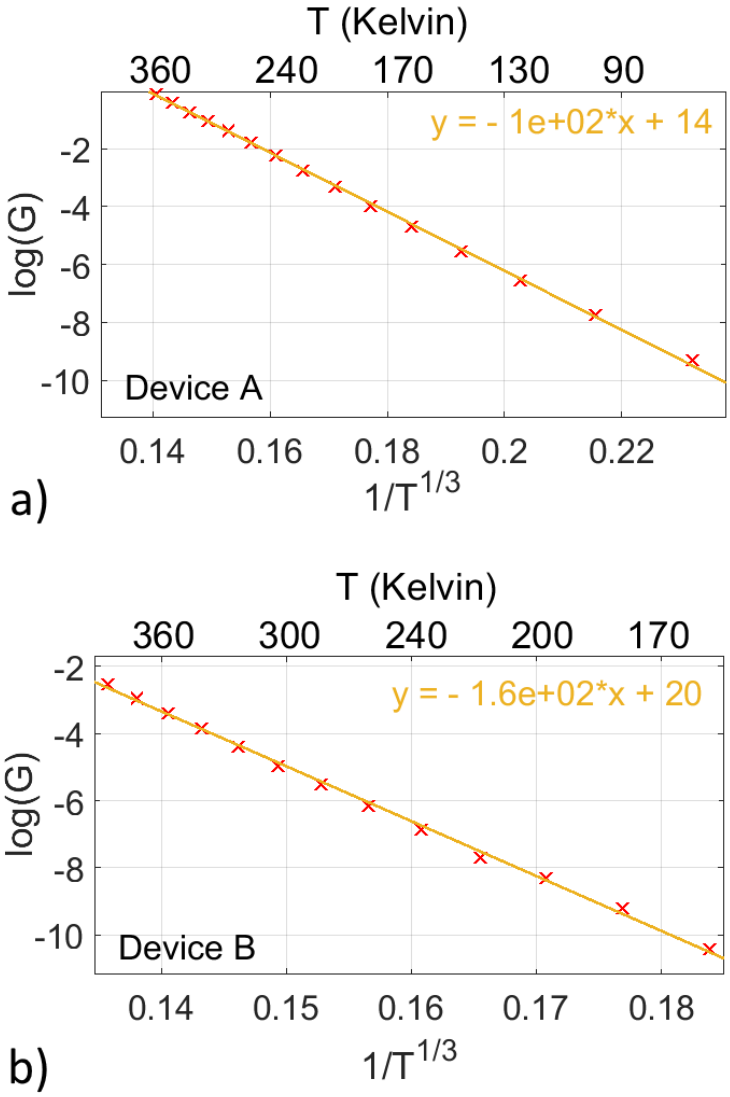

Figure 4.19: Temperature dependence of the conductance of device A and device B. The minimum temperature of the range of validity is limited by the minimum current of the measurement setup.

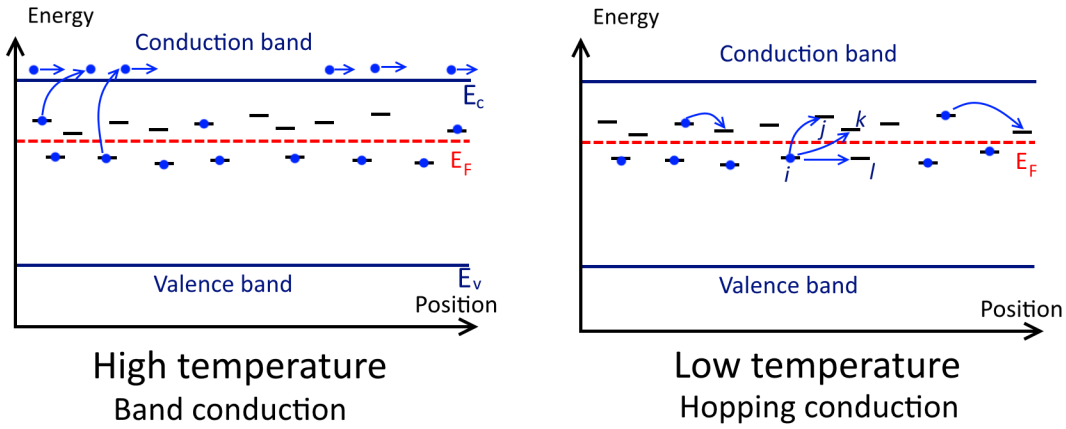

Figure 4.20: Basic illustration of carrier transport in a doped semiconductor. At high temperature (left side), the electrons (blue dots) have enough thermal energy to go into the conduction band while at low temperature (right side), the conduction occurs via hopping from one site to another.

is constant, one can then estimate in two dimensions:

$$E_{ij} = \frac{1}{\pi R_{ij}^2 N(E_F)} \tag{18}$$

Maximizing the expression for the probability with respect to R_{ij}, one obtained:

$$R_{optimal}^3 = \frac{\xi^2}{\pi N(E_F) k_B T} \tag{19}$$

and

$$P_{optimal} = \exp\left[-\left(\frac{T^*}{T}\right)^{\frac{1}{3}}\right] \tag{20}$$

where $T^* = \frac{3}{k_B \xi^2 N(E_F)\pi}$. Finally the current should be a product of the probability for one hop and the attempt frequency of the hopping mechanism. Hence, we obtain equation 16 again:

$$G(T) \propto \exp\left[-\left(\frac{T^*}{T}\right)^{\frac{1}{3}}\right] \tag{21}$$

The constant T^* has only been qualitatively derived. Calculated with percolation theory simulations, the commonly used form for a two dimensional system is[165]:

$$T^* = \frac{13.8}{k_B N(E_F) \xi^2} \tag{22}$$

In summary, Mott variable range hopping theory is a formalism aiming to describe the

physics of localized electrons in a random network of trapping sites. The power of this theory resides in the simplicity of the initial argument, and the relationship between conductance and temperature given in equation 16 has been observed in many 3D (where 1/3 is replaced by 1/4) and 2D systems: amorphous materials[168, 169, 170, 171], polycrystalline materials[172, 173], graphene oxide[174] and graphene reduced oxide[24], quantum dots solids[175, 176], and quasicrytals[177].

At this point, we would like to point out that electron-electron interaction effects can occur in a variable range hopping system. The formation of a coulomb gap in the DOS at low temperature arises from the long range coulomb interaction between electrons, which adds an extra potential energy to overcome in the process of hopping from one localized site to another[178]. This reduces the conductivity predicted by Mott and it was shown that equation 16 is changed to the Efros-Shklovskii variable range hopping relation:

$$G = G_{ES} \exp\left[-\left(\frac{T_{ES}}{T}\right)^{\frac{1}{2}} \right] \tag{23}$$

with T_{ES} a constant with the dimensionality of temperature and the exponent 1/2 being the same in all dimensions. The buffer layer transport fits Mott's version of variable range hopping rather than Efros-Shkloskii's, indicating insignificant electron-electron interactions.

Screening of the coulomb interactions has been suggested for a two dimensional variable range hopping system in the presence of a parallel metal gate[179]. As we will discuss in the next chapter, the SiC substrate could play a very important role in the presence of variable range hopping in the buffer layer, and could be responsible as well for such screening. Alternatively, a cross over from Efros-Shklovskii to Mott variable range hopping has been observed in quantum dot solids by decreasing the concentration of electrons in the material[175], indicating that a low concentration of electrons would not experience a coulomb gap in the DOS. A definitive conclusion regarding the importance of electron-electron interactions in the buffer layer would require further investigations.

4.5.4 Electric bias dependence at 4.2 K

At this point, we have only analyzed the low bias voltage part of the data measured. The IV curves of Fig. 4.16 present a clear non-linearity and their shape, as it turns out, is also a

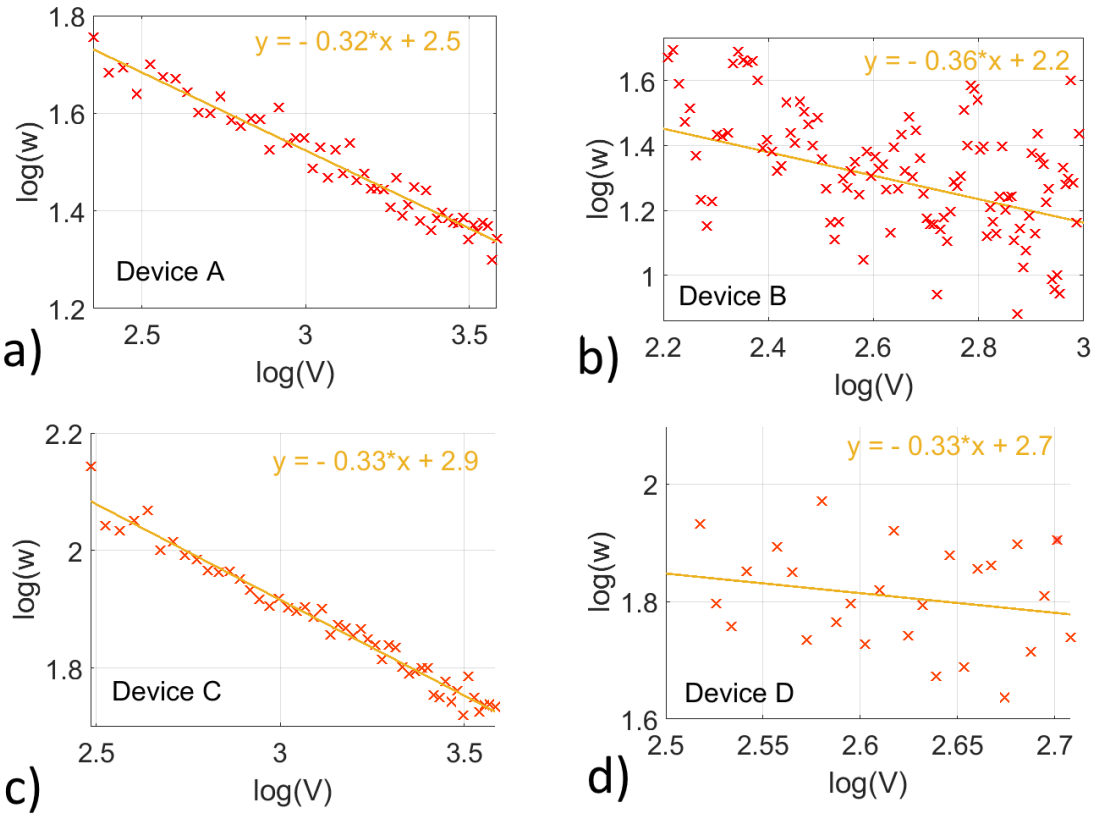

Figure 4.21: Resistance curve derivative analysis of the voltage dependence of the low bias voltage of devices A, B, C and D. They all give an value of α around 1/3 despite a large dispersion devices B and D.

signature of 2D variable range hopping. The RCDA of the differential conductance G=$\frac{dI}{dV}$ dependence on the electric field E measured at 4.2 K is shown in Fig. 4.21 for devices A, B, C and D. The electric field seems to play a similar role to the temperature as the RCDA indicates that G(E)$\propto \exp[1/E^{1/3}]$.

The specific dependence of the differential conductance G=$\frac{dI}{dV}$ on the bias electric field is another evidence that the contacts (graphene or metal) do not play a dominant role in the resistance of the buffer layer devices even at low temperature as it fits the hopping model rather than a Schottky diode equation ($\log(I_{Schottky}) \propto V_{bias}$)[180].

It was predicted by Shklovskii that localized electrons in the variable range hopping regime can be driven out of their trapping sites by an external electric field[181]. This is a distinct effect from the Poole-Frenkel effect, which occurs when trapped electrons are moved into the conduction band of a semiconductor by an external electric field[182]. In the presence of the Poole-Frenkel effect, the logarithm of the current increases as the square root of the applied voltage while for 2D variable range hopping conduction, it increases as $V^{-1/3}$.

In the presence of an external electric field $\boldsymbol{E}$, the electrons have additional energy. An elegant way to visualize it is to consider the energy band diagram along the device channel. A potential difference between source and drain induces a bending in the energy bands, as shown in Fig. 4.22. As the electric field increases, more states are energetically accessible to hop to. Even at zero temperature, transport is possible as long as the field is strong enough. Mathematically, the energy from site i to site j in equation 18 is reduced by the electric potential energy difference between the sites:

$$E_{ij} = \frac{1}{\pi R_{ij}^2 N(E_F)} - eER_{ij} \tag{24}$$

Maximizing the new expression for P with respect to R_{ij} and evaluating it at zero temperature gives optimal hopping distance:

$$R_{optimal}^3(T=0) = \frac{2}{\pi N(E_F) eE} \tag{25}$$

which finally leads to the zero temperature variable range hopping expression in a strong

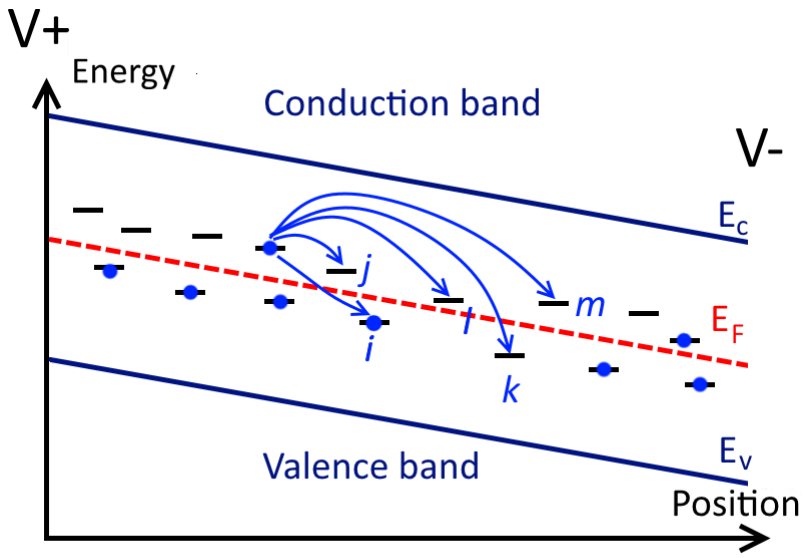

Figure 4.22: The band bending in a strong electric field increases the number of states accessible by hopping.

electric field:

$$G(E) = G_1 \exp\left[-\left(\frac{E^*}{E}\right)^{\frac{1}{3}}\right] \tag{26}$$

where $E^* = \frac{k_B T^*}{2e\xi}$ according to this simple derivation. Equation 26 is in accordance with our experimental observation (Fig. 4.21). Fig. 4.23 presents the differential conductance at 4.2 K plotted against $1/E^{1/3}$. As expected, the model fits over a wide range of current down to the minimum measurable current in our setup. The values of E^* are reported in Fig. 4.24.

4.5.5 Effective temperature, localization length, and density of states

We have shown that near zero temperature, the electric field plays a role analogous to the temperature. As T rises, a mixture of thermally activated and electric field driven transport occurs. The concept of effective temperature (T_{eff}) as been introduced[183, 184, 185] in an attempt to unify the effects of temperature and electric field in a hopping system. Marianer and Shklovskii proposed the following form of T_{eff}[183]:

$$T_{eff}^2 = T^2 + (0.67eE\xi/k_B)^2 \tag{27}$$

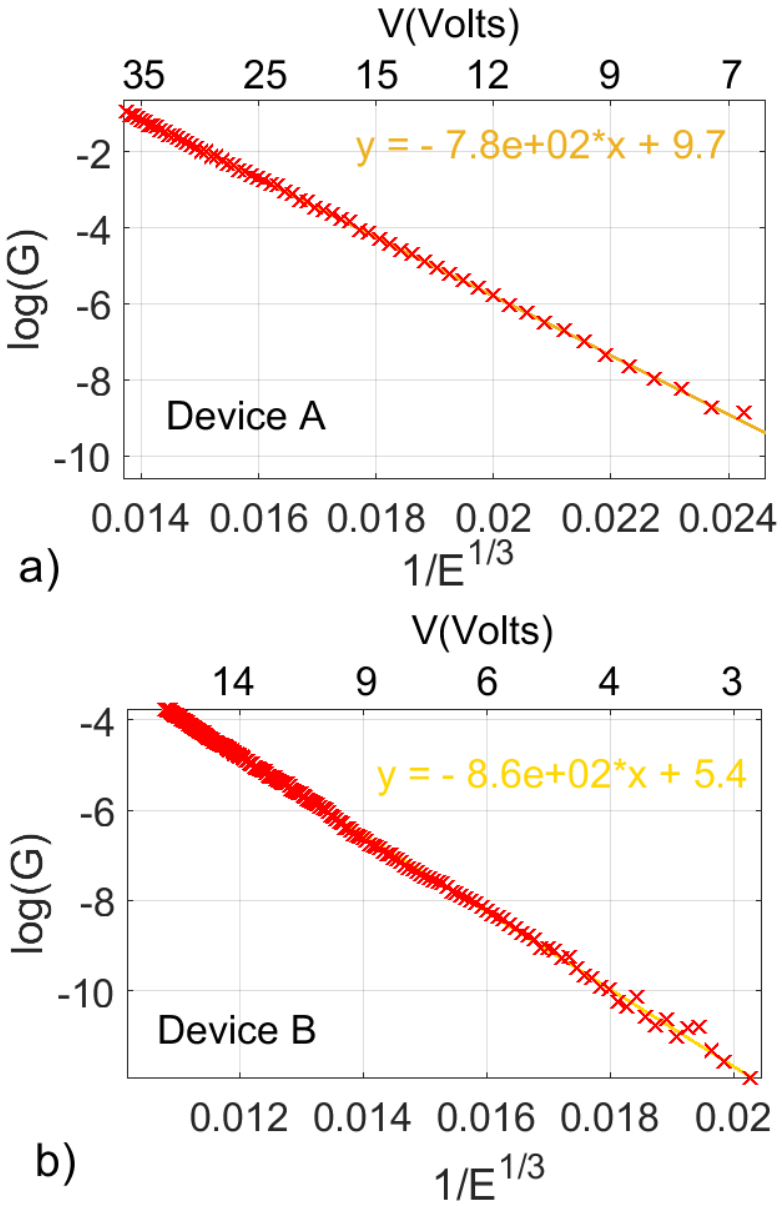

Figure 4.23: Biased electric field dependence of the conductance of device A and device B at 4.2 K.

The factor 0.67 is determined by numerical calculations simulating the hopping transport in the band tail of amorphous semiconductors, i.e. an exponentially increasing DOS with energy. As it is pointed out in a review on the concept of effective temperature[186], equation 27 still lacks a physical interpretation. Nevertheless, including T_{eff} in our model implies:

$$G(T_{eff}) = G_3 \exp\left[-\left(\frac{T^*}{T_{eff}}\right)^{\frac{1}{3}} \right] \tag{28}$$

which we already know works in the limit of T→0 and E→0 for the buffer layer. This gives us a refined relation between T^* and E^*:

$$E^* = \frac{k_B}{0.67e\xi} T^* \tag{29}$$

The values of T^* and E^* are measured for multiple devices coming from different samples and they are plotted against each other in Fig. 4.24. The data contains both metal-contacted and SWGNR-contacted buffer layer devices. Besides a few outliers, most of the data points are falling on a line extrapolating towards the origin (within 3-5%) which is in agreement with equation 29. If our model is correct, the slope of the fit gives the average value of $\frac{k_B}{0.67e\xi}$ and we can extract the average localization length ξ, which characterizes the radial decay of the wavefunction of a localized electron. According to the fit of Fig. 4.24 It is found that ξ=2.19 nm for the buffer layer. Equation 22 relates T^* with ξ and $N(E_F)$, the DOS around the Fermi level. The value of T^* varies by an order of magnitude, which means that the DOS around the Fermi level changes slightly from device to device. $N(E_F)$ is calculated to be between 6.28×10^{11} and 1×10^{13} $cm^{-2}eV^{-1}$. The outliers devices of Fig. 4.24 remain unexplained. While the values of T^* are directly accessible from the data, the determination of E^* requires the knowledge of the dimensions of the device in order to convert the voltage into the electric field. There could be a source of error in what is expected to be the geometry of the device (problem of fabrication and characterization of the device) or some unexpected and unknown potential drops could occur in the circuit (bad contacts, for instance), but the fabrication process of those devices was the same as the others.

Finally, we attempt to fit the data for all voltages at all temperature according to the effective temperature model. Until now, we have ignored the pre-exponential factor in our

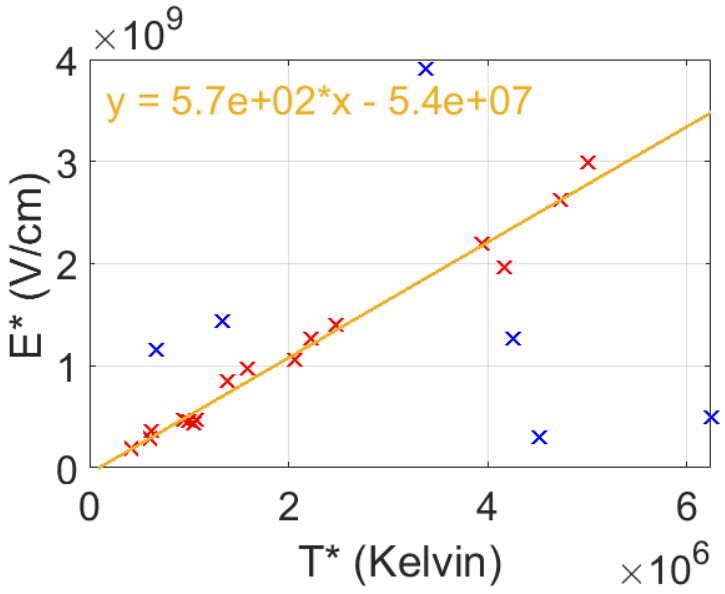

Figure 4.24: E* plotted versus T* for different buffer layer devices and samples. The linear fit is calculated for the data in red. Blue crosses are outliers and are not taken into account in the fit.

model. In the variable range hopping picture, it represents the attempt frequency of the hopping mechanism. Its temperature dependence is often ignored, which is reasonable if the DOS around the Fermi level is considered to be constant[165]. From the analysis done in Fig. 4.19, its value for device A is about exp(9.7). A nonlinear least square fitting method is applied at each temperature with ξ as the fitting parameter. The result is shown in Fig. 4.25a with the corresponding fitted values of ξ as a function of temperature in Fig. 4.25b. The fitting of the voltage dependence is not perfect and this method gives a lower value of the localization length (between 0.8 and 1.3) compared to the previous value of 2.19 nm. Nonetheless, this shows that the effective temperature model works to a certain extend. A better determination of the pre-exponential factor form would certainly improve the fits. Advanced numerical methods such as Monte Carlo simulations are most commonly used to study the variable range hopping conduction and determine the energy spectrum of the material[187].

We have shown in this chapter how the mobility is limited by the localization of the electrons in the buffer layer. The trapping of the charges manifests itself by the presence of a two dimensional Mott variable range hopping conduction. The localization length of the

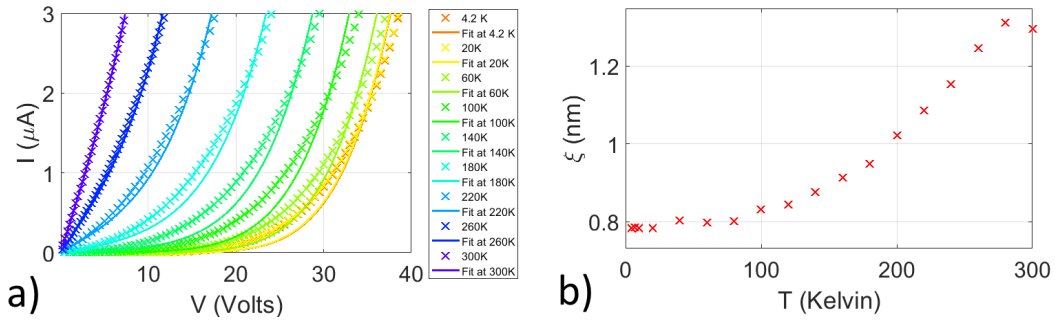

Figure 4.25: a) IV curves of device A and their fit according to equation 28 with ξ as a fitting parameter. b) Fitted values of ξ at each temperature.

electrons is found to be between 0.8 and 2.2 nm, a length scale reminiscent of the 1.8 nm periodicity of the buffer layer corrugation. So far, we have not commented on the origin of the localization of electrons, which is the focus of the next chapter.

CHAPTER V

DISCUSSION OF THE VARIABLE RANGE HOPPING CONDUCTION IN THE BUFFER LAYER

The observation of Mott variable range hopping in the epitaxial graphene buffer layer has come as a surprise. By essence, variable range hopping conduction is associated with disordered materials. According to solid state physics and Bloch's theorem, electrons in a periodic lattice of ions are described by Bloch waves, delocalized wave functions presenting the same periodicity as the lattice[161]. When that periodicity is broken, Bloch theorem is no longer valid and localization can occur[188]. We have shown in chapter 3 how the buffer layer is a well organized graphene layer and not an amorphous or defective material. This brings up two questions: what is the origin of localization of electrons in the buffer layer, and why does the transport follow a variable range hopping conduction when the buffer layer is seemingly a perfectly ordered material? This chapter aims to bring some insight on those questions by considering possible scenarios regarding this apparent contradiction.

5.1 Electron localization in 2D and quasi 2D systems

We first compare our experimental observations with the hopping transport seen in other systems with an emphasis on carbon based materials. The similarities and differences between the buffer layer and those materials are discussed in order to highlight the uniqueness of the buffer layer.

5.1.1 Variable range hopping in carbon materials

Variable range hopping was initially predicted to be a low temperature phenomenon in order for the charge carriers to be in a localized regime[167]. We saw in the previous chapter how the buffer layer exhibits this mode of conduction up to at least 420 K, indicating quite a significant localization effect, where tunneling between traps persists above room temperature. Such a large dynamical range of validity has been observed in many materials,

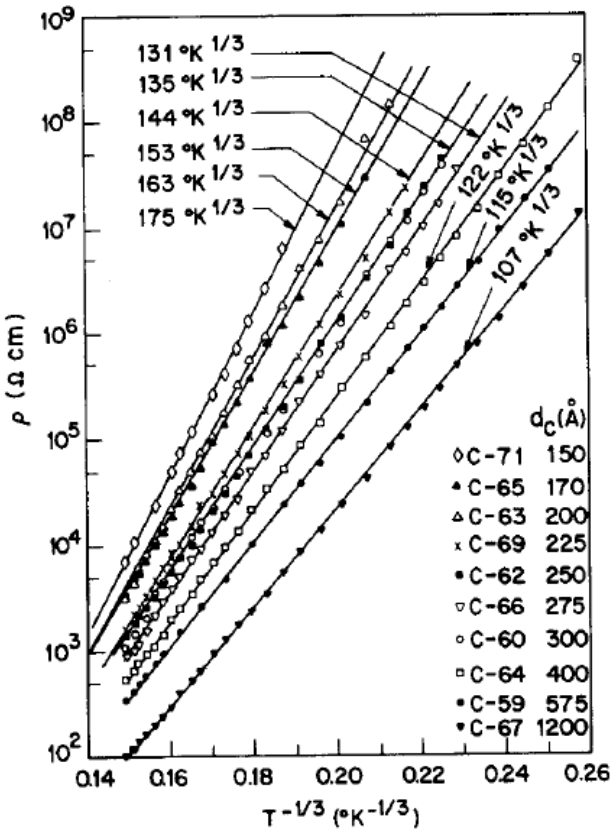

Figure 5.1: Temperature dependence of amorphous carbon thin films showing a 2D Mott variable range hopping conduction. From reference [170].

including carbon based ones: amorphous carbon (aC) for example, has been shown to obey 3D Mott variable range hopping between 30 K and 300 K[169] with T^*_{3D}= 7×10^7. As the thickness of aC is reduced, a transition to 2D transport is observed[170] as shown in Fig. 5.1. The localization length ξ was then estimated to be 1.2 nm giving N(E_F) = 10^{18} eV^{-1}cm^{-3}. A more recent study shows how the model of conduction extends up to 500 K for hydrogenated aC[189, 190]. The localization is interpreted as π-electrons localized in sp^2 clusters embedded in a hydrogenated sp^3 carbon matrix. They estimates the contribution of σ-electron to be negligible in this range of temperature.

The degree of localization was shown to be dependent on the structure of the films, as reviewed by Robertson[191]. The deposition method can produce either true amorphous carbon, or carbon with highly conductive path of graphite-like carbon. In addition, the electrical properties of aC are modified upon heat treatments, first by increasing the DOS

of hopping sites and eventually leading to graphite nanocrystallization of the films displaying a metallic behavior.

The high bias conduction in amorphous carbon is also non linear[192, 193]. However, the field dependence was shown not to follow the effective temperature model: the conductivity is in the form $\sigma = \sigma_0 \exp(E^n/E_n)$ where n=2 at low field and n=1/2 at high field. This was interpreted as a transition from the Apsley-Hughes model[194] (describing intermediate bias voltage effect in the variable range hopping in 3D) to the Poole-Frenkel effect.

While the behavior of aC resembles the observations made on the buffer layer, aC is very different structurally as it intrinsically lacks periodicity. In the case of hydrogenated aC, one expects a range of different sizes of sp^2 bonded graphite clusters leading to a spectrum of energy states within the band gap of aC[195]. This is inconsistent with the regular 6×6 periodicity of the buffer layer.

Variable range hopping has also been observed in functionalized graphene samples, such as reduced graphene oxide (rGO)[24]. The conduction was found to follow Mott's model from 80 K to 300 K with T_* around 7×10^5 K which is close to the parameters we found for the buffer layer. Other studies have also found the high field conduction to follow equation 26 at low temperature[196]. rGO is a disordered material, generally considered to be a mixture of graphitic islands surrounded by sp^3 functionalized graphene oxide boundaries, reminiscent of the nature of hydrogenated amorphous carbon.

Other systems can display variable range hopping. For the sake of time and relevance, we will simply list some of them here. Hydrogenated graphene, or graphane, fit the Efros-Shlovskii model between 10K and 300K, with T_{ES}=250K[110]. Mott variable range hopping was observed from 80 K to 300 K for a few layers of non-reduced graphene oxide with $T^*=1\times10^6$ K[174]. Both of those materials are expected to be highly disordered due to the randomness of the functionalization process. We point out that high temperature variable range hopping (Mott or Efros-Shlovskii) is regularly reported for other two and three dimensional materials such as MoS_2[197, 198, 199], black phosphorous[200], or quantum dot solids of various composition[172, 175, 201, 176, 202]. The case of quantum dot solids is quite interesting as localization is an intended effect when fabricating these materials. They can

exhibit a relatively well ordered structure (size distribution of 7%) and yet, the small difference in energy from dot to dot leads to a variable range hopping type of conduction, both in the ohmic regime (low bias) and the non linear regime at low temperature[175, 202]. This suggests that strong disorder may not be a necessary condition for variable range hopping to occur, as long a the electrons are well localized.

In conclusion of this section, high temperature variable range hopping is commonly observed in certain materials, suggesting the presence of strongly localized charge carriers in those systems. In graphitic material, the charges are often considered to be localized in isolated sp^2 islands surrounded by disordered boundaries. While disorder is intrinsic in those material, the case of quantum dots solids indicates that a strong localization effect could be more relevant than the randomness of the density of states for variable range hopping to occur.

5.1.2 Localization in periodic graphene structures

Before we attempt to model the electronic structure of the buffer layer, this section shortly addresses some localization effect in graphene structures to demonstrate that electron localization is not always a result of disorder. For example, some interesting phenomenon can be observed by varying the angle between two graphene layers on top of each other.

Twisted bilayer graphene (TBG) structures have been actively studied in recent years[203, 204, 205, 206]. The electrons are localized on a Moiré pattern in the form of a triangular lattice in the case of some every specific twisting angles, referred to as "magic angles". Flat bands are predicted to appear at the Fermi level when the twist angle between the two graphene layers reaches such a magic angle, as a result of the interlayer hybridization. These interactions manifest themselves as a renormalization of the Fermi velocity at the Dirac point, which can be visualized as a Dirac cone flattening itself. The Fermi velocity become zero for magic angles where the interlayer hybridization is stronger that the kinetic energy, inducing localization of the electrons. In a very recent experiment, the existence of a Mott insulating phase was observed at very low temperature[207], indicating that localization in a perfectly ordered graphitic system is indeed possible. In fact, Mott transitions

from a metallic behavior to an insulating state are a more general concept where the single electron band structure depiction of the electronic transport fails[208]. Many body effects, not taken into account in the non-interacting electron picture can lead to such transition when the necessary conditions (temperature, pressure, concentration) are fulfilled. We will not go into the details of such a rich field of physics, but this points us towards alternative possibilities regarding the localization in the buffer layer.

5.2 Image charge potential as the origin of localization in the buffer layer

So far, we have reviewed some 2D and 3D systems with variable range hopping as the main mode of conduction up to room temperature or above. In particular, electrons in graphitic systems with disordered phases are subject to a strong localization effect, and the conduction is only made possible by hopping from one graphite like domain to another. While exact structure of the buffer layer remains to be determined, it is known that no more than 26% of the carbon atoms are expected to be close enough to the substrate to create a covalent bond[67]. Whether or not this bonding involves a change in hybridization to sp^3 in those carbon atoms, this number is much less than the amount of hybridized carbon atoms in the disorder graphite and graphene systems that we have been referring to.

Another very important point that needs to be emphasized is the fact that the conduction band of the buffer layer was not observed even after being covered with Cs atoms. The transport is not consistent with the single electron picture of band structure. In light of this knowledge of the buffer layer, a simple model of electron localization is developed in this section.

5.2.1 Classical calculation of the image potential

We recall that the buffer layer is a corrugated graphene layer situated on top of SiC, and that XRR and XSW analyses have demonstrated that the last layer of SiC, while depleted in Si atoms, is not significantly corrugated[67]. The distance between the bottom of the corrugation is estimated to be on the order of an atomic bond length, while the top of the corrugation is fairly decoupled from the substrate, making the buffer layer quite a unique

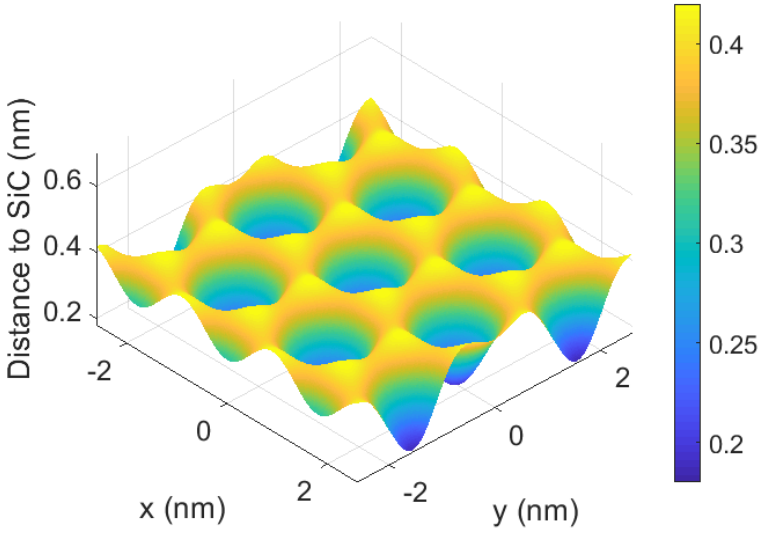

Figure 5.2: Modelization of the buffer layer topography.

system. In addition, STM images and XRD measurement indicate that the surface follows a 6×6 reconstruction with an hexagonal symmetry, giving the corrugation periodicity around 1.8 nm[117, 66]. This is also confirmed by TEM images[68]. From the Mott variable range conduction analysis, we estimate the electron localization length to be somewhere between 0.8 and 2.2 nm, and we hypothesize that the transport properties are linked to the unique structure of the buffer layer. In this model, we consider that the interaction with the substrate does not involve an sp^3 hybritization in the buffer layer.

The distance d between SiC and the buffer layer as a function the lateral position (x,y) can be approximately described by:

$$d(x,y) = d_{min} + \Delta d \times f_{hex}(x,y) \tag{30}$$

where d_{min} is the minimum distance from the SiC substrate, Δd is the amplitude of the corrugation and f_{hex}(x,y) is a function of hexagonal periodicity varying from 0 to 1. It has the form:

$$f_{hex} = 1 - \frac{1}{9}\left(1 + 4\cos\left[\frac{2\pi}{a}x\right]\cos\left[\frac{2\pi}{\sqrt{3}a}y\right] + 4\cos^2\left[\frac{2\pi}{\sqrt{3}a}y\right]\right) \tag{31}$$

where a ≈ 1.8 nm is the periodicity of the corrugation. Fig. 5.2 is a surface plot of equation 30 with parameters $d_{min} \approx 0.18$ Å and $\Delta d \approx 0.24$ Å taken from reference [67].

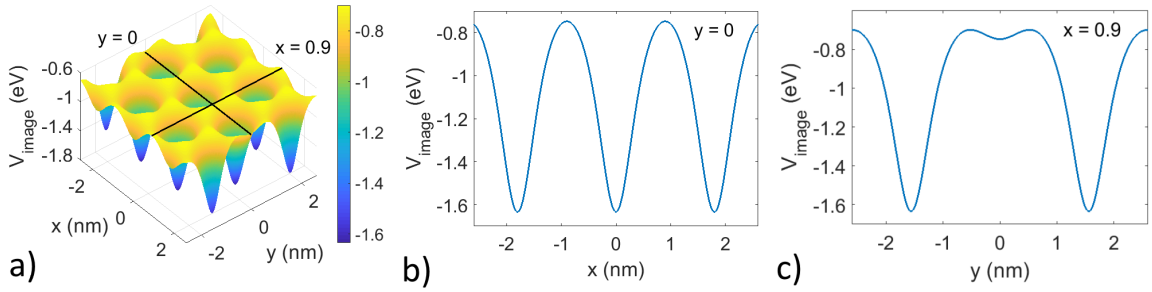

Figure 5.3: Image charge potential of a point charge in the buffer layer. a) Image potential map of a point charge in the buffer as modeled in Fig. 5.2. b) and c) Slices of V_{image} along the x and y directions.

From the model given by equation 30, one can consider the electrostatic potential experienced by an electron constrained to the buffer layer plane near the surface of SiC. Elementary electrostatics tells us that a point charge situated at a small distance d near the surface of a dielectric material sees an attractive potential created by the induced polarization in the dielectric. A simple way to calculate the strength of this potential is by using the method of images[85]. The polarized surface creates the same electric field that a fictional charge of opposite sign at a distance d into the dielectric would create. If we (simplistically) model an electron in the buffer layer as a negative point charge, the potential energy V_{image} as seen by the electron is:

$$V_{image} = -\frac{\epsilon_{SiC} - \epsilon_{vac}}{\epsilon_{SiC} + \epsilon_{vac}} \frac{e}{4\pi\epsilon_0 \left(4d(x,y)\right)} \tag{32}$$

where ϵ_{SiC} ≈10 and ϵ_{air} =1. Fig. 5.3a shows a plot of the image charge potential in the buffer layer as given by equation 32. Fig. 5.3b and c show that the depth of the potential wells experienced by electrons in the buffer layer is $E_{wells} = 0.93$ eV, corresponding to more than 10000 K. This is consistent with the localization in the buffer layer observed up to at least 420 K, as thermionic emission in the form $\exp[-\frac{E_{wells}}{k_B T}]$ would not give significant contribution to the current and only tunneling (hopping) from site to site is possible.

While this calculation only considers point charges, it nevertheless points out the importance of the image potential. The depth of the wells is large enough that it certainly could be the origin of the localization in the buffer layer.

We also consider the influence of slight variations of the distance between the bottom

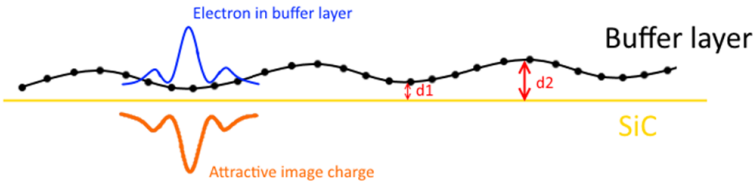

Figure 5.4: Realistic image charge in the buffer layer should consider the wave function of the electron rather than a point charge.

of the buffer layer corrugation and the substrate. A simple difference of 0.05 Å in d_{min} leads to a variation of 44 meV in the well depth, indicating a high sensitivity of the image potential on the actual topography. A realistic buffer layer corrugation may induced an array of wells with different depth, which could play a role in the manifestation of Mott variable range hopping in the buffer layer rather than hopping to the nearest well. This would require further theoretical investigation, and numerical simulations of the transport in the buffer layer taking into account the image potential of electrons would be insightful.

A more realistic picture should however consider the actual wave function of electrons in motion through the corrugation of the buffer layer, as depicted in Fig. 5.4. Such a model involves a quantum mechanical formulation, which we will comment in the next section.

5.2.2 Quantum effects

Without entering into much details, we consider here the quantum mechanical formulation of the problem. First, it is interesting to note that the image potential only exists where the electron is. It can therefore viewed as a "self"-potential leading to self-localization effect. The idea of self-localization has been of interest in the context of Mott insulators[209] and in the case of electron-phonon coupling or the formation of polarons[210]. Self-trapping of electrons due to their image potential was observed by femtosecond time- and angle-resolved two-photon photoemission spectroscopy in a thin alkane layer on top of a metal[211].

The introduction of the image potential term in the Schrödinger equation was considered for the case of graphene near a metal surface (such as a gate metal)[212]. As the potential depends on the electron charge density itself, this leads to a nonlinear Schrödinger's equation

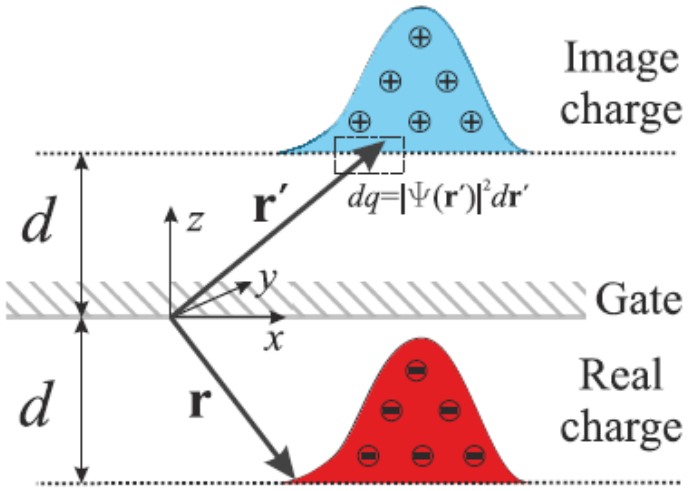

Figure 5.5: Schematic view of electron probability density near metal gate and density of image charge. Reproduced from [212].

(NLSE):

$$i\hbar\frac{\partial\Phi(\mathrm{r},t)}{\partial t} = -\frac{\hbar^2}{2m^*}\Delta\Phi(\mathrm{r},t) - \frac{e^2\Phi(\mathrm{r},t)}{2\kappa}\int\frac{|\Phi(\mathrm{r},t)|^2 d\mathrm{r}'}{|\mathrm{r}-\mathrm{r}'|} \tag{33}$$

where κ is a dielectric permittivity, m^* the effective mass of electrons and the integration is performed over the image charge density as represented in Fig. 5.5. It was shown that solutions of the NLSE can give rise to localization in graphene up to room temperature, adding some justification to the idea of image potential effects in the buffer layer. In this case however, the integration of the potential term should take into account that d is a function of the position (x,y) in the buffer later rather than a constant.

As mentioned previously, a careful theoretical study of the consequences of image potential in the buffer layer is needed in order to fully understand how it can be linked to the observed transport properties. It is possible that the randomness required for variable range hopping arises as fluctuations of purely quantum origins, but our goal here is merely to show the virtue of this idea.

5.3 Alternative model

We end this chapter by mentioning an alternative model of localization in the buffer layer. It is quite the opposite of the idea of localization at the bottom of the corrugation, as it considers the charge density to be concentrated on the areas of the buffer layer that are the

furthest from the substrate. This model for the localization of electrons has the advantage to be similar to what has been observed in epitaxial graphene on ruthenium (Ru), where the large periodic corrugation of the first layer give rise to localization of electron at the top parts of the Moiré pattern[213]. In connection to the image potential mentioned in the previous section, two photons time-resolved photoemission experiments unveiled the localized nature of an image potential state in the hills of the corrugation of the buffer layer on Ru[214]. Such an experiment would be of interest in further studies on the buffer layer.

Fig. 5.6a, reproduced from [66], shows a proposed model of bonding between the buffer layer and the SiC represented over a $6\sqrt{3}\times6\sqrt{3}$ unit cell. As discussed in chapter 3, it considered there the fact that the buffer layer is incommensurate with the underlying SiC. A scheme based on lateral distance between carbon atoms of the buffer layer and silicon atoms of SiC was the starting point of a tight-binding calculation yielding the charge density shown in 5.6b. This model yields decoupled graphene islands surrounded by a mixture of sp^2 and sp^3 carbon boundaries. Although the tight binding calculations yield a semiconducting band structure, this model is reminiscent of the embedded graphitic islands in amorphous carbon and rGO. Several issues can be pointed out in this model however, as it does not quite reflect the observed quasi 6x6 reconstruction but rather the $6\sqrt{3}\times6\sqrt{3}$ one, and their band structure does not reproduce important features in ARPES. In addition, the conduction band and electron-hole symmetry predicted by this model has not been observed in the buffer layer so far. The size of the graphene "dot" is however consistent with our estimation of the localization length and it reflects the idea of decoupled regions in the buffer layer surrounded by strongly interacting boundaries and can be compared to a quantum dot solid; although some amount of disorder in the size of the islands would be needed to induce the variable range hopping conducion.

Although we are not able to make a definitive conclusion regarding the origin of localization in the buffer layer, we argue that the attractive image potential from the substrate should not be ignored and could play a significant role in causing self-trapping of the electrons within the corrugation of the buffer layer. The consequences of this self-potential on

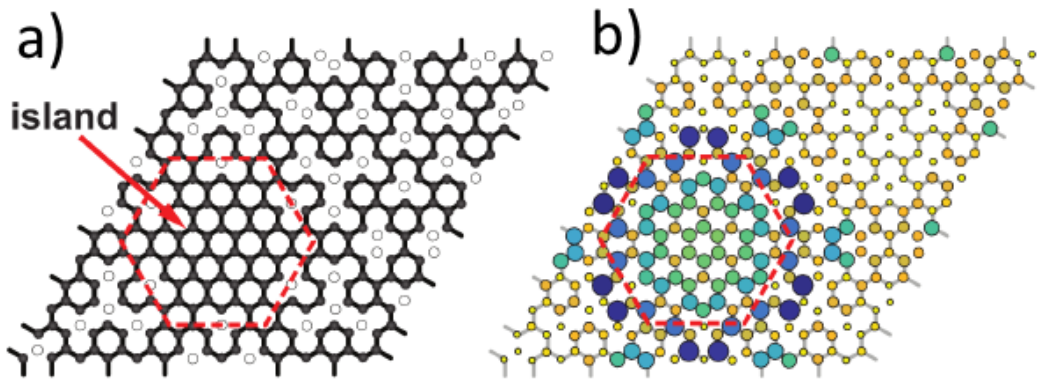

Figure 5.6: (a) A model structure based on modulated SiC layer (Black circles are carbon unbonded to the SiC. Gold circles are carbon bonded to Si in the interface layer below.). Red dashed hexagon marks the boundary of an isolated graphene island. (b) The calculated charge density (arbitrary units) at E=-0.6 eV for the structure in (a). Reproduced from [66].

the transport properties are not known at this time. Theoretical work using the nonlinear Schrödinger equation is needed to further develop the model and check its consistency with the experimental results.

CHAPTER VI

CONCLUSION

6.1 Thesis summary

In this thesis, I presented the investigation of the electronic transport properties of the buffer layer, the first graphene layer grown on SiC(0001). While the motivations for this study were geared towards possible applications of the buffer layer as an electronic material, this work has unveiled some unusual physics taking place in this system.

With improved fabrication processes, graphene and metal contacted buffer layer devices have been fabricated on single SiC terraces. The surface preparation and the well-defined geometry of the devices guarantee the integrity of the buffer layer area by preventing shorts from graphene ribbons growing on natural SiC steps. The contribution of the contacts to the device resistance was shown to become negligible upon desorbtion of oxygen, indicating that Ohmic contacts are achievable on the buffer layer as long as the devices are clean from adsorbed impurities. In the presence of oxygen, the resistance increases by a factor of several hundred, and the IV curves become non-symmetrical, indicating the formation of a Schottky barrier. In contrast, the adsorption of ammonia simply enhances the conduction by adding electrons in the buffer layer. The overall high resistivity of the buffer layer, above 10 MΩ per square for clean samples, can be tuned by about a factor 20 by the voltage applied on a top gate. These transport results are inconsistent with the predicted semiconducting properties.

The conduction mechanism in clean buffer layer samples was then studied as a function of temperature and bias voltage, revealing a two dimensional variable range hopping, following the theory developed by Sir Nevill Francis Mott. The analysis showed that the electrons have a localization length between 1 and 2 nm, and the transport is occurring via hopping from one localized site to another.

This behavior was then interpreted in light of what is known on the atomic and electronic

structure of the buffer layer. Despite the presence of dispersive states in the valence band of the buffer layer, we were unable to populate the conduction band by doping the buffer layer with Cesium atoms. The probable absence of a dispersive conduction band and the observation that electrons are localized in the buffer layer point towards unconventional carrier dynamics in the buffer layer. We presented the outline of a model taking into account the varying potential that electrons in the buffer layer should experience due to their image charge in the substrate. As a consequence of the corrugation of the buffer layer, this attractive image force creates potential wells with depth around 0.93 eV, which could induce localization even at high temperatures.

6.2 Outlook

6.2.1 The buffer layer at high temperature

The model of the image potential views the buffer layer as a corrugated graphene layer on top of SiC without involving any sp^3 hybridization. One would expect such a graphene layer to decouple from the substrate rather easily, which has been observed by numerous experiments on intercalation. We hypothesize that during the growth process, the buffer layer is a free standing graphene layer that turns into a periodically corrugated layer upon cooling down in due to the interaction with the substrate . Experimentally, this hypothesis can be verified by characterizing a buffer layer sample at high temperature (possibly above 1000°) and see if it turns into free-standing graphene at higher thermal energy. Several characterization methods are considered to observe this potential phase transition. Raman spectroscopy is able to differentiate between graphene and the buffer layer, but the signal of a single atomic layer is weak and strong infrared radiation from the bulk SiC drowns the contribution of graphene at high temperature, as observed in our early attempts.

On the other hand, preliminary experiments in collaboration with Pr. Ted Norris at the university of Michigan have demonstrated the compatibility of time-resolved pump/probe spectroscopy to discriminate between graphene and the buffer layer, even at 1000°. The experiment should be performed in a clean chamber in high vacuum to prevent any possible intercalation from contaminants. This type of spectroscopy involves populating empty

energy states with a laser pulse (the pump). A second laser pulse (the probe) measures the transmission for a specific wavelength at a definite time delay after the pump pulse. The experiment is repeated for different delays between pump and probe resulting in a plot of the transmission as a function of time, which characterizes the dynamics of charge carriers in a material. Epitaxial graphene on the Si-face of SiC displays a characteristic peak of enhanced transmission after the pump[215], while the buffer layer does not, as measured in our preliminary experiments.

6.2.2 Theoretical work

In this thesis, we have pointed out the importance of the image potential in a system such as the buffer layer. We believe that it opens the door towards theoretical considerations of the transport in the buffer layer. The calculations should consider the varying self-potential of the electrons wave functions in a corrugated graphene layer on top of a dielectric, which arises as a nonlinear term in the Schrödinger equation.

REFERENCES

[1] E. Curie and V. Sheean, *Madame Curie: A Biography*. Doubleday, Doran, 1937.

[2] K. S. Novoselov, A. K. Geim, S. V. Morozov, D. Jiang, Y. Zhang, S. V. Dubonos, I. V. Grigorieva, and A. A. Firsov, "Electric field effect in atomically thin carbon films," *science*, vol. 306, no. 5696, pp. 666–669, 2004.

[3] C. Berger, Z. Song, T. Li, X. Li, A. Y. Ogbazghi, R. Feng, Z. Dai, A. N. Marchenkov, E. H. Conrad, P. N. First, , and W. A. de Heer, "Ultrathin epitaxial graphite: 2d electron gas properties and a route toward graphene-based nanoelectronics," *The Journal of Physical Chemistry B*, vol. 108, no. 52, pp. 19912–19916, 2004.

[4] E. P. Randviir, D. A. Brownson, and C. E. Banks, "A decade of graphene research: production, applications and outlook," *Materials Today*, vol. 17, no. 9, pp. 426–432, 2014.

[5] I. Frank, D. M. Tanenbaum, A. M. van der Zande, and P. L. McEuen, "Mechanical properties of suspended graphene sheets," *Journal of Vacuum Science & Technology B: Microelectronics and Nanometer Structures Processing, Measurement, and Phenomena*, vol. 25, no. 6, pp. 2558–2561, 2007.

[6] A. K. Geim and K. S. Novoselov, "The rise of graphene," *Nature materials*, vol. 6, no. 3, p. 183, 2007.

[7] F. Schwierz, "Graphene transistors," *Nature nanotechnology*, vol. 5, no. 7, p. 487, 2010.

[8] X. Wang, L. Zhi, and K. Müllen, "Transparent, conductive graphene electrodes for dye-sensitized solar cells," *Nano letters*, vol. 8, no. 1, pp. 323–327, 2008.

[9] F. Schedin, A. Geim, S. Morozov, E. Hill, P. Blake, M. Katsnelson, and K. Novoselov, "Detection of individual gas molecules adsorbed on graphene," *Nature materials*, vol. 6, no. 9, pp. 652–655, 2007.

[10] Y. Liu, X. Dong, and P. Chen, "Biological and chemical sensors based on graphene materials," *Chemical Society Reviews*, vol. 41, no. 6, pp. 2283–2307, 2012.

[11] B. Dlubak, M.-B. Martin, C. Deranlot, B. Servet, S. Xavier, R. Mattana, M. Sprinkle, C. Berger, W. A. De Heer, F. Petroff, *et al.*, "Highly efficient spin transport in epitaxial graphene on sic," *Nature Physics*, vol. 8, no. 7, p. 557, 2012.

[12] M. D. Stoller, S. Park, Y. Zhu, J. An, and R. S. Ruoff, "Graphene-based ultracapacitors," *Nano letters*, vol. 8, no. 10, pp. 3498–3502, 2008.

[13] J. Crossno, J. K. Shi, K. Wang, X. Liu, A. Harzheim, A. Lucas, S. Sachdev, P. Kim, T. Taniguchi, K. Watanabe, *et al.*, "Observation of the dirac fluid and the breakdown of the wiedemann-franz law in graphene," *Science*, vol. 351, no. 6277, pp. 1058–1061, 2016.

[14] G. E. Moore, "Cramming more components onto integrated circuits, reprinted from electronics, volume 38, number 8, april 19, 1965, pp. 114 ff.," *IEEE solid-state circuits society newsletter*, vol. 20, no. 3, pp. 33–35, 2006.

[15] R. Courtland, "Moore's law's next step: 10 nanometers," *IEEE Spectrum*, vol. 54, no. 1, pp. 52–53, 2017.

[16] S. Natarajan, M. Agostinelli, S. Akbar, M. Bost, A. Bowonder, V. Chikarmane, S. Chouksey, A. Dasgupta, K. Fischer, Q. Fu, *et al.*, "A 14nm logic technology featuring 2 nd-generation finfet, air-gapped interconnects, self-aligned double patterning and a 0.0588 μm 2 sram cell size," in *Electron Devices Meeting (IEDM), 2014 IEEE International*, pp. 3–7, IEEE, 2014.

[17] D. R. Dreyer, R. S. Ruoff, and C. W. Bielawski, "From conception to realization: an historial account of graphene and some perspectives for its future," *Angewandte Chemie International Edition*, vol. 49, no. 49, pp. 9336–9344, 2010.

[18] S. Frank, P. Poncharal, Z. L. Wang, and W. A. d. Heer, "Carbon nanotube quantum resistors," *Science*, vol. 280, no. 5370, pp. 1744–1746, 1998.

[19] W. DeHeer, C. Berger, and P. First, "Patterned thin film graphite devices and method for making same," dec 2004. US Patent App. 10/860,710.

[20] A. A. Ahmadieh and H. A. Rafizadeh, "Dispersion curves and elastic constants of graphite," *Phys. Rev. B*, vol. 7, pp. 4527–4537, May 1973.

[21] P. R. Wallace, "The band theory of graphite," *Phys. Rev.*, vol. 71, pp. 622–634, May 1947.

[22] T. Ando, T. Nakanishi, and R. Saito, "Berry's phase and absence of back scattering in carbon nanotubes," *Journal of the Physical Society of Japan*, vol. 67, no. 8, pp. 2857–2862, 1998.

[23] K. S. Novoselov, A. K. Geim, S. Morozov, D. Jiang, M. Katsnelson, I. Grigorieva, S. Dubonos, and A. Firsov, "Two-dimensional gas of massless dirac fermions in graphene," *nature*, vol. 438, no. 7065, pp. 197–200, 2005.

[24] C. Gmez-Navarro, R. T. Weitz, A. M. Bittner, M. Scolari, A. Mews, M. Burghard, and K. Kern, "Electronic transport properties of individual chemically reduced graphene oxide sheets," *Nano Letters*, vol. 7, no. 11, pp. 3499–3503, 2007. PMID: 17944526.

[25] C. Mattevi, H. Kim, and M. Chhowalla, "A review of chemical vapour deposition of graphene on copper," *Journal of Materials Chemistry*, vol. 21, no. 10, pp. 3324–3334, 2011.

[26] A. V. Bommel, J. Crombeen, and A. V. Tooren, "Leed and auger electron observations of the sic(0001) surface," *Surface Science*, vol. 48, no. 2, pp. 463 – 472, 1975.

[27] A. S. Mayorov, R. V. Gorbachev, S. V. Morozov, L. Britnell, R. Jalil, L. A. Ponomarenko, P. Blake, K. S. Novoselov, K. Watanabe, T. Taniguchi, *et al.*, "Micrometer-scale ballistic transport in encapsulated graphene at room temperature," *Nano letters*, vol. 11, no. 6, pp. 2396–2399, 2011.

[28] K. I. Bolotin, K. Sikes, Z. Jiang, M. Klima, G. Fudenberg, J. Hone, P. Kim, and H. Stormer, "Ultrahigh electron mobility in suspended graphene," *Solid State Communications*, vol. 146, no. 9-10, pp. 351–355, 2008.

[29] Y. Zhang, Y.-W. Tan, H. L. Stormer, and P. Kim, "Experimental observation of the quantum hall effect and berry's phase in graphene," *Nature*, vol. 438, pp. 201–204, Nov 2005.

[30] K. I. Bolotin, F. Ghahari, M. D. Shulman, H. L. Stormer, and P. Kim, "Observation of the fractional quantum hall effect in graphene," *Nature*, vol. 462, no. 7270, p. 196, 2009.

[31] Y. Cao, V. Fatemi, S. Fang, K. Watanabe, T. Taniguchi, E. Kaxiras, and P. Jarillo-Herrero, "Unconventional superconductivity in magic-angle graphene superlattices," *Nature*, vol. 556, no. 7699, p. 43, 2018.

[32] S. Pei and H.-M. Cheng, "The reduction of graphene oxide," *Carbon*, vol. 50, no. 9, pp. 3210 – 3228, 2012. Festschrift dedicated to Peter A. Thrower, Editor-in-Chief, 1972 - 2012.

[33] W. S. Hummers Jr and R. E. Offeman, "Preparation of graphitic oxide," *Journal of the american chemical society*, vol. 80, no. 6, pp. 1339–1339, 1958.

[34] X. Li, W. Cai, J. An, S. Kim, J. Nah, D. Yang, R. Piner, A. Velamakanni, I. Jung, E. Tutuc, *et al.*, "Large-area synthesis of high-quality and uniform graphene films on copper foils," *Science*, vol. 324, no. 5932, pp. 1312–1314, 2009.

[35] A. Reina, X. Jia, J. Ho, D. Nezich, H. Son, V. Bulovic, M. S. Dresselhaus, and J. Kong*, "Layer area, few-layer graphene films on arbitrary substrates by chemical vapor deposition," *Nano letters*, vol. 9, no. 8, pp. 3087–3087, 2009.

[36] A. Varykhalov and O. Rader, "Graphene grown on co (0001) films and islands: Electronic structure and its precise magnetization dependence," *Physical Review B*, vol. 80, no. 3, p. 035437, 2009.

[37] J. Coraux, A. T. N Diaye, C. Busse, and T. Michely, "Structural coherency of graphene on ir (111)," *Nano letters*, vol. 8, no. 2, pp. 565–570, 2008.

[38] S.-Y. Kwon, C. V. Ciobanu, V. Petrova, V. B. Shenoy, J. Bareno, V. Gambin, I. Petrov, and S. Kodambaka, "Growth of semiconducting graphene on palladium," *Nano letters*, vol. 9, no. 12, pp. 3985–3990, 2009.

[39] P. Sutter, J. T. Sadowski, and E. Sutter, "Graphene on pt (111): Growth and substrate interaction," *Physical Review B*, vol. 80, no. 24, p. 245411, 2009.

[40] P. W. Sutter, J.-I. Flege, and E. A. Sutter, "Epitaxial graphene on ruthenium," *Nature materials*, vol. 7, no. 5, p. 406, 2008.

[41] W. Strupinski, K. Grodecki, A. Wysmolek, R. Stepniewski, T. Szkopek, P. Gaskell, A. Gruneis, D. Haberer, R. Bozek, J. Krupka, *et al.*, "Graphene epitaxy by chemical vapor deposition on sic," *Nano letters*, vol. 11, no. 4, pp. 1786–1791, 2011.

[42] Y. Zhang, L. Zhang, and C. Zhou, "Review of chemical vapor deposition of graphene and related applications," *Accounts of chemical research*, vol. 46, no. 10, pp. 2329–2339, 2013.

[43] J. Casady and R. W. Johnson, "Status of silicon carbide (sic) as a wide-bandgap semiconductor for high-temperature applications: A review," *Solid-State Electronics*, vol. 39, no. 10, pp. 1409–1422, 1996.

[44] A. Winkelmann, B. Schröter, and W. Richter, "Electron diffraction methods for the analysis of silicon carbide surfaces and the controlled growth of polytype heterostructures," *Journal of Physics: Condensed Matter*, vol. 16, no. 17, p. S1555, 2004.

[45] C. Berger, E. H. Conrad, and W. A. de Heer, "Epigraphene: epitaxial graphene on silicon carbide," *arXiv preprint arXiv:1704.00374*, 2017.

[46] P. N. First, W. A. de Heer, T. Seyller, C. Berger, J. A. Stroscio, and J.-S. Moon, "Epitaxial graphenes on silicon carbide," *MRS bulletin*, vol. 35, no. 4, pp. 296–305, 2010.

[47] N. Mishra, J. Boeckl, N. Motta, and F. Iacopi, "Graphene growth on silicon carbide: A review," *physica status solidi (a)*, vol. 213, no. 9, pp. 2277–2289, 2016.

[48] K. V. Emtsev, A. Bostwick, K. Horn, J. Jobst, G. L. Kellogg, L. Ley, J. L. McChesney, T. Ohta, S. A. Reshanov, J. Rohrl, E. Rotenberg, A. K. Schmid, D. Waldmann, H. B. Weber, and T. Seyller, "Towards wafer-size graphene layers by atmospheric pressure graphitization of silicon carbide," *Nat Mater*, vol. 8, pp. 203–207, Mar 2009.

[49] R. M. Tromp and J. B. Hannon, "Thermodynamics and kinetics of graphene growth on sic(0001)," *Phys. Rev. Lett.*, vol. 102, p. 106104, Mar 2009.

[50] W. A. de Heer, C. Berger, M. Ruan, M. Sprinkle, X. Li, Y. Hu, B. Zhang, J. Hankinson, and E. Conrad, "Large area and structured epitaxial graphene produced by confinement controlled sublimation of silicon carbide," *Proceedings of the National Academy of Sciences*, vol. 108, no. 41, pp. 16900–16905, 2011.

[51] X. Wu, Y. Hu, M. Ruan, N. K. Madiomanana, J. Hankinson, M. Sprinkle, C. Berger, and W. A. de Heer, "Half integer quantum hall effect in high mobility single layer epitaxial graphene," *Applied Physics Letters*, vol. 95, no. 22, 2009.

[52] Y. Hu, M. Ruan, Z. Guo, R. Dong, J. Palmer, J. Hankinson, C. Berger, and W. A. De Heer, "Structured epitaxial graphene: growth and properties," *Journal of Physics D: Applied Physics*, vol. 45, no. 15, p. 154010, 2012.

[53] L. Li and I. S. T. Tsong, "Atomic structures of 6h-sic(0001) and (0001) surfaces," *Surf. Sci.*, vol. 351, pp. 141–148, May 1996.

[54] J. Hass, W. A. de Heer, and E. H. Conrad, "The growth and morphology of epitaxial multilayer graphene," *Journal of Physics: Condensed Matter*, vol. 20, no. 32, p. 323202, 2008.

[55] J. Hass, F. Varchon, J. E. Millán-Otoya, M. Sprinkle, N. Sharma, W. A. de Heer, C. Berger, P. N. First, L. Magaud, and E. H. Conrad, "Why multilayer graphene

on4h-sic(000$\bar{1}$) behaves like a single sheet of graphene," *Phys. Rev. Lett.*, vol. 100, p. 125504, Mar 2008.

[56] M. Sprinkle, M. Ruan, Y. Hu, J. Hankinson, M. Rubio-Roy, B. Zhang, X. Wu, C. Berger, and W. A. De Heer, "Scalable templated growth of graphene nanoribbons on sic," *Nature nanotechnology*, vol. 5, no. 10, p. 727, 2010.

[57] M. Orlita, C. Faugeras, R. Grill, A. Wysmolek, W. Strupinski, C. Berger, W. A. De Heer, G. Martinez, and M. Potemski, "Carrier scattering from dynamical magnetoconductivity in quasineutral epitaxial graphene," *Physical review letters*, vol. 107, no. 21, p. 216603, 2011.

[58] W. A. De Heer, C. Berger, X. Wu, P. N. First, E. H. Conrad, X. Li, T. Li, M. Sprinkle, J. Hass, M. L. Sadowski, *et al.*, "Epitaxial graphene," *Solid State Communications*, vol. 143, no. 1-2, pp. 92–100, 2007.

[59] J. Kedzierski, P.-L. Hsu, P. Healey, P. W. Wyatt, C. L. Keast, M. Sprinkle, C. Berger, and W. A. De Heer, "Epitaxial graphene transistors on sic substrates," *IEEE Transactions on Electron Devices*, vol. 55, no. 8, pp. 2078–2085, 2008.

[60] P. Darancet, N. Wipf, C. Berger, W. A. de Heer, and D. Mayou, "Quenching of the quantum hall effect in multilayered epitaxial graphene: the role of undoped planes," *Physical review letters*, vol. 101, no. 11, p. 116806, 2008.

[61] Z. Guo, R. Dong, P. S. Chakraborty, N. Lourenco, J. Palmer, Y. Hu, M. Ruan, J. Hankinson, J. Kunc, J. D. Cressler, C. Berger, and W. A. de Heer, "Record maximum oscillation frequency in c-face epitaxial graphene transistors," *Nano Letters*, vol. 13, no. 3, pp. 942–947, 2013. PMID: 23418924.

[62] C. Riedl, C. Coletti, and U. Starke, "Structural and electronic properties of epitaxial graphene on sic (0 0 0 1): a review of growth, characterization, transfer doping and hydrogen intercalation," *Journal of Physics D: Applied Physics*, vol. 43, no. 37, p. 374009, 2010.

[63] K. V. Emtsev, F. Speck, T. Seyller, L. Ley, and J. D. Riley, "Interaction, growth, and ordering of epitaxial graphene on sic0001 surfaces: A comparative photoelectron spectroscopy study," *Phys. Rev. B*, vol. 77, p. 155303, Apr 2008.

[64] F. Varchon, R. Feng, J. Hass, X. Li, B. N. Nguyen, C. Naud, P. Mallet, J.-Y. Veuillen, C. Berger, E. H. Conrad, and L. Magaud, "Electronic structure of epitaxial graphene layers on sic: Effect of the substrate," *Phys. Rev. Lett.*, vol. 99, p. 126805, Sep 2007.

[65] M. S. Nevius, M. Conrad, F. Wang, A. Celis, M. N. Nair, A. Taleb-Ibrahimi, A. Tejeda, and E. H. Conrad, "Semiconducting graphene from highly ordered substrate interactions," *Phys. Rev. Lett.*, vol. 115, p. 136802, Sep 2015.

[66] M. Conrad, F. Wang, M. Nevius, K. Jinkins, A. Celis, M. Narayanan Nair, A. Taleb-Ibrahimi, A. Tejeda, Y. Garreau, A. Vlad, *et al.*, "Wide band gap semiconductor from a hidden 2d incommensurate graphene phase," *Nano letters*, vol. 17, no. 1, pp. 341–347, 2016.

[67] M. Conrad, J. Rault, Y. Utsumi, Y. Garreau, A. Vlad, A. Coati, J.-P. Rueff, P. Miceli, and E. Conrad, "Structure and evolution of semiconducting buffer graphene grown on sic (0001)," *Physical Review B*, vol. 96, no. 19, p. 195304, 2017.

[68] M. N. Nair, I. Palacio, A. Celis, A. Zobelli, A. Gloter, S. Kubsky, J.-P. Turmaud, M. Conrad, C. Berger, W. de Heer, *et al.*, "Band gap opening induced by the structural periodicity in epitaxial graphene buffer layer," *Nano letters*, vol. 17, no. 4, pp. 2681–2689, 2017.

[69] A. Bostwick, T. Ohta, T. Seyller, K. Horn, and E. Rotenberg, "Quasiparticle dynamics in graphene," *Nat Phys*, vol. 3, pp. 36–40, Jan 2007.

[70] S. Y. Zhou, G.-H. Gweon, A. V. Fedorov, P. N. First, W. A. de Heer, D.-H. Lee, F. Guinea, A. H. Castro Neto, and A. Lanzara, "Substrate-induced bandgap opening in epitaxial graphene," *Nat Mater*, vol. 6, pp. 770–775, Oct 2007.

[71] J. Ristein, S. Mammadov, and T. Seyller, "Origin of doping in quasi-free-standing graphene on silicon carbide," *Phys. Rev. Lett.*, vol. 108, p. 246104, Jun 2012.

[72] C. Berger, Z. Song, X. Li, X. Wu, N. Brown, C. Naud, D. Mayou, T. Li, J. Hass, A. N. Marchenkov, E. H. Conrad, P. N. First, and W. A. de Heer, "Electronic confinement and coherence in patterned epitaxial graphene," *Science*, vol. 312, no. 5777, pp. 1191–1196, 2006.

[73] T. Shen, J. J. Gu, M. Xu, Y. Q. Wu, M. L. Bolen, M. A. Capano, L. W. Engel, and P. D. Ye, "Observation of quantum-hall effect in gated epitaxial graphene grown on sic (0001)," *Applied Physics Letters*, vol. 95, no. 17, 2009.

[74] A. Tzalenchuk, S. Lara-Avila, A. Kalaboukhov, S. Paolillo, M. Syvajarvi, R. Yakimova, O. Kazakova, J. J. B. M., V. Fal'ko, and S. Kubatkin, "Towards a quantum resistance standard based on epitaxial graphene," *Nat Nano*, vol. 5, pp. 186–189, Mar 2010.

[75] J. Jobst, D. Waldmann, F. Speck, R. Hirner, D. K. Maude, T. Seyller, and H. B. Weber, "Quantum oscillations and quantum hall effect in epitaxial graphene," *Phys. Rev. B*, vol. 81, p. 195434, May 2010.

[76] W. Norimatsu and M. Kusunoki, "Formation process of graphene on sic (0 0 0 1)," *Physica E: Low-dimensional Systems and Nanostructures*, vol. 42, no. 4, pp. 691 – 694, 2010. 18th International Conference on Electron Properties of Two-Dimensional Systems.

[77] J. Baringhaus, M. Ruan, F. Edler, A. Tejeda, M. Sicot, Taleb-IbrahimiAmina, A.-P. Li, Z. Jiang, E. H. Conrad, C. Berger, C. Tegenkamp, and W. A. de Heer, "Exceptional ballistic transport in epitaxial graphene nanoribbons," *Nature*, vol. 506, pp. 349–354, Feb 2014. Letter.

[78] S. Datta, *Electronic transport in mesoscopic systems*. Cambridge university press, 1997.

[79] J. Hicks, A. Tejeda, A. Taleb-Ibrahimi, M. Nevius, F. Wang, K. Shepperd, J. Palmer, F. Bertran, P. Le Fevre, J. Kunc, *et al.*, "A wide-bandgap metal–semiconductor–metal nanostructure made entirely from graphene," *Nature Physics*, vol. 9, no. 1, p. 49, 2013.

[80] M. Nevius, F. Wang, C. Mathieu, N. Barrett, A. Sala, T. Mentes, A. Locatelli, and E. Conrad, "The bottom-up growth of edge specific graphene nanoribbons," *Nano letters*, vol. 14, no. 11, pp. 6080–6086, 2014.

[81] I. Palacio, A. Celis, M. N. Nair, A. Gloter, A. Zobelli, M. Sicot, D. Malterre, M. S. Nevius, W. A. De Heer, C. Berger, *et al.*, "Atomic structure of epitaxial graphene sidewall nanoribbons: flat graphene, miniribbons, and the confinement gap," *Nano letters*, vol. 15, no. 1, pp. 182–189, 2014.

[82] I. Forbeaux, J.-M. Themlin, and J.-M. Debever, "Heteroepitaxial graphite on $6h$ – SiC(0001) : interface formation through conduction-band electronic structure," *Phys. Rev. B*, vol. 58, pp. 16396–16406, Dec 1998.

[83] S. Lilov, "Study of the equilibrium processes in the gas phase during silicon carbide sublimation," *Materials Science and Engineering: B*, vol. 21, no. 1, pp. 65–69, 1993.

[84] L. Malard, M. Pimenta, G. Dresselhaus, and M. Dresselhaus, "Raman spectroscopy in graphene," *Physics Reports*, vol. 473, no. 5, pp. 51 – 87, 2009.

[85] A. Zangwill, *Modern electrodynamics*. Cambridge University Press, 2013.

[86] G. Binnig and H. Rohrer, "Scanning tunneling microscopy," *Surface science*, vol. 126, no. 1-3, pp. 236–244, 1983.

[87] G. Binnig, C. F. Quate, and C. Gerber, "Atomic force microscope," *Physical review letters*, vol. 56, no. 9, p. 930, 1986.

[88] X. N. Xie, H. Chung, C. Sow, and A. Wee, "Nanoscale materials patterning and engineering by atomic force microscopy nanolithography," *Materials Science and Engineering: R: Reports*, vol. 54, no. 1-2, pp. 1–48, 2006.

[89] F. J. Giessibl, "Advances in atomic force microscopy," *Rev. Mod. Phys.*, vol. 75, pp. 949–983, Jul 2003.

[90] XE-70, *User's Manual*. Park Systems, 2009.

[91] M. Emmrich, F. Huber, F. Pielmeier, J. Welker, T. Hofmann, M. Schneiderbauer, D. Meuer, S. Polesya, S. Mankovsky, D. Ködderitzsch, *et al.*, "Subatomic resolution force microscopy reveals internal structure and adsorption sites of small iron clusters," *Science*, vol. 348, no. 6232, pp. 308–311, 2015.

[92] J. J. Sakurai and J. Napolitano, *Modern quantum mechanics*. Cambridge University Press, 2017.

[93] M. A. Vanhove, W. H. Weinberg, and C.-M. Chan, *Low-energy electron diffraction: experiment, theory and surface structure determination*, vol. 6. Springer Science & Business Media, 2012.

[94] C. Davisson and L. H. Germer, "The scattering of electrons by a single crystal of nickel," *Nature*, vol. 119, no. 2998, p. 558, 1927.

[95] L. De Broglie, *Recherches sur la théorie des quanta*. PhD thesis, Migration-université en cours d'affectation, 1924.

[96] J. F. Watts, "X-ray photoelectron spectroscopy," *Surface science techniques*, pp. 5–23, 1994.

[97] S. A. Campbell, *Fabrication engineering at the micro and nanoscale*. New York: Oxford University Press,, 2008.

[98] MicroChem, *Nano PMMA and copolymer*. Available at `http://microchem.com/pdf/PMMA_Data_Sheet.pdf`.

[99] Shipley, *Microposit MF-319 developer*. Available at `http://microchem.com/products/images/uploads/MF_319_Data_Sheet.pdf`.

[100] S. M. George, "Atomic layer deposition: an overview," *Chemical reviews*, vol. 110, no. 1, pp. 111–131, 2009.

[101] K. F. Jensen, *Chemical Vapor Deposition*, ch. 5, pp. 199–263. ACS Publications, 1989.

[102] P. C. Andricacos, C. Uzoh, J. O. Dukovic, J. Horkans, and H. Deligianni, "Damascene copper electroplating for chip interconnections," *IBM Journal of Research and Development*, vol. 42, no. 5, pp. 567–574, 1998.

[103] X. Wang, S. M. Tabakman, and H. Dai, "Atomic layer deposition of metal oxides on pristine and functionalized graphene," *Journal of the American Chemical Society*, vol. 130, no. 26, pp. 8152–8153, 2008.

[104] R. H. J. Vervuurt, W. M. M. E. Kessels, and A. A. Bol, "Atomic layer deposition for graphene device integration," *Advanced Materials Interfaces*, vol. 4, no. 18, p. 1700232, 2017.

[105] P. Kelly and R. Arnell, "Magnetron sputtering: a review of recent developments and applications," *Vacuum*, vol. 56, no. 3, pp. 159–172, 2000.

[106] W. Van Dorp and C. W. Hagen, "A critical literature review of focused electron beam induced deposition," *Journal of Applied Physics*, vol. 104, no. 8, p. 10, 2008.

[107] R. Bunshah and R. Schramm, "Alumina deposition by activated reactive evaporation," *Thin Solid Films*, vol. 40, pp. 211–216, 1977.

[108] L. Van der Pauw, "A method of measuring specific resistivity and hall effect of discs of arbitrary shape," *Philips research reports*, vol. 13, pp. 1–9, 1958.

[109] I. Miccoli, F. Edler, H. Pfnür, and C. Tegenkamp, "The 100th anniversary of the four-point probe technique: the role of probe geometries in isotropic and anisotropic systems," *Journal of Physics: Condensed Matter*, vol. 27, no. 22, p. 223201, 2015.

[110] D. C. Elias, R. R. Nair, T. Mohiuddin, S. Morozov, P. Blake, M. Halsall, A. Ferrari, D. Boukhvalov, M. Katsnelson, A. Geim, *et al.*, "Control of graphene's properties by reversible hydrogenation: evidence for graphane," *Science*, vol. 323, no. 5914, pp. 610–613, 2009.

[111] F. Wang, G. Liu, S. Rothwell, M. Nevius, A. Tejeda, A. Taleb-Ibrahimi, L. Feldman, P. Cohen, and E. Conrad, "Wide-gap semiconducting graphene from nitrogen-seeded sic," *Nano letters*, vol. 13, no. 10, pp. 4827–4832, 2013.

[112] I. Pletikosić, M. Kralj, P. Pervan, R. Brako, J. Coraux, A. Ndiaye, C. Busse, and T. Michely, "Dirac cones and minigaps for graphene on ir (111)," *Physical Review Letters*, vol. 102, no. 5, p. 056808, 2009.

[113] C. Enderlein, Y. Kim, A. Bostwick, E. Rotenberg, and K. Horn, "The formation of an energy gap in graphene on ruthenium by controlling the interface," *New Journal of Physics*, vol. 12, no. 3, p. 033014, 2010.

[114] C. S. Chang, I. S. T. Tsong, Y. C. Wang, and R. F. Davis, "Scanning tunneling microscopy and spectroscopy of cubic [beta]-sic(111) surfaces," *Surf. Sci.*, vol. 256, pp. 354–360, Oct. 1991.

[115] M. H. Tsai, C. S. Chang, J. D. Dow, and I. S. T. Tsong, "Electronic contributions to scanning-tunneling-microscopy images of an annealed beta-sic(111) surface," *Phys. Rev. B*, vol. 45, pp. 1327–1332, Jan. 1992.

[116] G. M. Rutter, N. P. Guisinger, J. N. Crain, E. A. A. Jarvis, M. D. Stiles, T. Li, P. N. First, and J. A. Stroscio, "Imaging the interface of epitaxial graphene with silicon carbide via scanning tunneling microscopy," *Phys. Rev. B*, vol. 76, p. 235416, Dec 2007.

[117] S. Goler, C. Coletti, V. Piazza, P. Pingue, F. Colangelo, V. Pellegrini, K. V. Emtsev, S. Forti, U. Starke, F. Beltram, and S. Heun, "Revealing the atomic structure of the buffer layer between sic(0001) and epitaxial graphene," *Carbon*, vol. 51, no. Complete, pp. 249–254, 2013.

[118] W. Chen, H. Xu, L. Liu, X. Gao, D. Qi, G. Peng, S. C. Tan, Y. Feng, K. P. Loh, and A. T. S. Wee, "Atomic structure of the 6hsic(0 0 0 1) nanomesh," *Surface Science*, vol. 596, no. 13, pp. 176 – 186, 2005.

[119] A. Mattausch and O. Pankratov, "*Ab Initio* study of graphene on sic," *Phys. Rev. Lett.*, vol. 99, p. 076802, Aug 2007.

[120] J. Baringhaus, *Mesoscopic transport phenomena in epitaxial graphene nanostructures: A surface science approach*. PhD thesis, Gottfried Wilhelm Leibniz Universitat Hannover, 2015.

[121] J. Baringhaus, J. Aprojanz, J. Wiegand, D. Laube, M. Halbauer, J. Hubner, M. Oestreich, and C. Tegenkamp, "Growth and characterization of sidewall graphene nanoribbons," *Applied Physics Letters*, vol. 106, no. 4, 2015.

[122] C. Riedl, C. Coletti, T. Iwasaki, A. Zakharov, and U. Starke, "Quasi-free-standing epitaxial graphene on sic obtained by hydrogen intercalation," *Physical review letters*, vol. 103, no. 24, p. 246804, 2009.

[123] J. D. Emery, V. D. Wheeler, J. E. Johns, M. E. McBriarty, B. Detlefs, M. C. Hersam, D. Kurt Gaskill, and M. J. Bedzyk, "Structural consequences of hydrogen intercalation of epitaxial graphene on sic (0001)," *Applied Physics Letters*, vol. 105, no. 16, p. 161602, 2014.

[124] F. Speck, J. Jobst, F. Fromm, M. Ostler, D. Waldmann, M. Hundhausen, H. B. Weber, and T. Seyller, "The quasi-free-standing nature of graphene on h-saturated sic (0001)," *Applied Physics Letters*, vol. 99, no. 12, p. 122106, 2011.

[125] C. Melios, S. Spencer, A. Shard, W. Strupiński, S. R. P. Silva, and O. Kazakova, "Surface and interface structure of quasi-free standing graphene on sic," *2D Materials*, vol. 3, no. 2, p. 025023, 2016.

[126] C. Xia, L. I. Johansson, A. Zakharov, L. Hultman, and C. Virojanadara, "Effects of al on epitaxial graphene grown on 6h-sic (0001)," *Materials Research Express*, vol. 1, no. 1, p. 015606, 2014.

[127] B. Premlal, M. Cranney, F. Vonau, D. Aubel, D. Casterman, M. De Souza, and L. Simon, "Surface intercalation of gold underneath a graphene monolayer on sic (0001) studied by scanning tunneling microscopy and spectroscopy," *Applied Physics Letters*, vol. 94, no. 26, p. 263115, 2009.

[128] A. Stöhr, S. Forti, S. Link, A. A. Zakharov, K. Kern, U. Starke, and H. M. Benia, "Intercalation of graphene on sic (0001) via ion implantation," *Physical Review B*, vol. 94, no. 8, p. 085431, 2016.

[129] J. L. McChesney, A. Bostwick, T. Ohta, T. Seyller, K. Horn, J. González, and E. Rotenberg, "Extended van hove singularity and superconducting instability in doped graphene," *Physical review letters*, vol. 104, no. 13, p. 136803, 2010.

[130] K. Yagyu, T. Tajiri, A. Kohno, K. Takahashi, H. Tochihara, H. Tomokage, and T. Suzuki, "Fabrication of a single layer graphene by copper intercalation on a sic (0001) surface," *Applied Physics Letters*, vol. 104, no. 5, p. 053115, 2014.

[131] A. L. Walter, K.-J. Jeon, A. Bostwick, F. Speck, M. Ostler, T. Seyller, L. Moreschini, Y. S. Kim, Y. J. Chang, K. Horn, *et al.*, "Highly p-doped epitaxial graphene obtained by fluorine intercalation," *Applied Physics Letters*, vol. 98, no. 18, p. 184102, 2011.

[132] S. Sung, J. Yang, P. Lee, J. Kim, M. Ryu, H. Park, G. Lee, C. Hwang, K. S. Kim, J. Kim, *et al.*, "Spin-induced band modifications of graphene through intercalation of magnetic iron atoms," *Nanoscale*, vol. 6, no. 7, pp. 3824–3829, 2014.

[133] K. V. Emtsev, A. A. Zakharov, C. Coletti, S. Forti, and U. Starke, "Ambipolar doping in quasifree epitaxial graphene on sic (0001) controlled by ge intercalation," *Physical Review B*, vol. 84, no. 12, p. 125423, 2011.

[134] M. Ostler, F. Fromm, R. J. Koch, P. Wehrfritz, F. Speck, H. Vita, S. Böttcher, K. Horn, and T. Seyller, "Buffer layer free graphene on sic (0 0 0 1) via interface oxidation in water vapor," *Carbon*, vol. 70, pp. 258–265, 2014.

[135] C. Virojanadara, S. Watcharinyanon, A. Zakharov, and L. I. Johansson, "Epitaxial graphene on 6 h-sic and li intercalation," *Physical Review B*, vol. 82, no. 20, p. 205402, 2010.

[136] T. Gao, Y. Gao, C. Chang, Y. Chen, M. Liu, S. Xie, K. He, X. Ma, Y. Zhang, and Z. Liu, "Atomic-scale morphology and electronic structure of manganese atomic layers underneath epitaxial graphene on sic (0001)," *ACS nano*, vol. 6, no. 8, pp. 6562–6568, 2012.

[137] S. Watcharinyanon, L. I. Johansson, C. Xia, and C. Virojanadara, "Changes in structural and electronic properties of graphene grown on 6h-sic (0001) induced by na deposition," *Journal of Applied Physics*, vol. 111, no. 8, p. 083711, 2012.

[138] S. Oida, F. McFeely, J. Hannon, R. Tromp, M. Copel, Z. Chen, Y. Sun, D. Farmer, and J. Yurkas, "Decoupling graphene from sic (0001) via oxidation," *Physical Review B*, vol. 82, no. 4, p. 041411, 2010.

[139] A. Yurtsever, J. Onoda, T. Iimori, K. Niki, T. Miyamachi, M. Abe, S. Mizuno, S. Tanaka, F. Komori, and Y. Sugimoto, "Effects of pb intercalation on the structural and electronic properties of epitaxial graphene on sic," *Small*, vol. 12, no. 29, pp. 3956–3966, 2016.

[140] C. Xia, L. I. Johansson, Y. Niu, A. A. Zakharov, E. Janzén, and C. Virojanadara, "High thermal stability quasi-free-standing bilayer graphene formed on 4h–sic (0 0 0 1) via platinum intercalation," *Carbon*, vol. 79, pp. 631–635, 2014.

[141] H. Kim, O. Dugerjav, A. Arvisbaatar, and J. M. Seo, "Bifunctional effects of the ordered si atoms intercalated between quasi-free-standing epitaxial graphene and sic (0001): graphene doping and substrate band bending," *New Journal of Physics*, vol. 17, no. 8, p. 083058, 2015.

[142] H. Kim, O. Dugerjav, A. Lkhagvasuren, and J. M. Seo, "Charge neutrality of quasi-free-standing monolayer graphene induced by the intercalated sn layer," *Journal of Physics D: Applied Physics*, vol. 49, no. 13, p. 135307, 2016.

[143] S. Watcharinyanon, L. I. Johansson, C. Xia, J. I. Flege, A. Meyer, J. Falta, and C. Virojanadara, "Ytterbium intercalation of epitaxial graphene grown on si-face sic," *Graphene*, vol. 2, no. 02, p. 66, 2013.

[144] C. Riedl, U. Starke, J. Bernhardt, M. Franke, and K. Heinz, "Structural properties of the graphene-sic(0001) interface as a key for the preparation of homogeneous large-terrace graphene surfaces," *Phys. Rev. B*, vol. 76, p. 245406, Dec 2007.

[145] S. Kim, J. Ihm, H. J. Choi, and Y.-W. Son, "Origin of anomalous electronic structures of epitaxial graphene on silicon carbide," *Phys. Rev. Lett.*, vol. 100, p. 176802, Apr 2008.

[146] R. C. Haddon, ". pi.-electrons in three dimensiona," *Accounts of chemical research*, vol. 21, no. 6, pp. 243–249, 1988.

[147] F. Fromm, M. Oliveira Jr, A. Molina-Sanchez, M. Hundhausen, J. Lopes, H. Riechert, L. Wirtz, and T. Seyller, "Contribution of the buffer layer to the raman spectrum of epitaxial graphene on sic (0001)," *New Journal of Physics*, vol. 15, no. 4, p. 043031, 2013.

[148] A. Tiberj, J. R. Huntzinger, N. Camara, P. Godignon, and J. Camassel, "Raman spectrum and optical extinction of graphene buffer layers on the Si-face of 6H-SiC," *ArXiv e-prints*, Dec. 2012.

[149] W. Strupinski, K. Grodecki, P. Caban, P. Ciepielewski, I. Jozwik-Biala, and J. Baranowski, "Formation mechanism of graphene buffer layer on sic(0 0 0 1)," *Carbon*, vol. 81, pp. 63 – 72, 2015.

[150] A. Nagashima, N. Tejima, and C. Oshima, "Electronic states of the pristine and alkali-metal-intercalated monolayer graphite/ni(111) systems," *Phys. Rev. B*, vol. 50, pp. 17487–17495, Dec 1994.

[151] S. Watcharinyanon, C. Virojanadara, and L. I. Johansson, "Rb and cs deposition on epitaxial graphene grown on 6h-sic (0001)," *Surface Science*, vol. 605, no. 21-22, pp. 1918–1922, 2011.

[152] M. Narayanan Nair, I. Palacio, A. Celis, A. Zobelli, A. Gloter, S. Kubsky, J.-P. Turmaud, M. Conrad, C. Berger, W. de Heer, *et al.*, "Band gap opening induced by the structural periodicity in epitaxial graphene buffer layer," *Nano Letters*, 2017.

[153] J. M. Palmer, *Pre-growth structures for high quality epitaxial graphene nanoelectronics grown on silicon carbide*. PhD thesis, Georgia Institute of Technology, 2014.

[154] V. Borovikov and A. Zangwill, "Step bunching of vicinal 6 h-sic {0001} surfaces," *Physical Review B*, vol. 79, no. 24, p. 245413, 2009.

[155] J. Palmer, J. Kunc, Y. Hu, J. Hankinson, Z. Guo, C. Berger, and W. A. de Heer, "Controlled epitaxial graphene growth within removable amorphous carbon corrals," *Applied Physics Letters*, vol. 105, no. 2, 2014.

[156] X. Yu, C. Hwang, C. Jozwiak, A. Khl, A. Schmid, and A. Lanzara, "New synthesis method for the growth of epitaxial graphene," *Journal of Electron Spectroscopy and Related Phenomena*, vol. 184, no. 36, pp. 100 – 106, 2011. Advances in Vacuum Ultraviolet and X-ray PhysicsThe 37th International Conference on Vacuum Ultraviolet and X-ray Physics (VUVX2010).

[157] P. G. Collins, K. Bradley, M. Ishigami, and d. A. Zettl, "Extreme oxygen sensitivity of electronic properties of carbon nanotubes," *science*, vol. 287, no. 5459, pp. 1801–1804, 2000.

[158] V. Derycke, R. Martel, J. Appenzeller, and P. Avouris, "Controlling doping and carrier injection in carbon nanotube transistors," *Applied Physics Letters*, vol. 80, no. 15, pp. 2773–2775, 2002.

[159] J. Kong, N. R. Franklin, C. Zhou, M. G. Chapline, S. Peng, K. Cho, and H. Dai, "Nanotube molecular wires as chemical sensors," *science*, vol. 287, no. 5453, pp. 622–625, 2000.

[160] A. Stassen, R. De Boer, N. Iosad, and A. Morpurgo, "Influence of the gate dielectric on the mobility of rubrene single-crystal field-effect transistors," *Applied Physics Letters*, vol. 85, no. 17, pp. 3899–3901, 2004.

[161] C. Kittel, P. McEuen, and P. McEuen, *Introduction to solid state physics*, vol. 8. Wiley New York, 1996.

[162] X. Zhang, Q. Xue, and D. Zhu, "Positive and negative linear magnetoresistance of graphite," *Physics Letters A*, vol. 320, no. 5-6, pp. 471–477, 2004.

[163] S. Sze, *Physics of semiconductor devices (2nd edition)*. Wiley-Interscience,New York, NY, Jan 1981.

[164] R. Jalilian, L. A. Jauregui, G. Lopez, J. Tian, C. Roecker, M. M. Yazdanpanah, R. W. Cohn, I. Jovanovic, and Y. P. Chen, "Scanning gate microscopy on graphene: charge inhomogeneity and extrinsic doping," *Nanotechnology*, vol. 22, no. 29, p. 295705, 2011.

[165] B. I. Shklovskii and A. L. Efros, *Electronic properties of doped semiconductors*, vol. 45. Springer Science & Business Media, 2013.

[166] A. Zabrodsky and I. Shlimak, "Effect of doping inhomogeneities on the conductivity of heavily doped and compensated semiconductors," *Fizika Tekhn. Poluprov.*, vol. 9, no. 3, pp. 587–589, 1975.

[167] N. Mott, "Conduction in glasses containing transition metal ions," *Journal of Non-Crystalline Solids*, vol. 1, no. 1, pp. 1–17, 1968.

[168] N. Mott, "Conduction in non-crystalline materials: Iii. localized states in a pseudogap and near extremities of conduction and valence bands," *Philosophical Magazine*, vol. 19, no. 160, pp. 835–852, 1969.

[169] J. Hauser, "Hopping conductivity in amorphous carbon films," *Solid State Communications*, vol. 17, no. 12, pp. 1577–1580, 1975.

[170] J. Hauser, "Electrical, structural and optical properties of amorphous carbon," *Journal of Non-Crystalline Solids*, vol. 23, no. 1, pp. 21–41, 1977.

[171] R. Rosenbaum, "Crossover from mott to efros-shklovskii variable-range-hopping conductivity in in x o y films," *Physical Review B*, vol. 44, no. 8, p. 3599, 1991.

[172] D. Yu, C. Wang, B. L. Wehrenberg, and P. Guyot-Sionnest, "Variable range hopping conduction in semiconductor nanocrystal solids," *Physical review letters*, vol. 92, no. 21, p. 216802, 2004.

[173] L. Pi, L. Zheng, and Y. Zhang, "Transport mechanism in polycrystalline la 0.825 sr 0.175 mn 1- x cu x o 3," *Physical Review B*, vol. 61, no. 13, p. 8917, 2000.

[174] M. Jin, H.-K. Jeong, W. J. Yu, D. J. Bae, B. R. Kang, and Y. H. Lee, "Graphene oxide thin film field effect transistors without reduction," *Journal of Physics D: Applied Physics*, vol. 42, no. 13, p. 135109, 2009.

[175] H. Liu, A. Pourret, and P. Guyot-Sionnest, "Mott and efros-shklovskii variable range hopping in cdse quantum dots films," *ACS nano*, vol. 4, no. 9, pp. 5211–5216, 2010.

[176] A. J. Houtepen, D. Kockmann, and D. Vanmaekelbergh, "Reappraisal of variable-range hopping in quantum-dot solids," *Nano letters*, vol. 8, no. 10, pp. 3516–3520, 2008.

[177] J. Delahaye, J. Brison, and C. Berger, "Evidence for variable range hopping conductivity in the ordered quasicrystal i-alpdre," *Physical review letters*, vol. 81, no. 19, p. 4204, 1998.

[178] A. Efros and B. Shklovskii, "Coulomb gap and low temperature conductivity of disordered systems," *Journal of Physics C: Solid State Physics*, vol. 8, no. 4, p. L49, 1975.

[179] F. Van Keuls, X. Hu, H. Jiang, and A. Dahm, "Screening of the coulomb interaction in two-dimensional variable-range hopping," *Physical Review B*, vol. 56, no. 3, p. 1161, 1997.

[180] D. K. Schroder, *Semiconductor material and device characterization*. John Wiley & Sons, 2006.

[181] B. Shklovskii, "Hopping conduction in semiconductors subjected to a strong electric field.," *Sov Phys Semicond*, 1973.

[182] O. Mitrofanov and M. Manfra, "Poole-frenkel electron emission from the traps in algan/gan transistors," *Journal of Applied Physics*, vol. 95, no. 11, pp. 6414–6419, 2004.

[183] S. Marianer and B. Shklovskii, "Effective temperature of hopping electrons in a strong electric field," *Physical Review B*, vol. 46, no. 20, p. 13100, 1992.

[184] C. Nebel, "Transport in a-si: H," *Journal of non-crystalline solids*, vol. 137, pp. 395–400, 1991.

[185] B. Cleve, B. Movaghar, R. Schumacher, and P. Thomas, "High-field and low-field transport in amorphous semiconductors," *Journal of non-crystalline solids*, vol. 137, pp. 415–418, 1991.

[186] J. Casas-Vázquez and D. Jou, "Temperature in non-equilibrium states: a review of open problems and current proposals," *Reports on Progress in Physics*, vol. 66, no. 11, p. 1937, 2003.

[187] S. D. Baranovskii, "Mott lecture: Description of charge transport in disordered organic semiconductors: Analytical theories and computer simulations," *physica status solidi (a)*, 2018.

[188] D. J. Thouless, "Anderson's theory of localized states," *Journal of Physics C: Solid State Physics*, vol. 3, no. 7, p. 1559, 1970.

[189] D. Dasgupta, F. Demichelis, and A. Tagliaferro, "Electrical conductivity of amorphous carbon and amorphous hydrogenated carbon," *Philosophical Magazine B*, vol. 63, no. 6, pp. 1255–1266, 1991.

[190] C. Godet, "Hopping model for charge transport in amorphous carbon," *Philosophical Magazine B*, vol. 81, no. 2, pp. 205–222, 2001.

[191] J. Robertson, "Amorphous carbon," *Advances in Physics*, vol. 35, no. 4, pp. 317–374, 1986.

[192] C. Godet, S. Kumar, and V. Chu, "Field-enhanced electrical transport mechanisms in amorphous carbon films," *Philosophical Magazine*, vol. 83, no. 29, pp. 3351–3365, 2003.

[193] S. Kumar, C. Godet, A. Goudovskikh, J.-P. Kleider, G. Adamopoulos, and V. Chu, "High-field transport in amorphous carbon and carbon nitride films," *Journal of non-crystalline solids*, vol. 338, pp. 349–352, 2004.

[194] N. Apsley and H. Hughes, "Temperature-and field-dependence of hopping conduction in disordered systems," *Philosophical Magazine*, vol. 30, no. 5, pp. 963–972, 1974.

[195] J. Robertson, "Electronic processes in hydrogenated amorphous carbon," *Journal of non-crystalline solids*, vol. 198, pp. 615–618, 1996.

[196] C. Cheah, C. Gómez-Navarro, L. Jaurigue, and A. Kaiser, "Conductance of partially disordered graphene: crossover from temperature-dependent to field-dependent variable-range hopping," *Journal of Physics: Condensed Matter*, vol. 25, no. 46, p. 465303, 2013.

[197] S. Ghatak, A. N. Pal, and A. Ghosh, "Nature of electronic states in atomically thin mos2 field-effect transistors," *Acs Nano*, vol. 5, no. 10, pp. 7707–7712, 2011.

[198] H. Qiu, T. Xu, Z. Wang, W. Ren, H. Nan, Z. Ni, Q. Chen, S. Yuan, F. Miao, F. Song, *et al.*, "Hopping transport through defect-induced localized states in molybdenum disulphide," *Nature communications*, vol. 4, p. 2642, 2013.

[199] N. Papadopoulos, G. A. Steele, and H. S. van der Zant, "Efros-shklovskii variable range hopping and nonlinear transport in 1 t/1 t- mos 2," *Physical Review B*, vol. 96, no. 23, p. 235436, 2017.

[200] S. J. Choi, B.-K. Kim, T.-H. Lee, Y. H. Kim, Z. Li, E. Pop, J.-J. Kim, J. H. Song, and M.-H. Bae, "Electrical and thermoelectric transport by variable range hopping in thin black phosphorus devices," *Nano letters*, vol. 16, no. 7, pp. 3969–3975, 2016.

[201] S. Sinha, S. Kumar Chatterjee, J. Ghosh, and A. Kumar Meikap, "Structural characterization and observation of variable range hopping conduction mechanism at high temperature in cdse quantum dot solids," *Journal of applied physics*, vol. 113, no. 9, p. 093703, 2013.

[202] K. Whitham, J. Yang, B. H. Savitzky, L. F. Kourkoutis, F. Wise, and T. Hanrath, "Charge transport and localization in atomically coherent quantum dot solids," *Nature materials*, vol. 15, no. 5, p. 557, 2016.

[203] J. M. B. Lopes dos Santos, N. M. R. Peres, and A. H. Castro Neto, "Graphene bilayer with a twist: Electronic structure," *Phys. Rev. Lett.*, vol. 99, p. 256802, Dec 2007.

[204] G. T. De Laissardiere, D. Mayou, and L. Magaud, "Numerical studies of confined states in rotated bilayers of graphene," *Physical Review B*, vol. 86, no. 12, p. 125413, 2012.

[205] R. Bistritzer and A. H. MacDonald, "Moiré bands in twisted double-layer graphene," *Proceedings of the National Academy of Sciences*, vol. 108, no. 30, pp. 12233–12237, 2011.

[206] D. Wong, Y. Wang, J. Jung, S. Pezzini, A. M. DaSilva, H.-Z. Tsai, H. S. Jung, R. Khajeh, Y. Kim, J. Lee, S. Kahn, S. Tollabimazraehno, H. Rasool, K. Watanabe, T. Taniguchi, A. Zettl, S. Adam, A. H. MacDonald, and M. F. Crommie, "Local spectroscopy of moiré-induced electronic structure in gate-tunable twisted bilayer graphene," *Phys. Rev. B*, vol. 92, p. 155409, Oct 2015.

[207] Y. Cao, V. Fatemi, A. Demir, S. Fang, S. L. Tomarken, J. Y. Luo, J. D. Sanchez-Yamagishi, K. Watanabe, T. Taniguchi, E. Kaxiras, *et al.*, "Correlated insulator behaviour at half-filling in magic-angle graphene superlattices," *Nature*, vol. 556, no. 7699, p. 80, 2018.

[208] N. F. MOTT, "Metal-insulator transition," *Rev. Mod. Phys.*, vol. 40, pp. 677–683, Oct 1968.

[209] S.-P. Kou and Z.-Y. Weng, "Self-localization of holes in a lightly doped mott insulator," *The European Physical Journal B - Condensed Matter and Complex Systems*, vol. 47, pp. 37–46, Sep 2005.

[210] N. Kirova and M.-N. Bussac, "Self-trapping of electrons at the field-effect junction of a molecular crystal," *Phys. Rev. B*, vol. 68, p. 235312, Dec 2003.

[211] N.-H. Ge, C. M. Wong, R. L. Lingle, J. D. McNeill, K. J. Gaffney, and C. B. Harris, "Femtosecond dynamics of electron localization at interfaces," *Science*, vol. 279, no. 5348, pp. 202–205, 1998.

[212] V. Vyurkov and D. Svintsov, "Quantum single electron solitons near metal surface," *arXiv preprint arXiv:1308.3460*, 2013.

[213] D. Stradi, S. Barja, C. Díaz, M. Garnica, B. Borca, J. Hinarejos, D. Sánchez-Portal, M. Alcamí, A. Arnau, A. V. De Parga, *et al.*, "Electron localization in epitaxial graphene on ru (0001) determined by moiré corrugation," *Physical Review B*, vol. 85, no. 12, p. 121404, 2012.

[214] N. Armbrust, J. Güdde, P. Jakob, and U. Höfer, "Time-resolved two-photon photoemission of unoccupied electronic states of periodically rippled graphene on ru (0001)," *Physical review letters*, vol. 108, no. 5, p. 056801, 2012.

[215] H. Wang, J. H. Strait, P. A. George, S. Shivaraman, V. B. Shields, M. Chandrashekhar, J. Hwang, F. Rana, M. G. Spencer, C. S. Ruiz-Vargas, *et al.*, "Ultrafast relaxation dynamics of hot optical phonons in graphene," *Applied Physics Letters*, vol. 96, no. 8, p. 081917, 2010.

VITA

Jean-Philippe was born in France's countryside near Lyon. Naturally curious, he grew up being fascinated by nature's diverse phenomena such as the weather, volcanoes and earthquakes, the colors of the sunset and planetary movements. When he discovered in high school that physics gave explanations for all of those curiosity, he decided that he wanted to learn more about it. He attended the Grenoble Institute of Technology where he earned a Bachelor of Science in engineering physics in 2011. He then joined a double-degree program between Grenoble Institute of Technology and Kungliga Tekniska Hgskolan in Stockholm, Sweden which gave him the grade of Master of Science in engineering physics in 2013. He came as a research intern at Georgia Tech in the summer of 2012 to work in the epitaxial graphene lab with Walt de Heer's group. He came back in August 2013 as a PhD student in the School of Physics Georgia Tech to work under the supervision of Pr. de Heer. Upon completion of his doctoral work, Jean-Philippe will go on to work on the development of new technologies for the microelectronic industry.